SIEMENS

Siemens Power Generation, Inc.

Small-Scale Low Cost Solid Oxide Fuel Cell Power Systems

Final Report
of
DOE CO-Operative Agreement No. DE-FC26-02NT41247

Reporting Period:
August 2002 thru August 2006

Presented to

National Energy Technology Laboratory
U.S. Department of Energy

by

Siemens Power Generation, Inc.
George Westinghouse Science and Technology Center
1310 Beulah Road
Pittsburgh, PA 15235-5098

Project Manager: S. D. Vora

February 2008

DISCLAIMER

ABSTRACT

Progress in tasks seeking greater cell power density and lower cost through new cell designs, new cell materials and lower operating temperature is summarized. The design of the program required Proof-of-Concept unit of residential capacity scale is reviewed along with a summary of results from its successful test.

Attachment 1 summarizes the status of cell development. Attachment 2 summarizes the status of generator design, and Attachment 3 of BOP design.

TABLE OF CONTENTS

PAGE

LIST OF FIGURES

LIST OF TABLES

EXECUTIVE SUMMARY

This report summarizes SECA Phase-1 program results - August 2002 through August 2006. The program consists of tasks dealing with solid oxide fuel cell [SOFC] development, small scale {i.e. residential scale} SOFC generator design and development, small scale balance of plant [BOP] design and development, and the design, fabrication, and test of a proof-of-concept [POC] power system of nominally 5 kWe capacity.

Cell development has encompassed alternative geometric concepts for high power density [HPD] cathode supported cells, alternative materials for cell constituent elements, the analytic investigation of cell structural viability and electrochemical performance, the development of fabrication technology for alternative cell concepts, the fabrication of specimen cells, the experimental validation of thermal/ structural integrity, the experimental corroboration of electrochemical performance, and the optimization of cell characteristics for inclusion in a viable generator module design. The commercial computational fluid dynamic [CFD] code FLUENT along with a user defined function to model SOFC electrochemical performance was used to generate detailed temperature fields within the cell. The industry standard structural analysis code ANSYS was used to investigate cell structural integrity. The HPD5 cell was selected for application to the POC because fabrication technology was established and therefore compatible with program schedule. The Delta-n cell geometry was selected as the most promising. Delta-n cells were fabricated using cathode extrusion and sintering followed by plasma spray application of electrolyte, interconnection, and anode. A developmental sample Delta-n cell with an active anode area of approximately 1400 cmsq yielded 330 Watts at 0.7 Volts under test. Peak power was extrapolated to over 500 Watts per cell. The plasma spray apparatus procured and installed can process Delta-n cells 130 cm long by 16 cm wide. Delta-n cells of these dimensions should be capable of over 1 kWe per cell.

Generator module design and development is intertwined with cell optimization because the proper distribution and flow of reactants and reactant products is the essence of module design considering electrochemical needs, thermal management needs, structural needs, cell electrical interconnection and electrical power extraction form the generator module. The POC generator module employs 36 HPD5R1 cells arranged in two rows which straddle an ejector and natural gas reformer assembly. Air is carried into the cathode passages via air feed tubes and the ejector serves to recirculate spent anode gas and mix it with the natural gas fuel in the fashion of the well known Siemens seal-less generator module design. The POC has operated for the required 1500 hours producing 3.3 kWe gross DC power at 35% efficiency [dc/LHV ng]. Generator design concepts for utilization of the Delta-n cell are under development and evaluation.

Siemens has successfully met SECA Phase-1 program objectives.

ATTACHMENT 1

1. CELL DEVELOPMENT

1.1 DEVELOPMENT OF OPTIMIZED DESIGN FOR THE SEAL-LESS PLANAR AIR ELECTRODE (CATHODE) SUPPORT TUBES

The "High Power Density" cathode supported solid oxide fuel cell designated HPD5R1 (see Figure 1-3) was selected as the baseline cell for materials improvement, manufacturing process development and generator module design and consequently was the standard against which alternative HPD cell configurations were evaluated.

1.1.1 ANALYTICAL MODELING AND SIMULATION

1.1.1.1 INTRODUCTION

The HPD cell was modeled analytically to estimate thermal-hydraulic and electrochemical performance. Certain model parameters were determined in the process of validating the model against isothermal cell test data. The electrochemical model was then applied to determine in-stack [i.e. non-isothermal] cell performance. A variety of HPD cathode cross-sections were investigated analytically with particular emphasis on thermal stress tolerance. Thermal stress experiments were performed to supplement and corroborate the analytical investigations. Alternative module designs were investigated in parallel with efforts to optimize the cell design to ensure compatibility, viability, reliability, and cost effective high efficiency.

1.1.1.2 EXPERIMENTAL

1.1.1.2.1 COMPUTATIONAL TOOL

The commercial computational fluid dynamics [CFD] code, FLUENT, along with the SOFC user defined function (UDF) to model cell electrochemistry, was chosen as the computational tool of choice for the thermal-hydraulic and electrochemical analysis of cell behavior. The Fluent based SOFC model has the ability to generate detailed temperature fields, which can be transferred to structural analysis software such as ANSYS or ALGOR.

1.1.1.2.2 OPTIMIZED HPD CELL DESIGN

1.1.1.2.2.1 COMPUTATIONAL PLAN FOR OPTIMIZATION OF THE HPD CELL CONFIGURATION

The optimization of the HPD cell was carried out in four phases (0, 1, 2, 3):

In phase 0, the NETL/FLUENT SOFC electrochemical model was validated for the HPD5R1 cell. In phase I, the effect of the number of air channels (and hence the number of ribs) on the

electrochemical performance of a HPD cell was investigated. The present generation of HPD cells, HPD5R1, with 5 air channels, which have been successfully tested to give enhanced performance (compared to a tubular cell of same active area), will be used as the baseline HPD cell configuration for comparison purposes. Initially, keeping the same cell width, cell thickness, and the cell wall thickness, two-dimensional HPD cell models were developed by varying the number of air channels from 6 – 11 (resulting in HPD6R1 to HPD11R1 configuration cells).

In phase 2, HPD cell configurations were evaluated, based on net performance, manufacturability, and structural robustness.

In phase 3, a complete three-dimensional model of the cell was developed to evaluate its tolerance to thermal gradients in both the cell-testing environment as well as in an in-stack environment. The model includes electrochemistry and the associated axial (as well as cross-sectional) variation of current density.

1.1.1.2.2.2 PHASE 0 - VALIDATION OF NETL/FLUENT SOFC ELECTROCHEMICAL MODEL

1.1.1.2.2.2.1 COMPUTATIONAL MODEL:

Although the NETL/Fluent SOFC model was validated against tubular cell data, it is essential to confirm its validity for a HPD cell, which has a significantly different cross-sectional geometry. Accordingly, the NETL/Fluent SOFC model was employed to compute the performance of a HPD5R1 cell and compare it with the experimental performance data for a HPD5R1 cell. The computational model of the HPD5R1 cell along with the mesh is shown in Figure 1-1. Symmetry about the center plane perpendicular to the long axis of the cell cross-section is utilized to reduce computations. The model is 1 cm in axial length and is essentially a computational analog of an experimental ring cell.

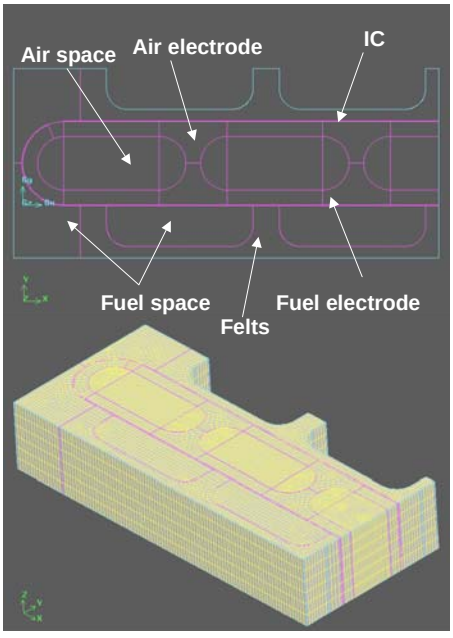

Figure 1-1. Computational model of the HPD5R1 cell

1.1.1.2.2.2.2 BOUNDARY CONDITIONS:

The model anode was flooded with fuel with composition equal to the mean fuel composition for a cell operating at 85% fuel consumption to simulate full utilization. The air channels were also flooded with air with composition equal to the mean air composition for an air stoichs value of 4. In order to eliminate confounding heat transfer effects, the cell was kept isothermal with a prescribed temperature of 1000°C, at which reliable experimental data exist for the HPD5R1 cells. Symmetry of the cell about its midplane was utilized in these calculations.

1.1.1.2.2.2.3 RESULTS

The results obtained from the computational model are shown in Figure 1-2 along with experimental data for a typical HPD5R1 cell. The model is in excellent agreement (within 1%) with the experimental data for current densities between 100 mA/cm^2 to 300 mA/cm^2.

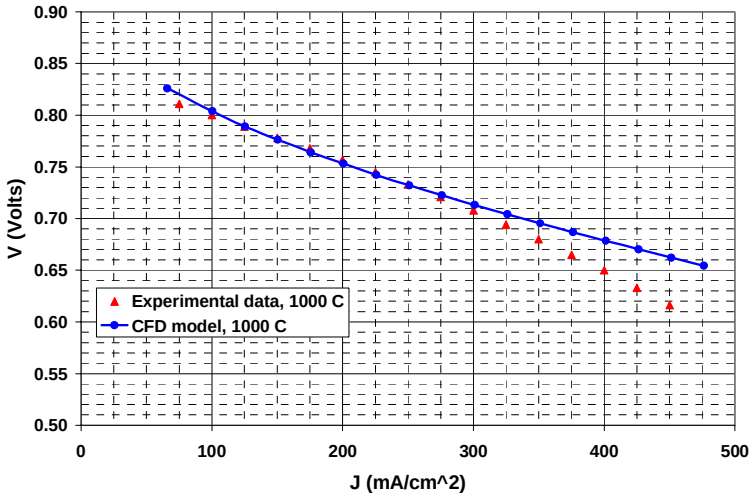

Figure 1-2. Comparison of HPD5R1 model results with experimental data

1.1.1.2.2.3 PHASE 1 - ELECTROCHEMICAL ANALYSIS OF HPDNR1

1.1.1.2.2.3.1 COMPUTATIONAL TECHNIQUE

The cell models will be pseudo-two-dimensional in nature - in essence three-dimensional models of the cells, but only 1 cm long.

1.1.1.2.2.3.2 CELL GEOMETRY

Only the number of air channels will be varied in these models for Phase 1.

Cell width = 101 mm

Cell thickness = 10 mm

The HPD cell configurations analyzed in Phase I are shown in Figure 1-3. By prior experience it was felt that air channels should not have sharp corners and should have full radius to avoid deleterious stresses. The same full radius as that of an HPD5R1 cell was used for the air channels.

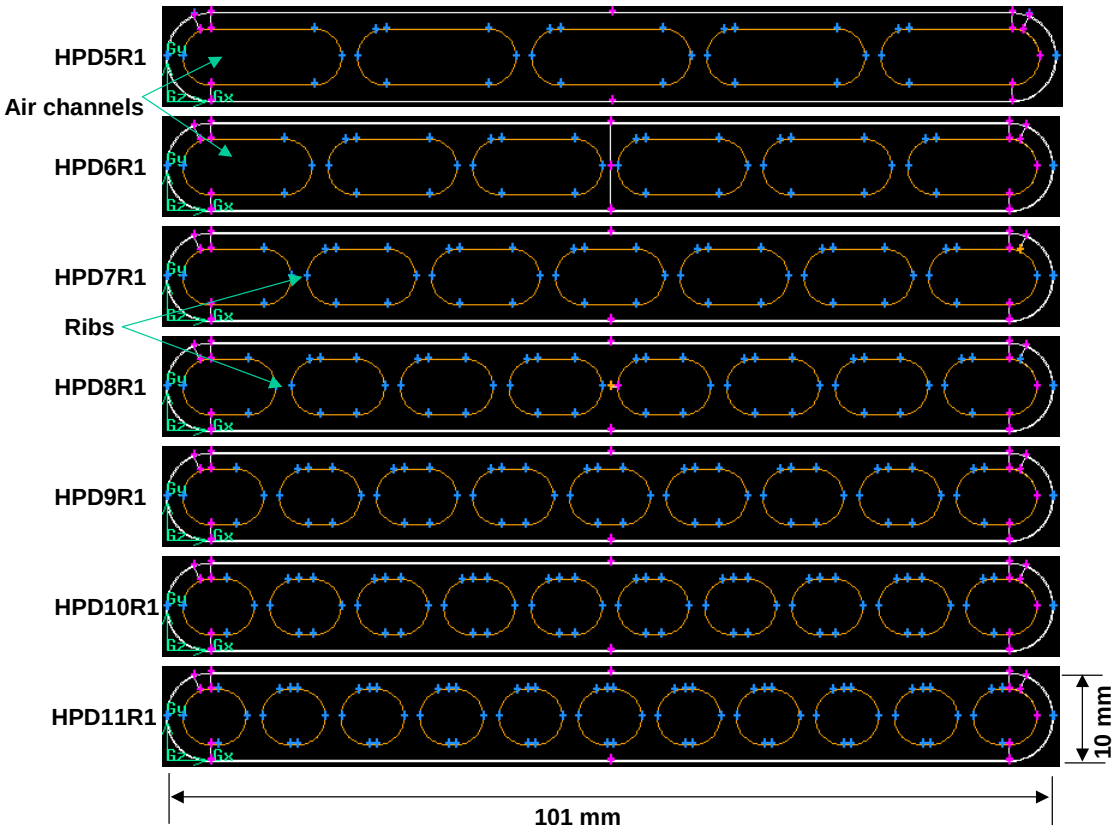

Figure 1-3. HPD cell configurations to be analyzed in Phase 1

1.1.1.2.2.3.3 BOUNDARY CONDITIONS & MATERIAL PROPERTIES

The close concurrence of the HPD5R1 model with experimental data presented in the previous section validates the material properties, which will be used in all the calculations in Phase 1. The boundary conditions will also be the same as in the validation case for all the configurations. Again, wherever possible, symmetry will be utilized of in these calculations.

1.1.1.2.2.3.4 PHASE 1 RESULTS

The V-J data generated using the models for the different HPD configurations at a temperature of 1000 C are summarized in Figure 1-4.

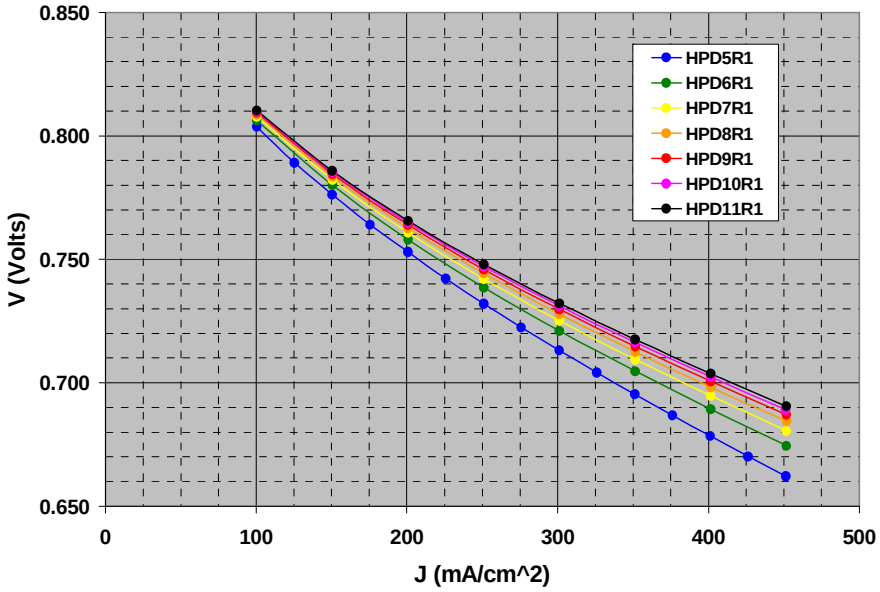

Figure 1-4. Comparison of performance of HPD5R1 to HPD11R1 cells, T_{cell} = 1000°C

At a given current density, the cell voltage increases as the number of channels is increased, as shown in Figure 1-4. The higher the number of channels the higher the number of available parallel current paths and lower is the net cell ohmic resistance.

The pressure drop across the cell also increases with increase in number of channels. However, the pressure drop value is small and the associated increase in parasitic blower power is insignificant.

Although the cell voltage increases with number of channels for a given current density, the relative increase in cell voltage, and, consequently, the relative increase in power per cell, decreases as the number of air channels is increased and follows a typical curve with diminishing returns. It is evident that for the HPD cell configuration used in the current calculation and at T_{cell} = 1000°C, a HPD cell with more than 7 air channels provides little additional benefit from a performance perspective.

The specific power values, power per unit mass, and power per unit volume of the stack of the HPD cells analyzed herein are compared with current tubular cell values in Figure 1-5 for a cell voltage of 0.7 volts. The calculated power enhancement obtained by using a HPD cell over a current tubular cell is also shown in the figure, which indicates that an 85% power enhancement per cell over a current tubular cell can be obtained with a HPD11 cell. The power per unit mass of the HPD cells analyzed are slightly better than that of a tubular cell, with a maximum power per unit mass value that is about 13.5% higher than the value for a current tubular cell. It is also clear that the HPD7 configuration analyzed herein represents an optimum from a power per unit mass perspective. However, as seen from Figure 1-5, a significant advantage of the HPD cells over the tubular cell lies in their higher power per unit stack volume or power density. A HPD11 cell can result in an 82% increase in power density over a tubular cell (the corresponding increase is about 48% for an HPD5 cell).

Increasing the number of air channels does not effect significantly the ratio of maximum current density to mean current density. The maximum current densities occur at locations where the felt connectors attach to the fuel electrode. The felt connector configuration is effective in distributing current uniformly.

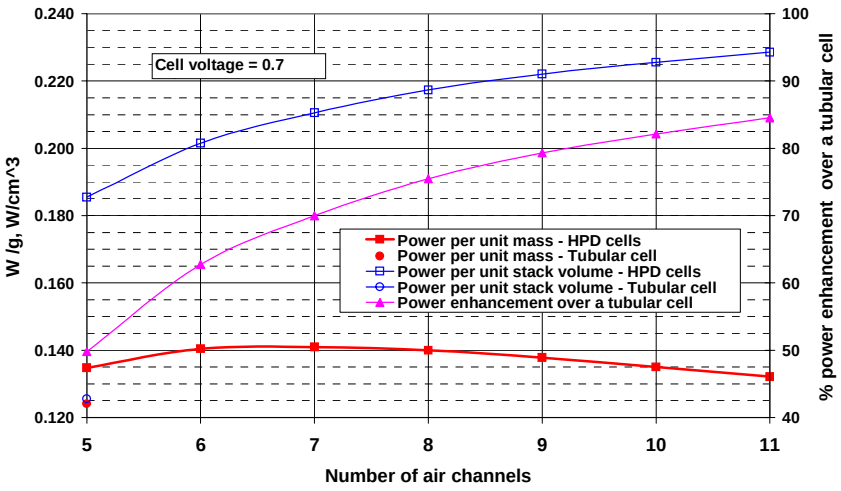

Figure 1-5. Comparison of HPD cells analyzed here with a tubular cell

It is clear that the optimum configuration is dependent on the interplay between the stack cost (related to power density) and the cell cost (related to power per unit mass). In addition, the tolerance to thermal as well as mechanical stresses needs to be taken into account ultimately.

1.1.1.2.2.4 PHASE 2 - ANALYSIS OF ALTERNATIVE HPD CELL DESIGNS

1.1.1.2.2.4.1 GEOMETRIC ALTERNATIVES

A selection of different air electrode cross section designs were modeled and solved for temperature and thermal stress fields. All the configurations analyzed herein feature air electrodes with constant length (25 mm) with these adjacent up-down air channels.

1.1.1.2.2.4.2 SIMULATION DETAILS

Steady-state heat transfer and linear stress analyses are performed on all the cross section designs listed in the previous section. These two analyses performed for each cross section are done sequentially such that the temperature field generated in the steady state thermal analysis is used to generate the thermal stress field. All the analyses are performed using ALGOR finite element modeling software.

1.1.1.2.2.4.3 MODEL ASSUMPTIONS AND BOUNDARY CONDITIONS

This analysis is based on the following assumptions:

1. Air electrode of the cell modeled. Other fuel cell components (for example, fuel electrode, interconnection, etc.) are not modeled.
2. Steady-state thermal analyses based on linear thermal properties for air electrode material.
3. Velocity field is not solved.
4. Effective heat transfer coefficient of 50 W/m^2-K used on the air side. All other boundaries assumed to be adiabatic.
5. Temperature field from the steady-state analysis is used to calculate the stress field.
6. Exact same mesh used for steady-state thermal and linear stress analyses.
7. For the linear stress analyses, the structure is assumed to be fixed at one node (node A) at one end and pinned at one node (node B) at the other end. Although, the node fixed at one end (node A) is allowed to translate along the axis joining the two nodes, node A and node B.

1.1.1.2.2.4.4 RESULTS AND DISCUSSION

1.1.1.2.2.4.4.1 *BASE CASE*

Steady-state thermal analyses and linear thermal stress analyses were performed for the air electrode cross sections. For this base case, air inlet and air outlet temperature was assumed to be 600^{o}C and 1000^{o}C, respectively. It should be noted that 400^{o}C temperature gradient in the inlet and outlet air streams result in 200^{o}C to 220^{o}C temperature gradient in the air electrode with the assumed effective heat transfer coefficient [4W/msqK]. The corresponding thermal stress field data were calculated with the help of the temperature field data obtained from the steady-state thermal analyses. The location of maximum stress is highly dependent on the geometry of the cross section. Indeed, an ‘edge’ or a ‘valley’ in the structure like the one in triangular cross section introduces local stresses in the air electrode. A “twist” phenomenon also can be observed due to the temperature gradient in the two air channels. .

1.1.1.2.3 POC CELL

1.1.1.2.3.1 INTRODUCTION

The SECA POC unit will employ HPD5R1 cells within a generator module that uses air feed tubes. The NETL/FLUENT SOFC model has been validated earlier by comparing results for 1cm long unit cells, both tubular and HPD geometry, with corresponding experimental data. While this is adequate for the purposes of checking the model quickly, it does not simulate the experimental set-up completely. For example, the variation of Nernst voltage, and consequently the variation current density, is not simulated. Hence, a full length HPD5R1 model was developed to match closely the experimental conditions used to generate the V-J for HPD cells.

Also this full length model was then extended to model a cell in a cell-stack to evaluate the nominal design point operation of the SECA POC unit.

1.1.1.2.3.2 EXPERIMENTAL

The computational experiments involved two steps. One, comparing the results for a full length SOFC model with isothermal experimental data, and two application of the calibrated model to the SECA POC unit.

1.1.1.2.3.2.1 COMPARISON OF FULL LENGTH SOFC MODEL WITH EXPERIMENTAL DATA FOR A HPD5R1 CELL

1.1.1.2.3.2.1.1 *MODEL GEOMETRY*

A model that essentially reproduced the experimental set-up used for testing HPD5R1 cells was developed using the CFD software Fluent. The model was generated using Fluent's pre-processor, Gambit 2.1, and is shown in Figure 1-6. Care was taken to resolve various layers of the cell adequately, and the computational mesh, shown in Figure 1-7, included a total of 260341 computational cells. The air feed tube, the felt connectors forming the fuel channels, the busbar, and the powerlead were also included in the model. The fuel electrode, the air electrode, and the interconnect regions were resolved and the electrolyte was approximated as a thin wall.

1.1.1.2.3.2.1.2 MODEL BOUNDARY CONDITIONS

The mass flow rate of air corresponding to 4 air stoichs (experimental conditions) was specified at the air feed tube inlet. The inlet fuel flow rate corresponding to 83% fuel utilization was prescribed at the inlet. The inlet fuel composition was 89 % H_2 and 11 % H_2O. The cell was kept isothermal by prescribing a temperature for all the regions. The computations were carried out at three different temperatures, 1000^{o}C, 900^{o}C, 800^{o}C at which the experimental cell V-J were generated. Note that only half the cell was modeled due to geometrical symmetry.

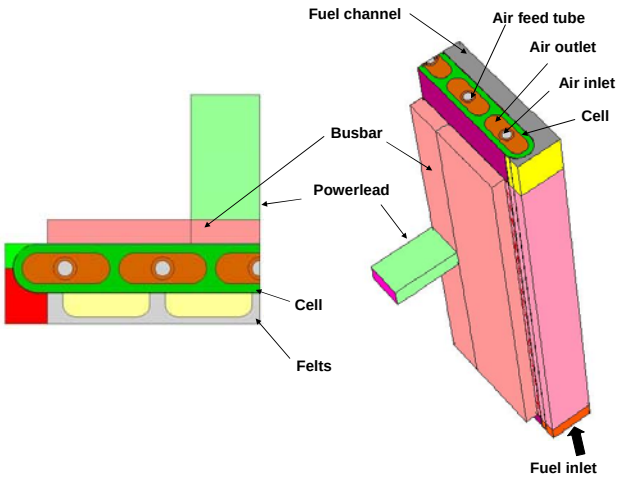

Figure 1-6. Computational model of the HPD5R1 cell – CFD domain

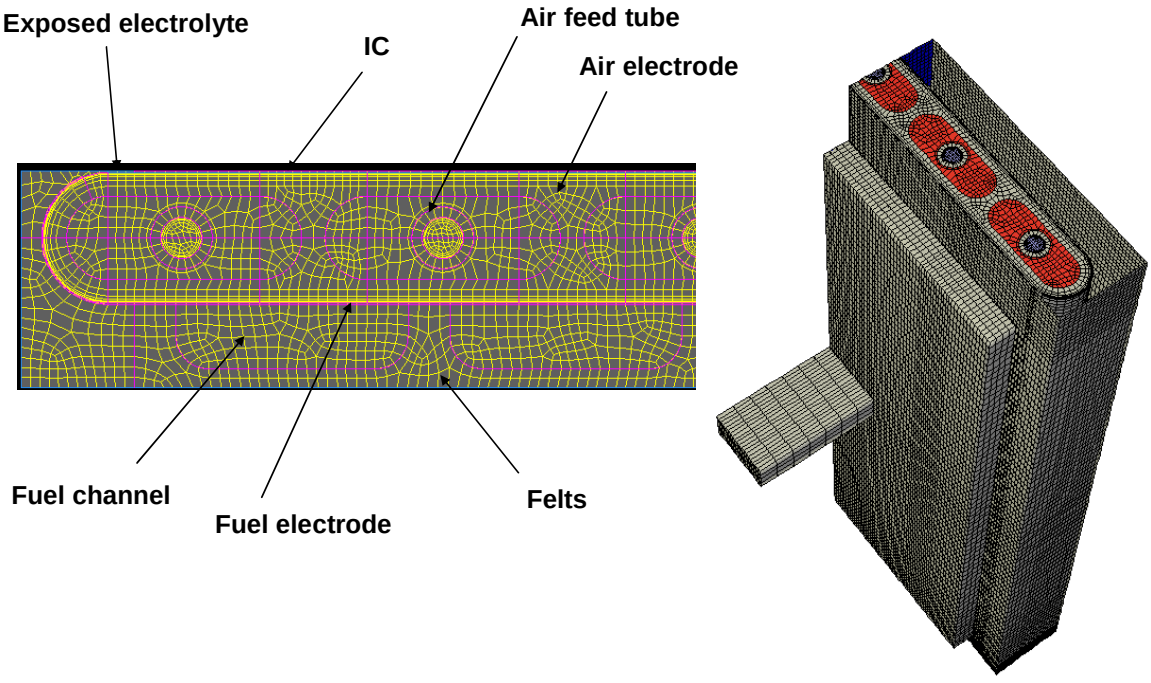

Figure 1-7. Computational mesh

The anode and the IC were assumed to 100 μm thick while the electrolyte thickness was assumed to be about 40 μm. The cathode and anode exchange current densities characterize the net activation loss. However, it is difficult to separate the two exchange current densities

from the net exchange current density. Fortuitously, the activation losses of both the electrodes manifest themselves as voltage drops at the corresponding electrode-electrolyte interfaces. Since the electrolyte layer is very thin, the effect of lumping both the electrode losses into one loss term will have a negligible effect on the spatial current distribution. The anode exchange current density is generally very high (low anode activation loss) in our case. Accordingly, the anode exchange current density was set to a very high value (1e+20 A/m^2). The cathode exchange current density was evaluated by fitting the CFD model results to experimental data at a current density of J = 250 mA/cm^2 for T_{cell} = 1000°C and 900°C, and at a current density J = 200 mA/cm^2 for the 800°C case. Table 1-1 lists the exchange current densities used at different temperatures:

Table 1-1. Cathode Exchange Current Densities at Different Temperatures

Temperature (°C)	Cathode exchange current density (A/m^2)
800	24
900	550
1000	2300

1.1.1.2.3.2.1.3 *RESULTS*

The V-J curves obtained using the CFD model are compared to experimental V-J data at the three different temperatures in Figure 1-8. The model is in excellent agreement with the experimental data at T_{cell} = 1000°C and 900°C. The agreement at T_{cell} = 800°C is not as good for reasons not clear at present. The contours of current density and Nernst voltage on the active region of the electrolyte are shown in Figure 1-9(a) and Figure 1-9(b) respectively corresponding to a mean current density of about 400 mA/cm^2 for T_{cell} = 1000°C. Note that the current density can be as high as 693 mA/cm^2 at the closed end for this case. The electrolyte current density vectors and the air electrode voltage contours are shown in Figure 1-10(a) and Figure 1-10(b).

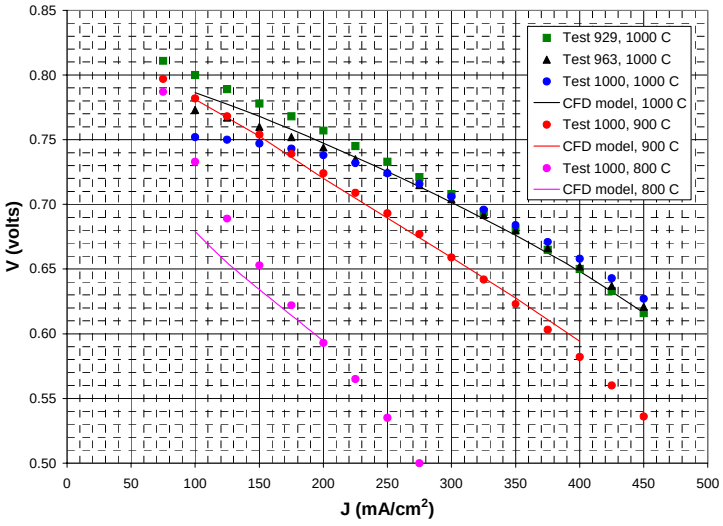

Figure 1-8. Comparison of isothermal HPD5R1 V-I with experimental data

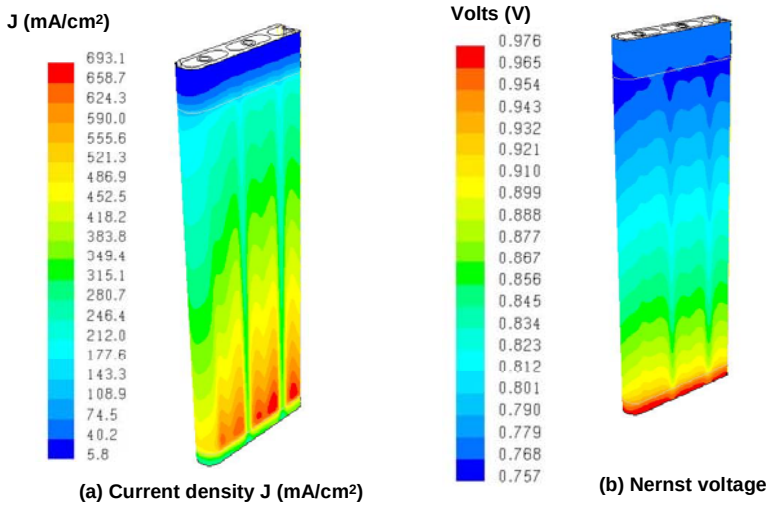

(a) Current density J (mA/cm²) (b) Nernst voltage

Figure 1-9. Contours of current density and Nernst voltage at a mean current density of 400 mA/cm^2 at T_{cell} = 1000^{o}C

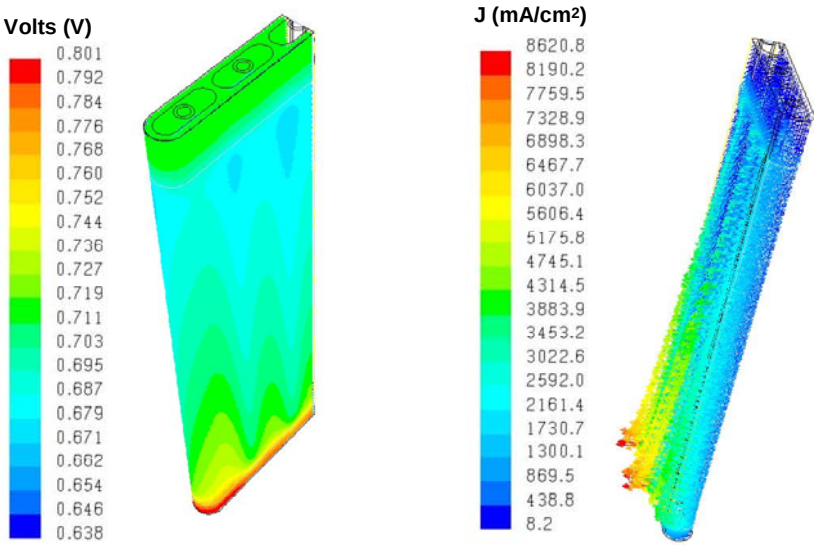

(a) Voltage contours (b) Current density vectors

Figure 1-10. Voltage contours and current density vectors in the air electrode at a mean current density of 400 mA/cm^2 at T_{cell} = 1000^{o}C

1.1.1.2.3.2.2 EVALUATION OF PERFORMANCE OF A HPD5R1 CELL IN THE SECA POC GENERATOR

The model described above, which represents a peripheral cell in the SOFC stack with no heat loss, was employed to simulate the performance of the cell in the SECA POC generator. To simulate a cell in the center of the stack, periodic boundary conditions are needed, which are not supported currently by the Fluent/NETL SOFC model. The SECA POC design features an anode gas recirculation loop that aids in the reformation of incoming fuel which feeds reformed fuel (corresponding to Pittsburgh natural gas) into the cell stack.

1.1.1.2.3.2.2.1 MODEL BOUNDARY CONDITIONS

The calculations were carried out for a cell current of 220 A (mean J ≈ 240 mA/cm^2), the design point for the SECA POC generator. The fuel was assumed to be fully reformed before it enters the cell, and its composition at inlet was computed based on 85% fuel consumption along with a recirculation rate that results in a 2.1 O_2 to C ratio in the pre-reformer (typical values used to prevent carbon formation in conventional SWPC SOFC generators). The fuel inlet temperature was assumed to be 700^{o}C based on previous calculations. The mass flow rate of air and the air inlet temperature were varied manually, based on previous experience, to limit the maximum temperature to less than 950^{o}C while maintaining a cell average temperature of about 900^{o}C. Table 1-2 lists the fuel and air composition used in these calculations.

Table 1-2. Fuel and Air Compositions at Corresponding Inlets

Boundary	Temperature	Species mole fractions					
	C	H_2	CO	H_2O	CO_2	O_2	N_2
Inlet to AFT	Varied	-	-	-	-	0.21	0.79
Fuel inlet to cell	700 C	0.428	0.181	0.214	0.148	-	0.028

The CFD domain was assumed to be adiabatic – there is no heat loss or heat addition. The net waste heat produced by the cell is carried away only by air and fuel.

Radiation heat transfer was modeled using Fluent's comprehensive Discrete Ordinates model. The cathode, the anode, and the felts were assumed to be nearly opaque with an absorption coefficient of 4e06 1/m. The electrolyte was modeled as a gray body with an emissivity of 0.9. The alumina air feed tube was assumed to have an emissivity of 0.52. An emissivity of 0.1 was used for the nickel busbars and powerleads.

1.1.1.2.3.2.2.2 RESULTS

The computed contours of temperatures and current density on the electrolyte face are shown in Figure 1-11(a) and Figure 1-11(b) for an air flow rate of 8 stoichs at a cell current of 220 A (mean J ≈ 240 mA/cm^2). The air inlet temperature was 607^{o}C. It clearly shows that the current density is maximum near the closed end. The temperature distribution is nearly uniform across the cell (in the transverse plane), as anticipated, since all the channels are similar. Further, radiation plays a significant role in smoothing the temperature distribution. The variation of the electrolyte temperature, the current density, and the Nernst voltage along the cell length (z direction) is shown in Figure 1-12. Note that all the points in the x-y plane corresponding to a z co-ordinate are plotted at this value of z co-ordinate. The maximum cell temperature is about 943^{o}C and the volumetric average of the cell temperature is about 900^{o}C. The cell voltage is about 680 mV, which is slightly below the cell voltage at a current density of J ≈ 240 mA/cm^2 for a cell operating isothermally at 900^{o}C (see Figure 1-8), which serves as a good check of the model. The air temperatures in the annulus between the AFT and the cell, and the air temperatures in the AFT are shown in Figure 1-13.

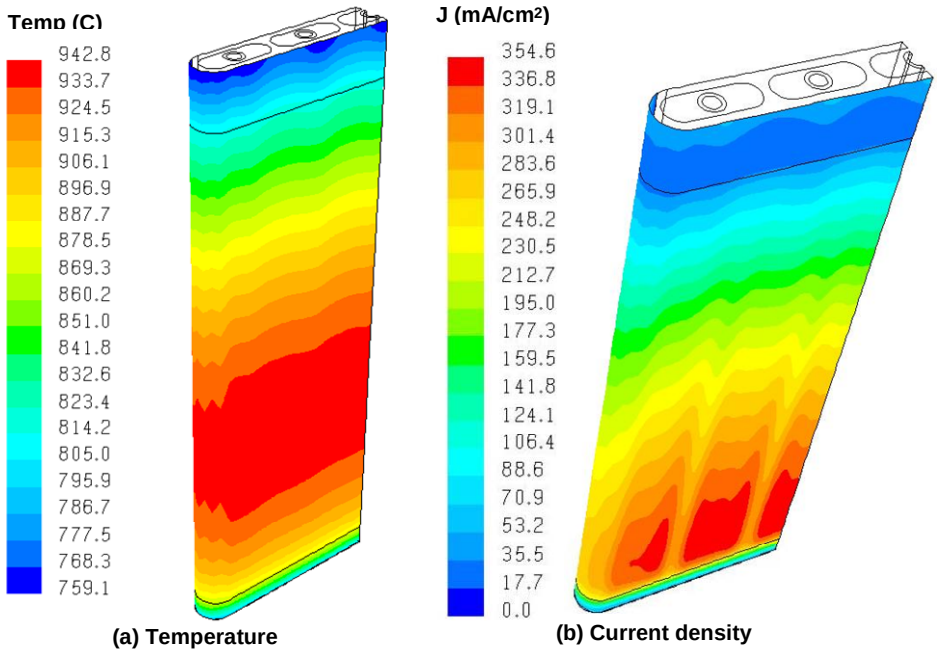

Figure 1-11. Temperature and current density contours on the electrolyte (I = 220 A, air stoichs = 8, $T_{air\text{-}in\text{-}cell}$ = 607^{o}C)

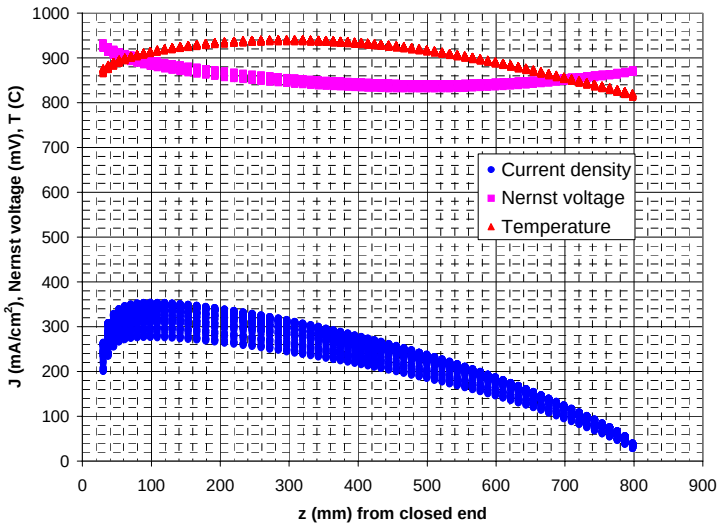

Figure 1-12. Variation of electrolyte current density, Nernst voltage, and temperature along the cell length

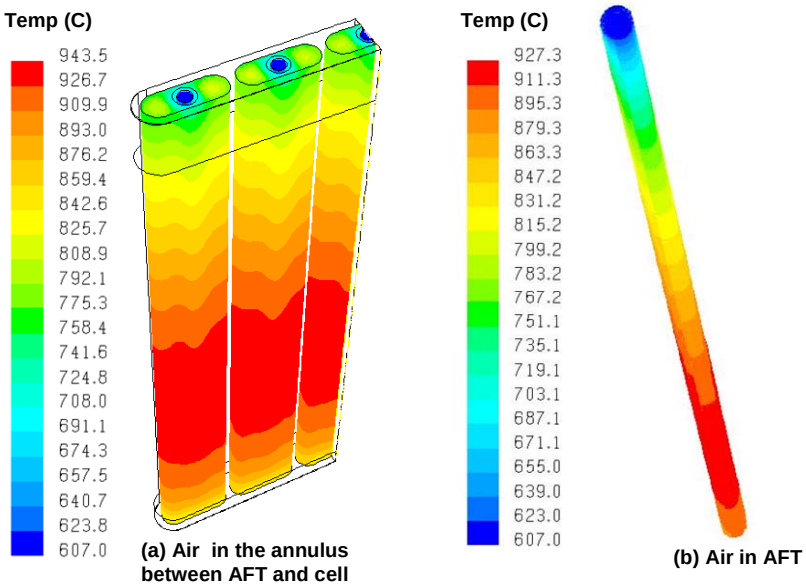

Figure 1-13. Air temperatures in the annulus between the air feed tube and cell and in the AFT

These computations refine preliminary estimates of cell performance in the SECA POC generator at its nominal operating point. It has to be pointed out that these computations are

amongst the most extensive computations carried out for this cell geometry till date. The Fluent/NETL SOFC model is a robust tool for these comprehensive computations. Although the computational times are not prohibitory, a simpler radiation model (relative to the computationally intensive DO radiation model) would considerably reduce the computational time.

1.1.2 HPD CELL DESIGN

In general this issue is covered in the discussion of Section 1.1.1.

1.1.3 LOW-COST AIR ELECTRODE MATERIAL DEVELOPMENT

1.1.3.1 *Introduction*

The cathode material presently used in the Siemens Westinghouse tubular SOFC was developed for use with the EVD electrolyte process and for operation at 1000°C. With the move towards lower operating temperatures and with the replacement of EVD with a plasma spray electrolyte process, there is opportunity to make significant performance improvement and cost reduction through the development of a new cathode material.

1.1.3.2 *Experimental*

In this task three different compositions are being prepared with higher levels of calcium doping than currently used. The compositions will be evaluated based on their physical properties, compatibility with plasma spray based cell processing, cell electrical performance, and raw materials cost.

1.1.3.3 *Results And Discussion*

Initial electrical test results for cell Y1B043 are shown in Figure 1-14. After ~360 hours of testing at 1000°C the cell has achieved 0.630 V at a current density of 300 mA/cm^2 and a fuel utilization of 82.6%. One of the more interesting observations thus far has been a very small conditioning effect compared to that normally seen in cells with standard cathodes.

Microcharacterization results are shown in Figure 1-15. X-ray spectroscopy analysis (Figure 1-16) indicates some calcium penetration into the electrolyte. This may indicate that the densification temperature for the electrolyte is too high and that the standard cell processing conditions may need to be modified for the new cathode.

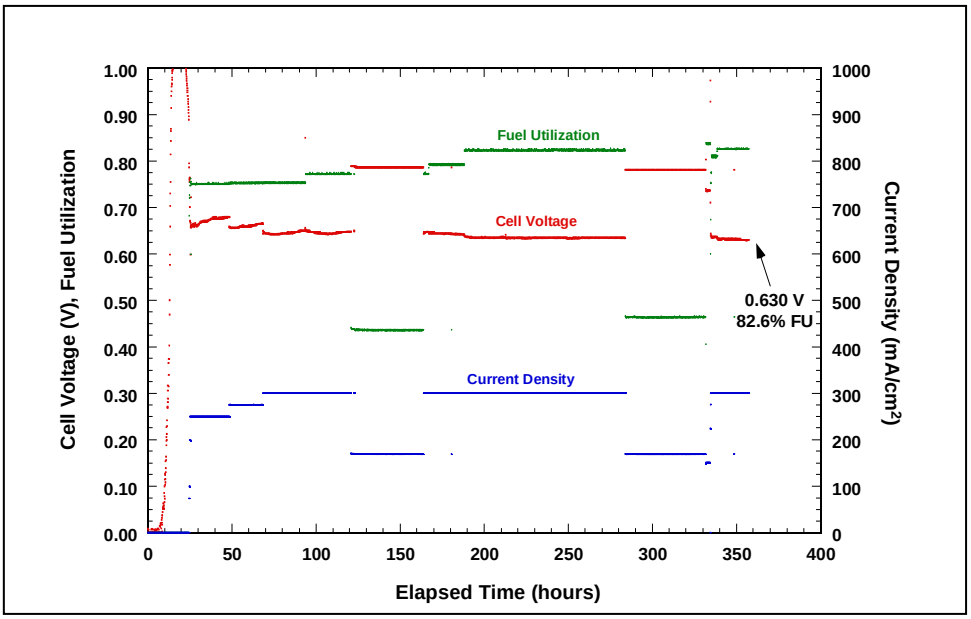

Figure 1-14. Cell test data versus time plot for cell Y1B043

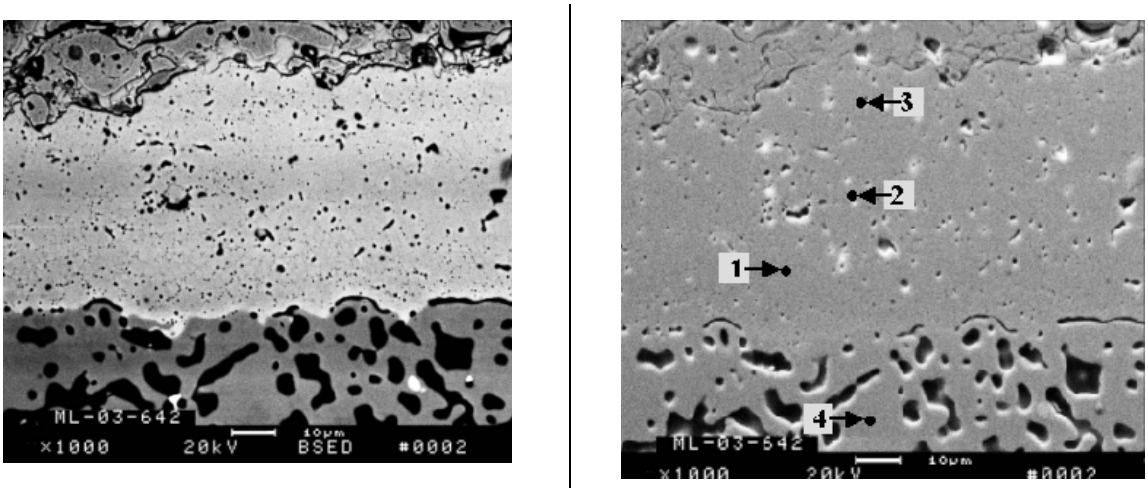

(a) (b)

Figure 1-15. SEM micrographs from an untested portion of cell Y1B043: (a) Back-scattered electron image showing anode at top, electrolyte at center, and cathode at bottom. (b) Secondary electron image of same region. Markers indicate regions from which the x-ray spectra in Figure 1-19 were taken

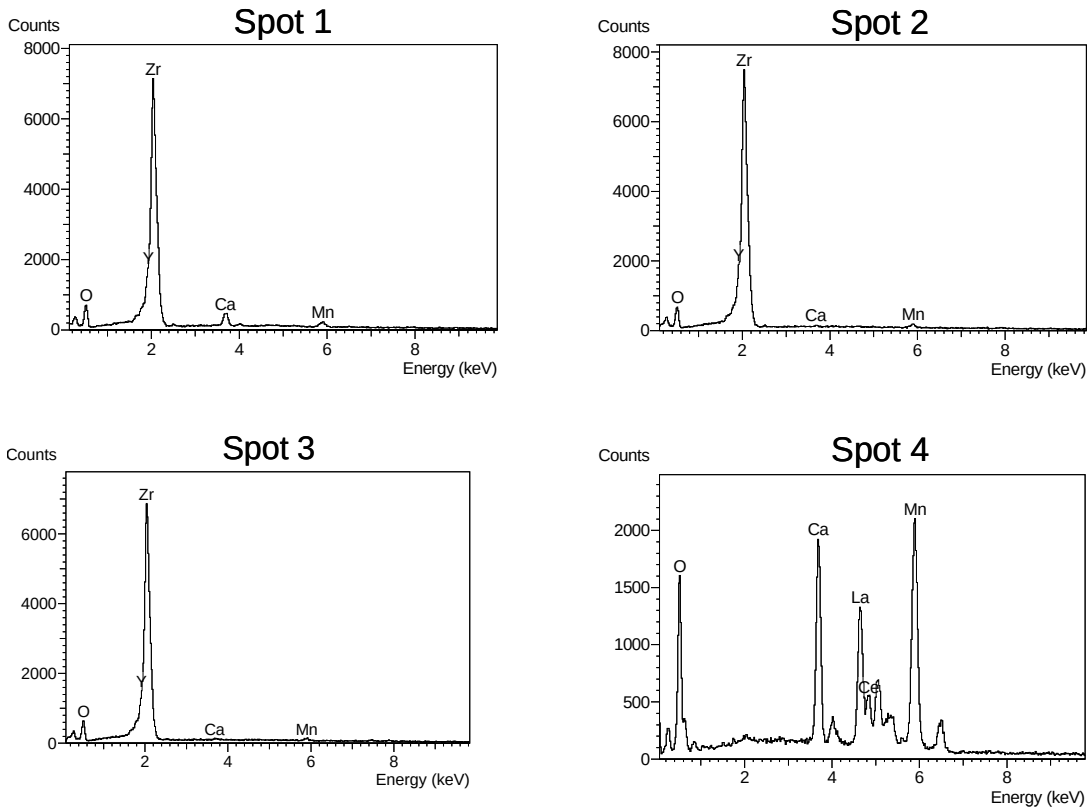

Figure 1-16. X-ray spectra from the locations indicated in Figure 1-15a

1.1.4 HPD CATHODE TUBE

1.1.4.1 *HPD5R1 Tube Fabrication Development – Closed End Application*

1.1.4.1.1 Introduction

In order to manufacture HPD geometry cathode tubes, a separate piece must be attached to the tube to close one end. The quality of the bond between the closed end piece and the tube has been a problem as has the quality of the end piece itself.

1.1.4.1.2 Experimental

There are two steps to the closed end application process: (1) re-hydrating the surfaces to be bonded and (2) applying force to form the bond. In order to address the closed end attachment issues both the steps were re-evaluated. A new process for re-hydrating the surfaces was developed. This process provides a higher degree of hydration while minimizing the free water at the surface. In the force application step, experiments were conducted to compare the effectiveness of the hydraulic press versus clamps.

The pieces used to make the closed ends are extruded separately from the rest of the HPD tube. The poor quality of these closed end pieces was addressed by redesigning the extrusion die. The die opening and cross-section of the closed end piece stayed the same, but the flow paths and interior dimensions of the die were changed.

1.1.4.1.3 Results and Discussion

The new technique for re-hydrating the surfaces was very successful. The elimination of free water from the bonding surfaces allows for easy visual inspection of the bond before it dries. When closed end piece and tube are forced together, one can observe extrusion of material all around the seam (Figure 1-17). A continuous ring of extruded material at the seam appears to be a requirement for a quality bond.

Previously, it had been determined that better closed ends were produced using a hydraulic laboratory press to bond the tube and closed end piece as opposed to using elastic bands or clamps. The biggest advantage of the press is that the applied load is known and can be easily controlled. The disadvantage of using the press lies in the potential for the tube to buckle during closed end attachment. Because of the wide and flat geometry and the overall length (> 1m in the green state) of the HPD5R1 tubes, buckling is likely when the tube is loaded in uniaxial compression (Figure 1-18). Slight buckling to either side results in an uneven bonding force during closed end attachment with one side having a greater bonding force than the other. Results with the press while excellent in many cases were too inconsistent. The use of clamps to apply the bonding force gave much more consistent results. Closed ends applied using clamps and the new re-hydration technique have consistently passed the closed end proof test.

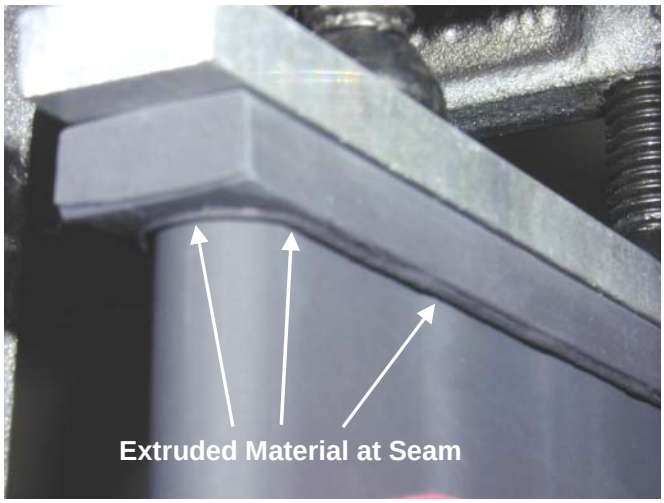

Figure 1-17. Extrusion of material from the seam during closed end bonding using clamps

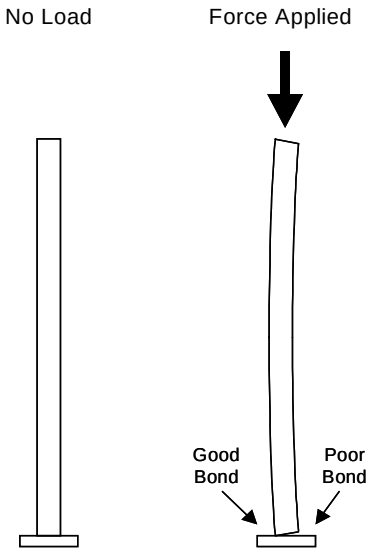

Figure 1-18. Illustration of buckling and its effects on bonding during closed end attachment using a hydraulic laboratory press

The extrusion die modifications were very successful in improving the quality of the extruded closed end pieces. Figure 1-19 compares microstructures of sintered closed end pieces. The defects common with the old die are now absent in pieces extruded with the new die.

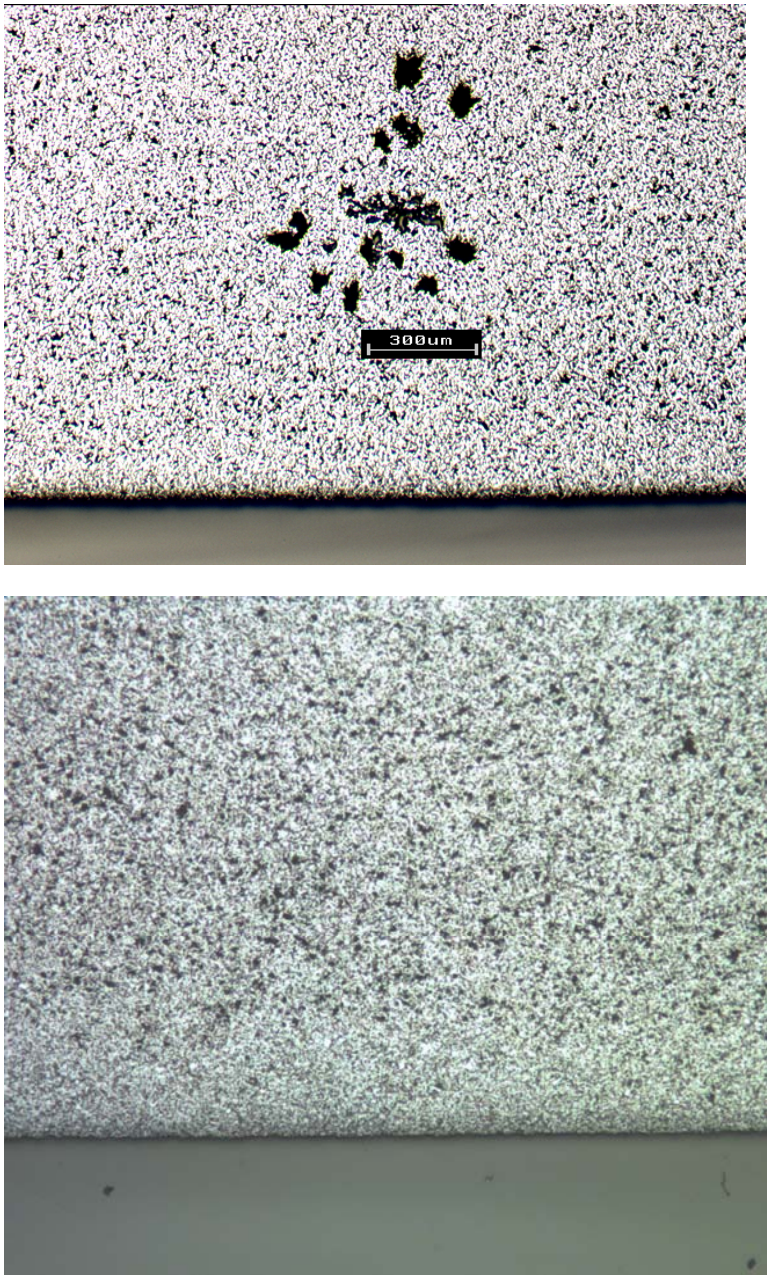

Figure 1-19. Optical micrographs showing cross-sections of sintered closed end pieces for HPD tubes: (top) before die improvements and (bottom) after die improvements

1.1.4.2 *DEVELOPMENT OF QC TECHNIQUES*

1.1.4.2.1 Experimental

A closed end proof test has been developed and implemented for HPD5R1 tubes. This step ensures the strength of the closed end cap to be acceptable for cell processing and generator operation. An external visual inspection is done to guarantee the integrity of the tube as well. In addition, an internal visual inspection is conducted by means of a borescope. The tube dimensions are checked by means of a 3D box and channel inserts to ensure that the tolerances for generator assembly are met.

1.1.4.2.2 Results and Discussion

The criterion for the proof test is to apply 4.5MPa of pressure, or about 10% of the tube strength, internally in each channel at the end cap and in separate steps. In case the strength bond of the end cap is very weak, this test can repeatably identify poor seams by removing the cap altogether. Obviously, if the tube fails the proof test such tube does not proceed for cell processing. In addition, the proof test has been used to identify the best conditions for applying the closed end cap.

A rigorous external visual inspection has been implemented before tubes proceed for cell processing. This step ensure that any flaws, such as cracks, are identified early on so that no value is added to a tube which may not survive cell processing of electrical operation. In addition, an internal visual inspection is conducted by means of a boroscope. Similarly this test intends to remove tubes with detrimental flaws from cell processing.

The final tube QC check is its dimensions. This test is done with a 3D box where the tube is fitted. This step eliminates tubes which are not reasonably straight or with significant bowing. A minimum channel height has been determined to allow enough clearance for the Air Feed Tubes. These steps ensures that the tolerances are met for generator assembly.

1.1.4.2.3 Conclusion

Quality Control techniques have been implemented in tube manufacturing in order to minimize the risk of cell failure during generator operation. In addition, such QC steps identifies flaws early on in the processing steps and no value is added to a tube of poor quality. Tube dimensions are measured in order to comply with the tolerances required for generator assembly.

1.1.4.3 *HPD Delta9 Tube Making*

Through August 2006 a total of 81 Delta-9 cathodes were fabricated to support plasma spray development for the Delta- 9 geometry. A new grit blaster procured earlier in 2006 facilitated the production of Delta-9 cathodes.

HPD10 tubes have also been made using the “Y4” cathode material.

1.2 LSGM-BASED FUEL CELL DEVELOPMENT

1.2.1 LSGM ELECTROLYTE DEVELOPMENT

1.2.1.1 *Introduction*

Research activities were directed towards investigating the effects of plasma spraying parameters, the chemistry of feedstock powder and substrate heating on the properties of the sprayed LSGM films. Four matrices, designated as Matrix-2, -3, -4 and –5, were designed to achieve these goals in addition to Matrix-1 that has been reported in the 2nd semiannual report. To be specific, Matrix-2 aims at a systematic study on gun power, Ar-gas flow, powder feeding rate and number of revolutions; Matrix-3 compares the effect by Ga_2O_3 compensated LSGM feedstock; Matrix-4 studies plasma spraying modified LSGM power with the optimized parameters on the heated substrate (<300^{o}C); Matrix-5 covers plasma spraying with a new type of gun anode.

1.2.1.2 Experimental

1.2.1.2.1 ADJUSTMENT OF LSGM FEEDSTOCK CHEMISTRY

Approximately 5 mol% Ga_2O_3 in the LSGM feedstock is lost during plasma spraying due to the formation of gaseous phase Ga_2O. This loss of Ga is also predicted by the thermodynamic calculation as will be shown later. To compensate the loss, a new batch of LSGM powder with modified composition, $La_{0.8}Sr_{0.2}Ga_{0.9}Mg_{0.2}O_{3-\square}$, was ordered from the supplier and utilized in most of plasma spray practice. In general, the powder is free flowing and has a d_{50}~23 μm.

1.2.1.2.2 PLASMA SPRAYING LSGM THIN-FILM

The plasma spraying practice from Matrix-2 to Matrix-4 used regular gun-anode 730. The details on the plasma spraying has been described in the last semiannual report. In an effort to reduce the temperature gradients during plasma spraying, one approach used in this study is to reduce the plume temperature by using a new-type of gun-anode known as 484 that is specially designed for spraying low-melting point materials. With this new gun-anode, the plume diagnosis revealed approximately 100^{o}C and 60 m/s lower plume temperature and particle velocity, respectively, than the regular 730 anode. The optimized spraying condition was finalized to be: gun power level 10 kWe, primary gas Ar flow 45 splm, powder feeding rate 8 grams/min, and a 7-layer deposition. No secondary gas such as H_2 is used due to the concern of excessive reduction of Ga_2O_3.

The tube substrates were chosen from newly developed composition thermally matched to the LSGM. Both fully sintered and bisque-fired tubes were used, and in some cases coated with Tb-doped CeO_2 interlayer prior to plasma spraying. The shrinkable feature of bisque-fired substrate is expected to allow a better densification of LSGM electrolyte during post-spray heat treatment step.

The substrate temperature has also been studied as an important variable. Several approaches were adopted in this study, *i e.*, plume heating and inner cartridge heater. In every case, no cooling air was used during plasma spraying.

1.2.1.2.3 POST SPRAY HEAT TREATMENT

Another effort to make a gas-tight LSGM film was the post-spray heat-treatment, *i. e.*, to infiltrate LSGM suspension into pre-existing cracks in as-sprayed LSGM films, followed by heat treatment at higher temperatures. At a temperature greater than 1500^{o}C, the leak rate of the LSGM film has been found to be dramatically reduced to a level where a single-cell test is possible.

On the other hand, to better understand the mechanism of crack propagation upon heat-treatment, the microstructural evolution of LSGM thin-films that were annealed from 400 to 1200^{o}C were also studied.

1.2.1.2.4 CHARACTERIZATION OF AS-SPRAYED LSGM

The as-sprayed LSGM film together with the substrate was cut, mounted and polished for microscopic observation. To discern secondary phases and micro-cracks, both secondary and back-scattered electron-images were taken for the same sample. If necessary, the EDX was also applied to identify the constituent of secondary phases.

For any given sample, window vacuum leak rates were measured on three locations of a 3”-long sample, each 120^{o} apart, along the circumference. An average of three readings was reported as the final window leak rate.

Since the chemistry of as-sprayed LSGM strongly depends on the APS conditions and would potentially affect the electrical conductivity and thermal expansion, the powder of as-sprayed LSGM were intentionally collected and analyzed by ICP and XRD to determine the chemical composition and crystal structure. These data were compared with the original LSGM feedstock powder so as to estimate the amount of Ga loss during the spraying and the change in crystal structure.

The dilatometric property of as-sprayed LSGM pellet was measured with the standard dilatometer available inside the company from room temperature to 1000^{o}C in air.

The ionic conductivity of as-sprayed LSGM film was determined by AC impedance technique from 700 to 900^{o}C in air. Pt mesh/paste was used to serve both as counter electrode and current collector.

1.2.1.2.5 SINGLE CELL TEST

The ring-type fuel cell testing was conducted in a specially designed test rig that separates air from fuel. Because of no closed-end on the ring sample, a sealant has to be used. For this test, two gold foils in a ring shape were applied to the both ends of the ring sample, followed by clamping between two Al_2O_3 end plates. To reinforce the sealing, additional Al_2O_3 cement was applied along the gaps. A schematic of the testing assembly is illustrated in Figure 1-20. The

whole test article was then spring-loaded to ensure no cracking of the cell during heating or cooling step. A thermocouple was also placed near the ring-cell to indicate the true temperature of the cell. To simplify the first test and have a fair evaluation of plasma-sprayed LSGM properties, no interconnection was used in this test. Pt was used as the anode as well as current collectors for cathode and anode. The cathode current collector was placed in a position opposite to Pt anode across the tube wall. The effective area of the cell was limited to 1 cm^2.

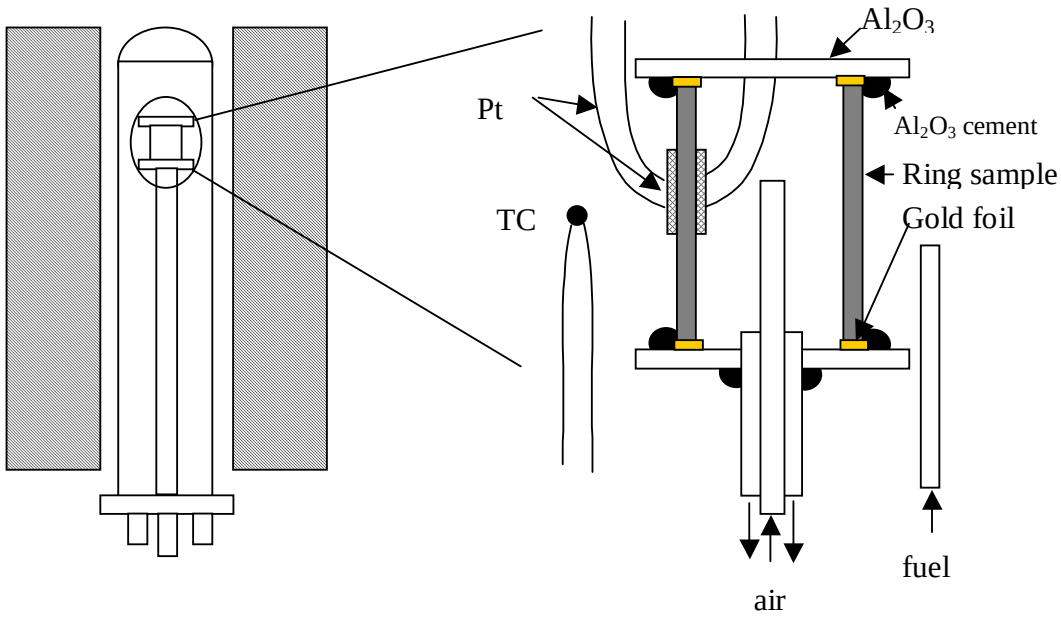

Figure 1-20. Schematic of ring-cell testing setup

The assembled test article was then loaded into a muffle tube with a flange-gasket seal at the bottom of the muffle tube, followed by loading into a vertical furnace. The test started with flowing air inside the article and ($4\%H_2+N_2$)+$3\%H_2O$ (cover gas)) mixture outside the article as the temperature was ramped up to 900°C. Upon reaching 900°C, the cover gas was switched to H_2 saturated with $3\%H_2O$. To maintain a minimal pressure differential across the cell, a flow rate, approximately 180 sccm, was set for both air and fuel. During cell heat-up and switchover of gases, the cell OCV was continuously recorded to monitor any variations. To evaluate the cell performance, a constant current was also applied across the cell at various level to observe the responding cell voltage.

1.2.1.3 *Results And Discussion*

1.2.1.3.1 THERMODYNAMIC CALCULATION OF GA VAPORATION

Gallium oxide, Ga_2O_3, as one of the major components in the newly developed electrolyte LSGM for low-temperature SOFCs, has a thermodynamic potential of being reduced to gaseous Ga_2O during plasma spray and further lost. The consequence of Ga-loss is significant because

it could alter the original LSGM composition, leading to appearance of second insulating-phases and therefore lower ionic conductivity in the as-sprayed LSGM layer.

The chemical reaction that causes the loss of Ga is expressed by:

$$(Ga_2O_3)_{\text{ in LSGM}} = Ga_2O_{(g)} + O_{2(g)} \quad (1)$$

$$K = \frac{P_{Ga_2O} P_{O_2}}{a_{Ga_2O_3}} \quad (2)$$

where K is the chemical equilibrium constant; $(Ga_2O_3)_{\text{in LSGM}}$ represents a dissolving state of Ga_2O_3 in LSGM with a chemical activity of a_{Ga2O3}; P_{Ga2O} and P_{O2} are the partial pressures of Ga_2O and O_2, respectively. Recent serial publications[1, 2] on thermodynamic properties of LSGM material by Professor Hilpert's group using Knudsen Effusion Mass Spectrometry in Research Center in Jülich provided valuable thermodynamic data for this analysis. The chemical equilibrium constant K and Gibbs free energy change μG^o of reaction (1) are given as a function of temperature T by

$$\ln K = -\frac{124145(\pm 4685)}{T} + 48.384(\pm 2.896) \quad (3)$$

$$\Delta G^o = 1032141 - 402.265 * T \qquad \text{(Joules/mole)} \quad (4)$$

Based on equations (2) and (3), the partial pressure of Ga_2O can be calculated as a function of temperature and partial pressure of O_2. The activity of Ga_2O_3 in LSGM was taken as 0.0025 (1800 K) as suggested by reference (1) and assumed in the paper to be insensitive to temperature. The results were graphically shown in Figure 1-21 in a temperature range close to plasma plume average temperature. As expected, the partial pressure of Ga_2O increases with temperature and with decreasing Po_2. Under plasma spray condition (~2200-2400^{o}C and Po_2=0.21 atm), the magnitude of Ga loss is significant considering the high primary gas flow rate. However, the kinetic rate for Ga vaporization under the plasma spray condition that determines the actual amount of Ga loss is unfortunately unknown at present time.

[1] W. Kuncewicz-Kupczyk et al, "Vaporization studies of the La_2O_3-Ga_2O_3 system", *J. Am. Ceram. Soc.*, 85(9) 2299-305 (2002)
[2] W. Kuncewicz-Kupczyk et al, "Vaporization of Sr- and Mg-doped lanthanum gallate and implications for solid oxide fuel cells", *J. Elechem. Soc.*, 148(6) E276-E281 (2001)

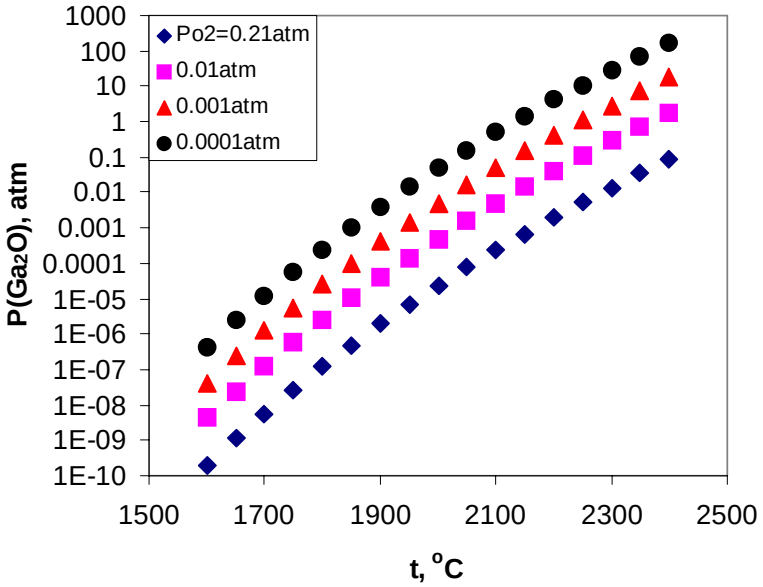

Figure 1-21. Plot of P_{Ga2O} as function of temperature and Po_2

1.2.1.3.2 WINDOW LEAK RATE

The window leak rate (WLR) measured at room temperature was used as an evaluation criterion for optimizing the plasma spraying parameters. Figure 1-22 shows the variation of WLR with the gun power at fixed primary Ar gas flow, powder feed rate and thickness, as a part of Matrix-2 study. It is evident that 10 – 15 kWe of gun power yields the lowest WLR, and is therefore taken as the optimized parameter. This set of parameters is adopted in the following study.

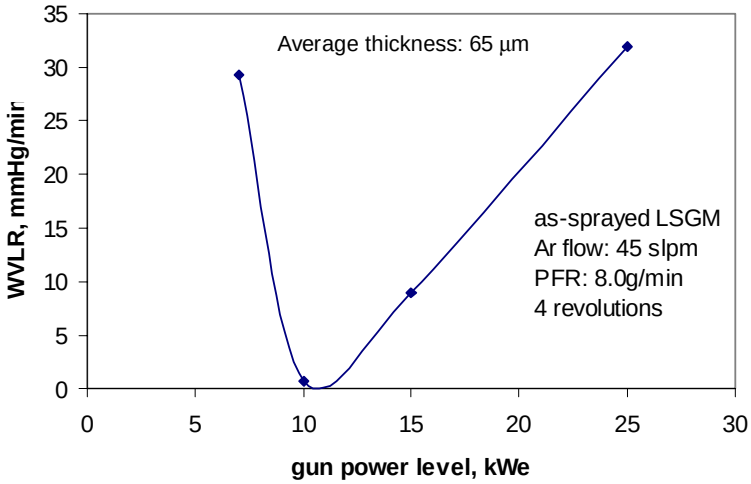

Figure 1-22. Variation of window leak rate with gun power

1.2.1.3.3 MICROSTRUCTURE OF LSGM FILMS AND EVOLUTION WITH TEMPERATURE

A little benefit with higher substrate temperature (~250^{o}C) can be seen in Figure 1-23, where the microstructures of LSGM sprayed on (a) unheated and (b) heated substrates (~250^{o}C). The cracks in LSGM with heated substrate appears to be less in number but larger in width than that without substrate heating. The banding is found by EDX to be Ga-depleted phase, indicating loss of Ga during plasma spraying occurred.

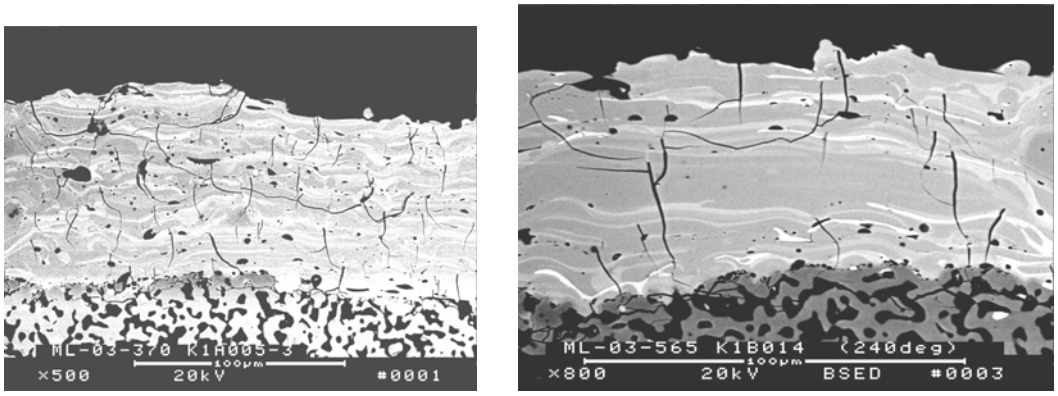

(a) (b)

Figure 1-23. **Comparison of Microstructures of LSGM films sprayed on (a) unheated and (b) heated substrate (250^{o}C) with parameters of 15 kWe, 45 slpm Ar, 8g/min powder feed rate and 4 layers. LSGM feedstock is not Ga_2O_3 compensated**

Another unique feature of plasma sprayed LSGM is the propagation of cracks upon heat-treatment. Figure 1-24 shows the microstructural evolution of LSGM films as a function of annealing temperature. The real visible change is clearly seen to occur at above 600^{o}C, which features coarsening of the microstructure and enlargement of pre-existing cracks. Disobeying to traditional sintering theory, cracks become larger and larger as the temperature increases. No sign of crack healing expected by solid state diffusion can be found from Figure 1-24.

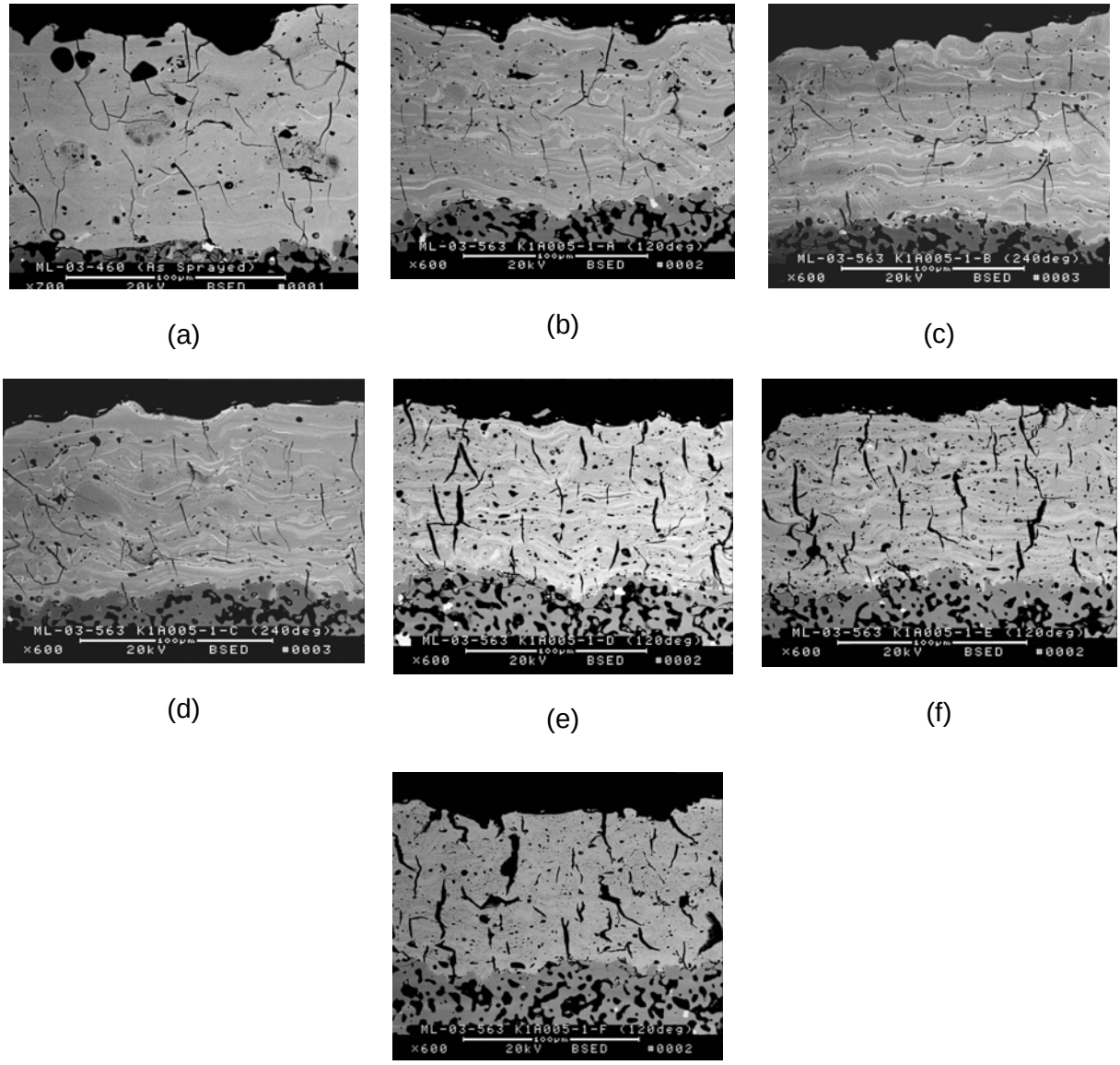

Figure 1-24. Microstructural evolution of LSGM films as a function of temperature. The duration for each temperature was fixed at 4 hours (a) as-sprayed, (b) 200°C, (c) 400°C, (d) 600°C, (e) 800°C, (f) 1000°C and (g) 1200°C

The microstructure of LSGM film produced by new gun anode 484 is shown in Figure 1-25. Compared with Figure 1-23, the number of cracks in Figure 1-25 is apparently lesser. This reduction in cracks is believed to attribute to lower plume temperature produced by anode 484.

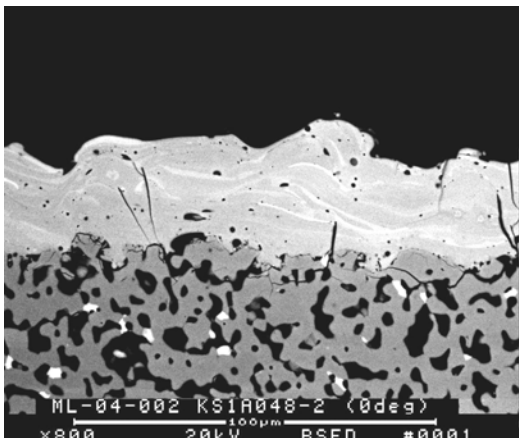

Figure 1-25. Microstructure of LSGM layer sprayed with new anode 484. The plasma spraying parameters are 30 kWe, 65 slpm AR, 8g/min powder feed rate and 4 layers

As one of approaches to eliminate the cracks, the as-sprayed LSGM layer was first annealed at 1000^{o}C for 4 hours, followed by vacuum infiltration of LSGM suspension. Thus treated LSGM/substrate was then finally sintered at 1500^{o}C for 4 hours. The microstructure is shown in Figure 1-26, where a dense LSGM layer is clearly seen with the presence of darker discrete phases embedded in the matrix. The composition of the darker phase was found by EDX to be Ga-depleted phase , and more importantly, an extensive Mn-Ga interdiffusion was observed around the interface region. The same sample was also used for single cell testing. The observation by Figure 1-26 suggests that high sintering temperature can eventually heal all cracks in the LSGM layer, but it has to pay the price of extensive cation diffusion, which leads to the change of chemical composition.

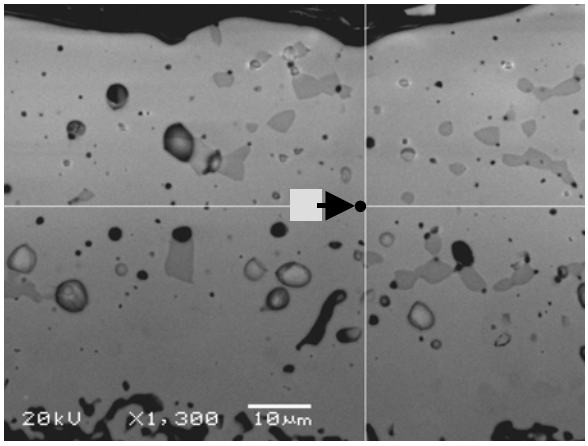

Figure 1-26. Microstructure of LSGM films after 1500^{o}C/4 hours

1.2.1.3.4 CHEMISTRY OF AS-SPRAYED LSGM

The chemistry of LSGM powder sprayed with various parameters, types of gun-anode and LSGM feedstock is summarized in Table 1-3. In general, the Ga-loss indicated by a higher A/B value increases with gun power and Ar flow for a given powder feedstock and the type of anode. Higher powder feed rate and removal of cooling air are also shown to reduce the Ga-loss, possibly as a result of lower plume temperature and unfavorable kinetic condition for Ga-loss. It appears that there is no dramatic reduction in Ga-loss by new gun-anode 484 as opposed to 730-anode whereas the addition of certain amount of excess Ga_2O_3 into stoichiometric LSGM powder does adjust the as-sprayed chemistry back to stoichiometry. Based upon these data, 10 kWe, 45slpm Ar, 8g/min feed rate, 4 revolutions together with 484 gun-anode and 5 mol% Ga_2O_3 compensated LSGM feedstock has been used as a standard condition.

Table 1-3. The Chemistry of As-Sprayed LSGM with Various Spraying Parameters Measured by ICP

Power		25	15	15	7	25	7	7	25	10	25
Ar flow		65	45	45	35	65	45	45	65	45	65
Feed rate		8	8	12	8	8	8	8	8	8	8
Anode		730	730	730	730	730	730	730	730	484	484
Powder		Stoich LSGM	Stoich LSGM	Stoich LSGM	Stoich LSGM	5mol% compen. LSGM	5mol% compen. LSGM	8mol% compen. LSGM	8mol% compen. LSGM	5mol% compen. LSGM	5mol% compen. LSGM
Mol%	Feed-stock										
La_2O_3	34.78	37.31	37.67	35.38	35.35	34.12	34.19	35.68	34.02	33.72	34.74
Ga_2O_3	33.06	28.94	27.99	32.92	32.13	34.42	33.92	31.01	34.77	33.20	32.05
SrO	16.56	17.31	17.38	17.26	17.22	16.97	16.92	17.40	16.67	16.16	16.39
MgO	15.39	14.98	16.13	16.63	16.54	16.96	16.87	17.37	17.12	16.79	16.66
A/B	**1.06**	**1.26**	**1.29**	**1.07**	**1.09**	**0.99**	**1.01**	**1.12**	**0.98**	**1.00**	**1.06**

1.2.1.3.5 X-RAY DIFFRACTION PATTERNS OF AS-SPRAYED LSGM AND AMOSPHOUS PHASE DETERMINATION

A typical XRD pattern of as-sprayed LSGM powder is shown in Figure 1-27, along with that of feedstock. A distinctive difference is the occurrence of amorphous phase peak at 2θ ~29-30^o in the as-sprayed pattern. By using an internal standard, the amount of amorphous phase was estimated and is plotted in Figure 1-28 as a function of plasma spraying condition. The figure seems to suggest that hotter plume achieved by higher power level and primary gas flow help crystallize more LSGM than that with colder plume.

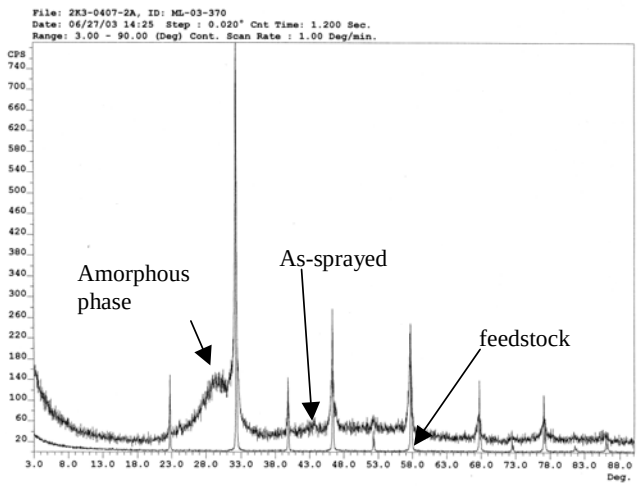

Figure 1-27. A typical XRD pattern of as-sprayed LSGM materials as a comparison with the feedstock

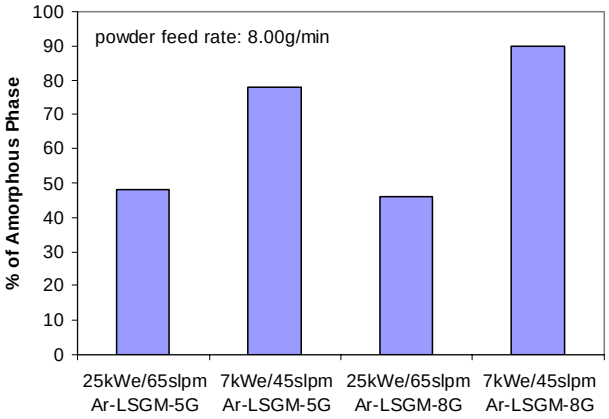

Figure 1-28. Variation of amorphous phase amount with plasma spray condition

1.2.1.3.6 DILATOMETRY OF AS-SPRAYED LSGM AND IMPLICATIONS

To study the potential volume change occurred during amorphous to crystalline phase-transition, a pellet made from as-sprayed LSGM was measured with dimensional change as a function temperature. Figure 1-29 shows the expansion curve. As evident in the figure, a shrinkage occurs at above 900^{o}C, below which a normal expansion is observed. The thermal hysteresis upon cooling indicated that the shrinkage is permanent. Recall from Figure 1-24 where a considerable crack propagation occurs at above 600^{o}C (with a holding time of 4 hours), it appears to suggest that the crack propagation is associated with volumetric contraction caused by the amorphous to crystalline phase-transition.

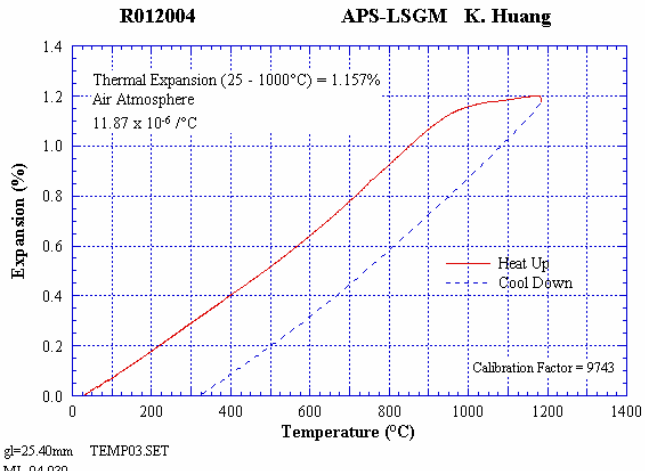

Figure 1-29. Thermal expansion curve of as-sprayed LSGM

The implication of Figure 1-29 is very important for understanding the cracking mechanism. The mechanisms for the cracks in the as-sprayed LSGM and crack propagation are apparently different. The former cracks are most likely related to the limited shrinkage of melted LSGM splats on depositing a rigid substrate, which imposes a tension on the LSGM layer, leading to the observed cracks. In contrast, as the LSGM film together with the substrate is heated, particularly above 800°C, the volume contraction resulted from amorphous to crystalline phase-transition would occur as indicated by Figure 1-29. As the substrate would not shrink at a temperature below 1400°C, the substrate would instead impose a tension upon relatively weaker LSGM film. This would further open up the pre-existing cracks. This is how the crack propagation occurs during heating up. Once the cracks exceed a certain size by which traditional solid-state diffusion could not "bridge" the cracks, further sintering would not help to heal them. One straightforward engineering solution to this problem is to heat the substrate to above the phase-transition temperature so that no amorphous to crystalline phase-transition could occur during the plasma spraying. The results of this study will be reported in the next semiannual report.

1.2.1.3.7 ELECTRICAL CONDUCTIVITY OF AS-SPRAYED LSGM FILMS

The electrical conductivity of various LSGM materials measured by AC impedance method is shown in Figure 1-30 The bar sample (sintered at 1450°C for 8 hours), used as a reference, exhibits the highest conductivity, followed by Ga_2O_3-compensated and sintered at 1500°C, Ga_2O_3-compensated and as-sprayed, and stoi-LSGM and as-sprayed. This finding is reasonable in that loss of Ga creates layered Ga-depleted phase as shown in Figure 1-23. Microstructural evolution of LSGM films as a function of temperature. The duration for each temperature was fixed at 4 hours (a) as-sprayed, (b) 200°C, (c) 400°C, (d) 600°C, (e) 800°C), (f) 1000°C and (g) 1200°C, which is a less conducting phase. As the chemical composition approaches to the ideal one and homogeneity, the conductivity increases accordingly. On the other hand. Figure 1-30 also suggests that a denser microstructure yields a higher conductivity.

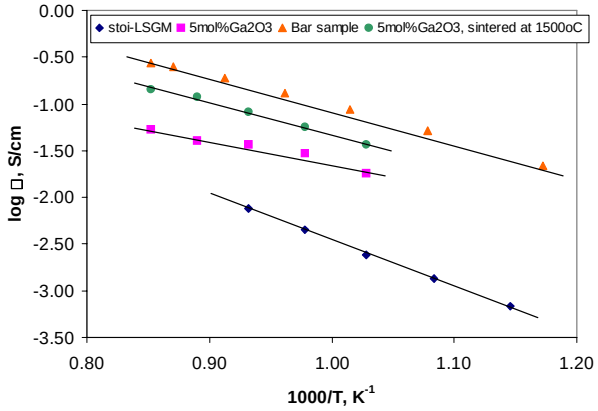

Figure 1-30. Arrhenius plot of electrical conductivity of various LSGM materials

1.2.1.3.8 SINGLE CELL TESTING RESULTS

The cell OCV as a function of time was recorded during heating up and displayed in Figure 1-31. As expected, cell OCV increased with temperature until the operating temperature was reached. At the constant operating temperature 900^{o}C, cell OCV was found to decline with time regardless of the type of fuel used. An examination of fuel outlet revealed that a certain amount of condensed water was trapped inside the tubing, which increased the pressure drop in the fuel line. The uneven pressure between air and fuel side therefore increased physical leaks through the seals, and further led to combustion and cell voltage decay. An immediate removal of water and addition of a cold-trap appeared to be effective as evidenced by a relatively stable OCV afterwards.

As the temperature was decreased to 800^{o}C, the average cell OCV was found to be lower than 900^{o}C. From a theoretical point of view, this suggests a possible electronic conduction present in the electrolyte layer. This assertion was also supported by an overall lower cell OCV compared to the theoretical value and marginal effect by fuel and air flow-rates.

Although the present cell configuration is not optimized and therefore not final, a small current was indeed applied to the cell to see the voltage response. Figure 1-32 shows the measured V-J curve. The initial sharp decrease in voltage upon applying current indicates a high activation polarization resistance of the cell. It is unclear whether anode or cathode is the major contributor at present stage. However, it is known from the literature that Pt is a non-catalytically active anode for LSGM electrolyte. An Ni-SDC anode is certainly a good candidate for next LSGM ring cell testing.

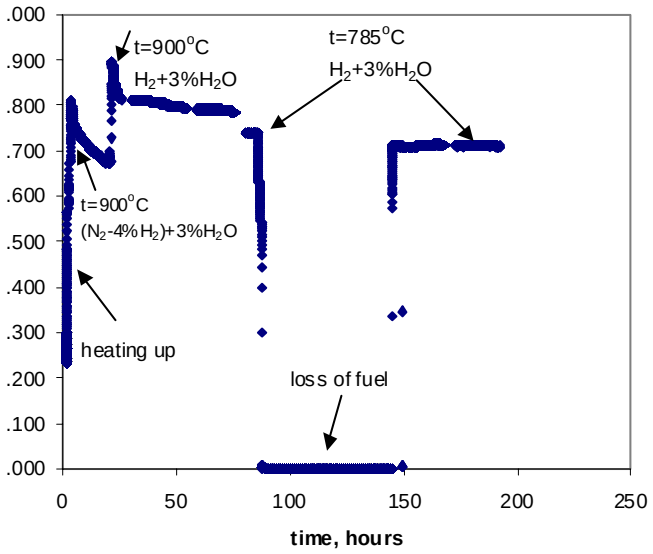

Figure 1-31. Cell OCV as a function of time

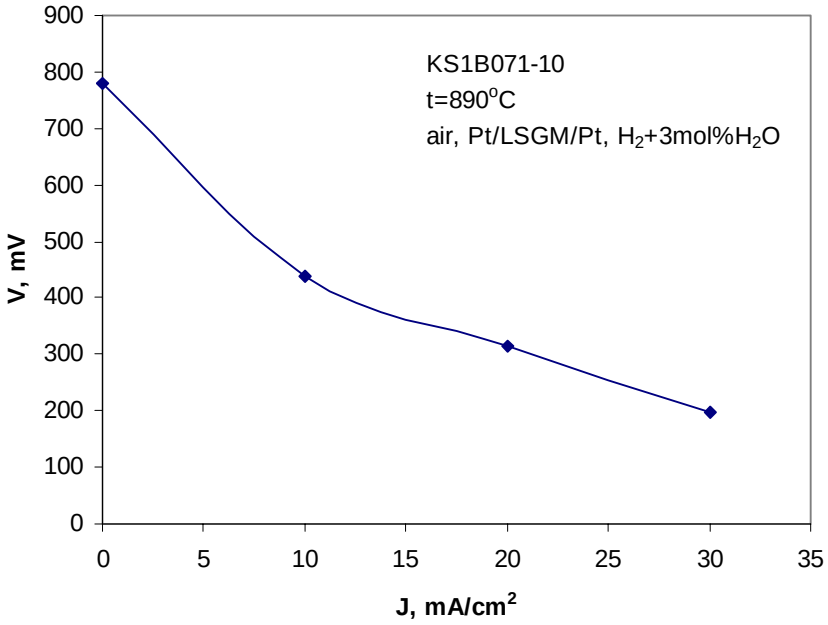

Figure 1-32. V-J curve of the tested ring-cell at 900°C

There are a total of four experimental matrices conducted during this reporting period, featuring understanding the impact provided by plasma spraying parameters, adjusted chemistry of LSGM feedstock, substrate heating and new type of gun-anode. The optimized plasma spraying condition was found to be 10 kWe gun power, 45 slpm Ar, 8g/min powder feed rate

and 4-revolution deposition layers. The average Ga-loss during plasma spraying was found to be 5 mol% Ga_2O_3, which provides a guideline for making modified chemistry of LSGM feedstock. It is clearly shown that Ga_2O_3-compensated LSGM film exhibits a higher electrical conductivity. The mildly heated substrate (<250^oC) indeed helps reduce the number of cracks in the as-sprayed LSGM layer, but the cracks are persistent in the microstructure. Further annealing of these films would lead to an unusual crack propagation. Use of new gun-anode 484 as opposed to regular 730 anode was shown to reduce the number of cracks in the films.

A single cell testing based on LSGM electrolyte was successfully performed for over 200 hours under open-circuit condition. The results indicated a certain degree of electronic conduction present in the LSGM, which is possibly caused by the high post-spray sintering temperature.

From a fundamental point of view, a better understanding of cracks formation and propagation has also been achieved. It is understood so far that the cracks seen in the as-sprayed LSGM is formed due to the tension induced by a quick volume contraction of the splat during cooling on a rigid substrate. It is also understood that the crack propagation is due to the amorphous to crystalline phase-transition, which results in also a volume contraction as indicated by dilatometry measurement and further imposes a tension on the LSGM films as temperature rises. To fundamentally solve this problem, a substrate temperature above the phase-transition temperature ~800^oC during plasma spray is necessary.

LSGM single cell tests, RT-004 and RT-005, were conducted.. Both of cells tested utilized LSGM electrolyte made from heated substrate and had LSCF+LSGM cathode interlayer between cathode and electrolyte. Ni+YDC (Y_2O_3-doped CeO_2) cermet anode was used for both tests.

The details on the cell assembly are described in Figure 1-19.

The test started with flowing air inside the cell and (3%H_2+N_2)+3%H_2O) mixture outside the cell as the temperature was ramped up to 800^oC. Upon reaching 800^oC, the cover gas 3%H_2+N_2 was switched to pure H_2 saturated with 3%H_2O. To maintain a minimal pressure differential across the cell, a flow rate, approximately 400 sccm was set for fuel and 200 sccm for air, respectively. To evaluate the cell performance, AC impedance spectroscopy analysis was conducted from 0.1 Hz to 65 kHz with a DC bias. Furthermore, to examine the long-term stability the cell was loaded with a constant current while the cell voltage was monitored as a function of time.

The long-term stability of cell voltage under a constant current density of 100mA/cm^2 is shown in Figure 1-33. It is evident from the plot that the cell voltage began to decline from 0.88 volt as soon as a DC current was loaded. After operating under OCV condition for approximately three days, the cell voltage was reduced to 0.63 voltage at 100 mA/cm^2. This comparison suggests that the degradation mechanism is not necessarily related to the cell current. It may well be associated with the exposure to high temperature. In order to continue to monitor the trend of degradation, the cell was reloaded with 50 mA/cm^2 and operated for additional 80 hours. The trend of degradation persisted over entire testing period.

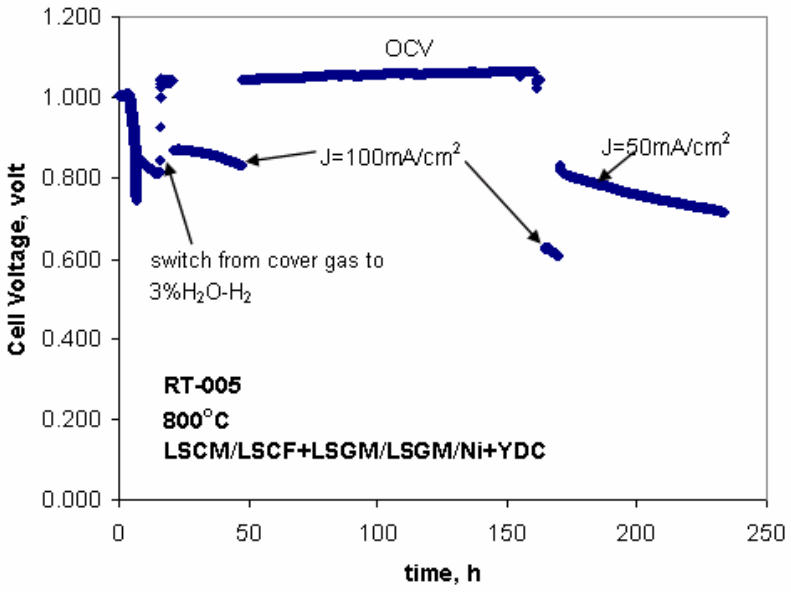

Figure 1-33. Lifetime plot of RT-005 measured at 800°C

To further elucidate the mechanism of the observed degradation, AC impedance analysis was conducted on the cell at different time, and the results are shown in Figure 1-34 and Figure 1-35. At the beginning of cell test, the impedance spectrum in Figure 1-34 indicated two semicircles, the one at high frequency related to anode process and the one at low frequency related to cathode process. It is clear that the major contribution of electrode kinetics resulted from cathode at this point of test. Upon applying DC current, the cathode semicircle increased with applied current, suggesting a limitation of gas mass transport. Based on the observation of microstructure, it is believed that the dense composite interlayer LSGM+LSCF is the root cause of the observed cathode polarization dependency on DC current. The total ohmic resistance index was found to be ~0.8 Ωcm^2 from the high frequency interception with the real-axis.

From Figure 1-35 at 20-hour, the evident difference in comparison to Figure 1-34 is the increase in total ohmic resistance index. Both anode and cathode semicircles remain unchanged in comparison to that measured at 0-hour. Previous experience seems to suggest that the conductivity stability of electrolyte LSGM and LSCM air-electrode material contributes to the elevated ohmic resistance index. At 140-hour, the anode semicircle is clearly seen to surpass the cathode semicircle as a dominating factor in addition to a continuous increase in ohmic resistance index. The growing anode polarization is believed to be due to the coarsening of Ni in an un-optimized anode NiO+YDC (Y_2O_3-doped CeO_2). A plasma-sprayed anode Ni+YDC is expected to considerably reduce the anode polarization.

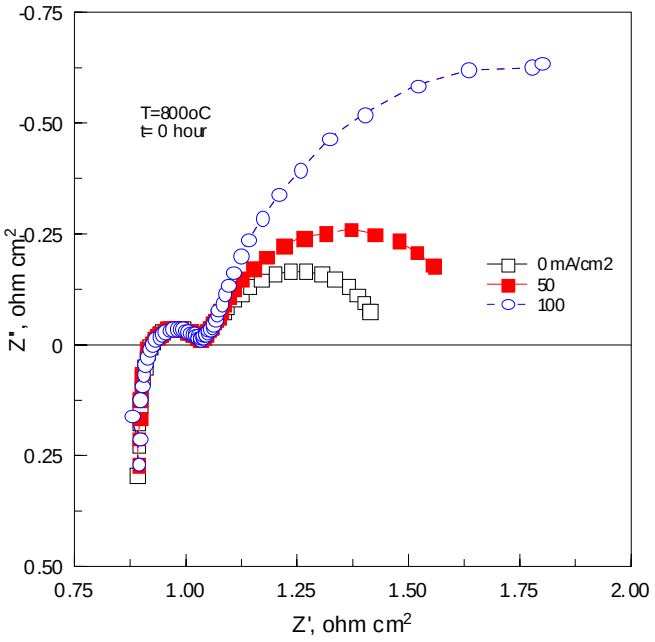

Figure 1-34. AC impedance spectra of RT-005 cell measured at 800°C

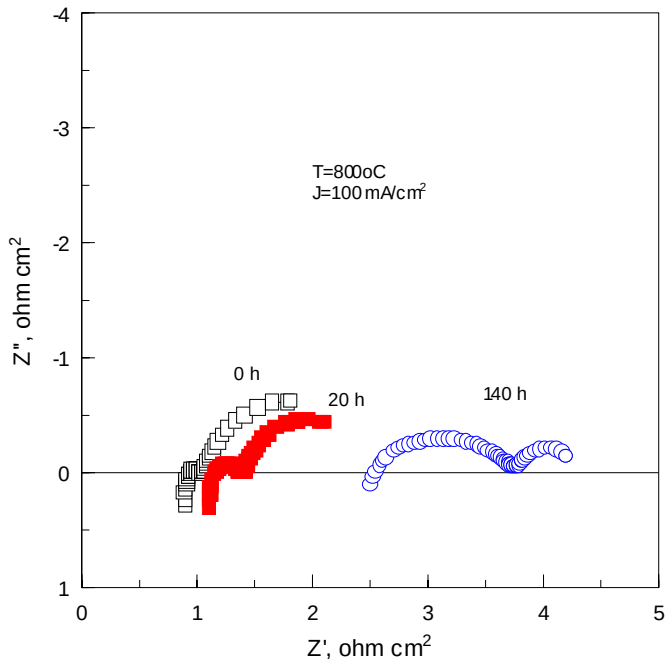

Figure 1-35. Time evolution of impedance spectra of RT-005 cell

1.2.2 CATHODE DEVELOPMENT

1.2.2.1 Introduction

Pilot-scale LSCM powder (~230 kg) has been made, from which approximate 120 tubes were extruded, calcined. About 20 of them was sintered and delivered for APS-LSGM research. The sections below describe the processing issues encountered during development, the pertinent data regarding the finished LSCM powder as well as sintered tubes, and the path forward.

1.2.2.2 Experimental

The raw materials, which included La_2CO_3, $SrCO_3$, CeO_2 and MnO_2, were assayed, weighed, mixed, calcined and milled into fine particles utilizing powder-making techniques developed at Siemens. The work involved dismantling and reassembling components of the mixing/blending equipment, feeder(s), and milling equipment along with the corresponding plumbing. After the equipment was cleaned, a single batch of LSCM material was prepared to precondition each piece of equipment and to determine the milling conditions. Several problems were encountered in the milling of the calcined material. These problems were associated with the ferromagnetic character and friability of the material. Solutions to these problems were worked out and the subsequent five batches of LSCM material (sub-lots) were milled at the appropriate parameters. The first batch of this series ~ 56 kg was used for tube-making experiments (formulation, mixing, piloting, etc). The remaining four batches (sub-lots) of material were blended and generated powder lot KS1 (230 kg) of LSCM cathode material for fabrication of cathode tubes. The tube properties results are presented and discussed below.

The chemistry of the conditioning and production material was validated using ICP analysis. X-ray diffraction was performed to examine the crystal structure. Particle size analysis was used to verify the d50 of the as milled material. SEM was used to qualitatively compare the particle size of the material as-calcined and at different milling conditions.

1.2.2.3 Results and Discussion

1.2.2.3.1 Particle Size Distribution

Particle size was measured with a Horiba laser scattering particle size distribution analyzer. Due to the ferromagnetic character and friability of the LSCM material, a new method of sample preparation had to be developed. The method involved increasing the viscosity of the solution by diluting ethylene glycol with water and adding energy during measurement to the sample in solution (increased circulation and sonnication). Thus, causing the magnetically-formed agglomerates to break apart and stay suspended in the solution. Furthermore, SEM images revealed that the intrinsic particle size showed little difference between the “as-calcined” and milled material, resulting in only a ~2um difference from the most energetic to the least energetic milling conditions. The d50 particle size range for the as-milled LSCM material was 7.5-8.5□m. Figure 1-36 shows the particle size distribution of the blended LSCM powder. Figure 1-37 displays SEM images that illustrate intrinsic particle size of the material at the aforementioned “as-calcined” and milled conditions.

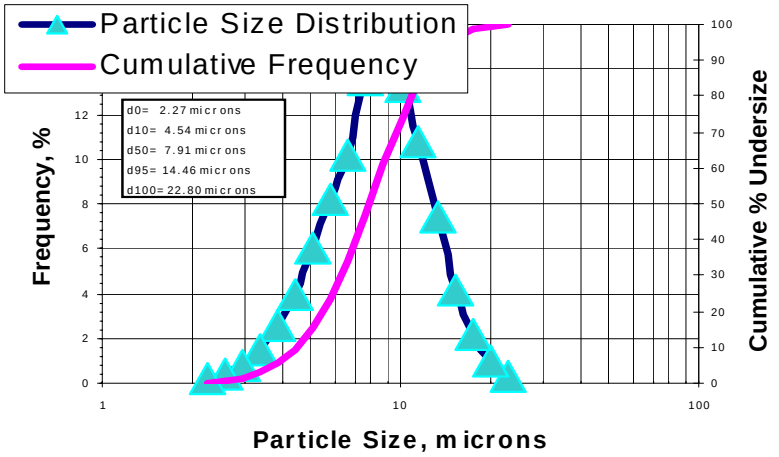

Figure 1-36. Particle size distribution of LSCM powders

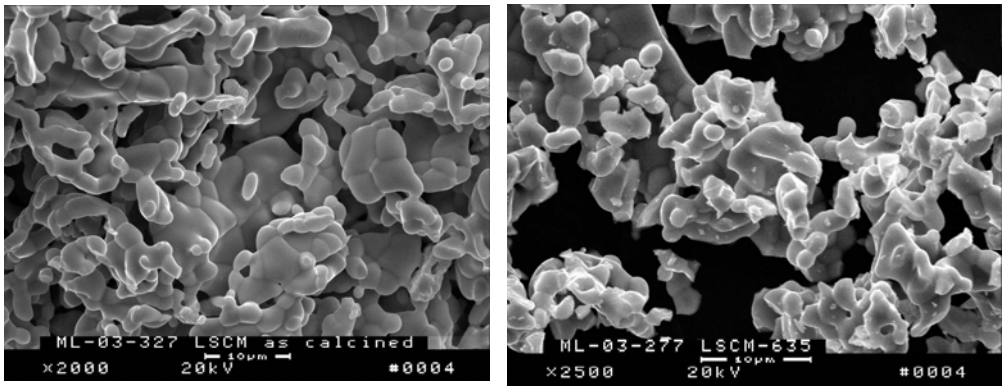

(a) as-calcined and (b) after milling.

Figure 1-37. SEM images of the intrinsic particle size of LSCM material

1.2.2.3.2 Tube Properties

The first 50 kg batch of milled powder was used to conduct mixing, extrusion and sintering experiments. The variables examined included the pore-former requirement added to the powder at blending and the amount of binder and water required for paste preparation. These variables were evaluated by tube properties and the ability to extrude the material into cathode tubes. The tube properties evaluated were diffusivity, 1400°C/2 hr shrinkage, burst strength, and elastic modulus. Varying the pore former effected the sintering time with the sintering temperature held constant. Little to zero pore former reduced the sintering time while more pore former increased the sintering time. Under both conditions the diffusivity and the 1400°C/2 hr shrinkage met specifications currently held for WPC3 cathode tubes. However, the burst strength and elastic modulus were inherently low for each condition and did not meet the strength requirements regardless of sintering time at temperature. Table 1-4 illustrates experimental data regarding the strength and elastic modulus. Most of the long tube sections were used for plasma spray experiments and elastic modulus was not measured. The low burst strength results indicated a high probability that the tube section would catastrophically fail

during the three-point bend test. The pilot powder lot KS1 piloting results are listed at the bottom of the table.

Table 1-4. Burst Strength and Elastic Modulus Data for LSCM Tubes

Tube ID	Temperature (°C)	Time (hr)	With or without pore former (%)	Burst Strength, MPa (avg)	Elastic Modulus, GPa (avg)
K1A008	1530	15	1%	21.12	N/A
K1B012			1%	18.72	N/A
K1C025	1530	10	0 %	23.75	21.4
K1D030	1530	7.5	0 %	18.51	N/A
K1E038	1530	7.5	0 %	22.65	N/A
KS1A0033	1530	7	1 %	25.83	20.40
KS1A0026	1530	7	1 %	N/A	20.93
KS1A0027	1530	10	1 %	28.4	21.14

1.2.2.4 Conclusion

The pilot powder lot of LSCM cathode material (~230 kg), designated KS1 was prepared. Approximately, 120 cathode tubes have been extruded and pre-sintered. Piloting activity has been completed and final sintering runs have commenced. An investigation into low tube strength has begun and involves lowering the calcination temperature and increasing the time. The purpose is to increase the driving force during tube sintering which may in effect result in an increased tube strength.

A new cathode composition featuring greater volume shrinkage during sintering process has been initiated recently. The basis behind this development is the necessity of co-shrinkage between LSGM film and cathode substrate in order to heal the pre-existing cracks created during plasma spraying process.

1.2.3 INTERCONNECTION DEVELOPMENT

The final composition for interconnection has been fixed based upon the studies of conductivity as a function of temperature and Po_2, thermal expansion coefficient and x-ray diffraction. A 5-kg batch powder has been made and in the process of being spray dried into agglomerates that are suitable for plasma spray.

1.3 PLASMA SPRAY TECHNOLOGY

1.3.1 ATMOSPHERIC PLASMA SPRAY (APS) OF HPD TUBES

1.3.1.1 *Introduction*

The plasma spray data generated during the manufacturing of the HPD5R1 cells for the POC has been analyzed in order to gain better insights of the APS process.

1.3.1.2 *Experimental*

A small batch of scandia stabilized zirconia (ScSZ) HPD5R1 cells (5) were fabricated to determine the initial spray parameters. Cell leak rates are in line with the yttria stabilized zirconia (YSZ) HPD5R1 cells which indicates that minimal effort would be required to switch to the ScSZ material. One cell was electrically tested, and the results will be discussed in Task 1.8.

Tubes of the HPD10R1 design were also fabricated into cells. Cell leak rates are reasonably good for a first trial, and the initials parameters are in place for successful spray events. One cell was electrically tested and the performance will be reported in Task 1.8. Several tubes of the new HPD9_G60 design were sprayed to establish the preliminary requirements to achieve leak tightness. Given the complex geometry, the plasma gun must be angled in order to always spray perpendicular to the tube. An optimal angle remains to be determined. Further trials will continue after the robotic system software is modified to accommodate the new geometry.

1.3.1.3 *Results and Discussion*

1.3.1.3.1 POC CELL PRODUCTION

During this period the HPD5R1 cell production for the SECA 5kW POC was completed. A great amount of data was collected and analyzed. Perhaps, the most important parameter during cell manufacturing is the Cell Leak Rate (CLR) measured in mmHg/min. Figure 1-38 report all the measured CLR in a box plot format and separated in Batch 1 through Batch 7. The criteria for acceptance for the next processing step is that the CLR be below 70 mmHg/min, see the dotted line.

In order to obtain a good CLR one must keep the particle temperature (T_p) to high values. In HPD cells fabrication combining the two parameters results in a large thermal input to the tube which results in the tube cracking because of thermal gradient from the front (spray side) to the back side of the tube. Tube cracking has been an issue with the HPD cells because of the current spray setup which should be upgraded using the lessons learned.

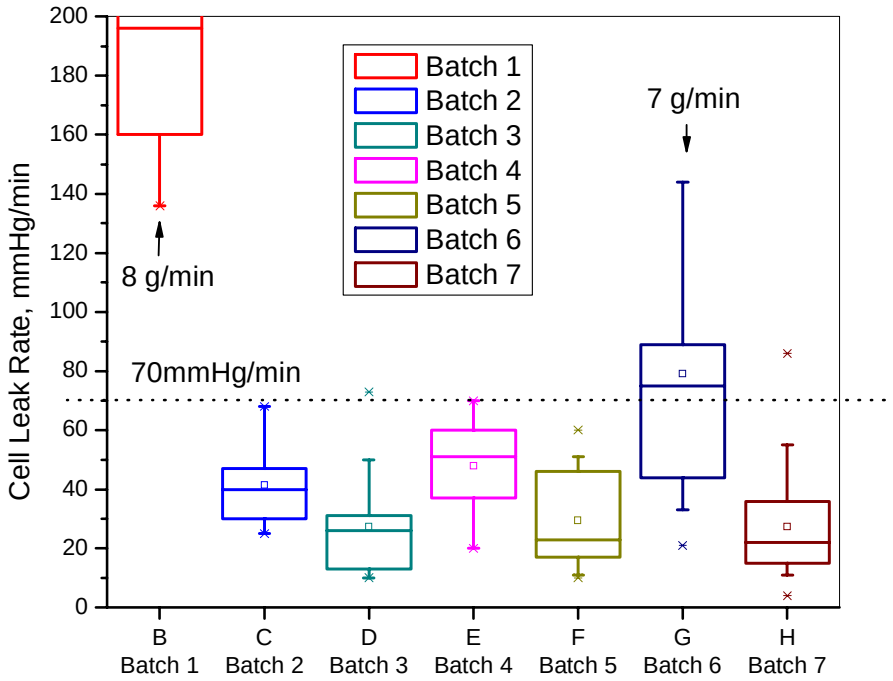

Figure 1-38. HPD5R1 cell leak rates after electrolyte densification. Powder feed rate is 6 g/min unless otherwise noted

Hence in Batch 1, see Figure 1-38, an attempt was made to lower the T_p and determine the parameters that would produce acceptable CLRs without damaging the tubes. The attempt was unsuccessful. A temporary solution was to decrease the powder feed rate so that even at high T_p the thermal input to the tube would be smaller. This was successful as one can observe from Batch 2 through Batch 5. Of course, as the powder feed rate was decreased the spraying time increased, but the yield improved significantly.

The high particle temperature required to spray the electrolyte also introduces significant wear on the gun hardware or electrodes. Basically, in order to maintain the same T_p for every spray event one must always change some of the input parameter such as power levels (kW) .

Figure 1-39 illustrates the particle temperature rise as a function of particle velocity. The lowest curve indicates the characteristic curve for YSZ particles where the literature value is found to be between 500-600J/kg K. As we can see the higher the velocity the greater the temperature rise. Basically, this temperature rise would help in melting more powder or would deform the splat further. The second curve (here provided for information only) indicates that a particle with lower heat capacity would have a faster temperature rise.

The lessons learned from the production cells have been very useful for spraying other tube designs or spraying different cell materials. For instance 5 HPD5R1 cells were fabricated using the ScSZ system in place of YSZ. The CLRs were in line with the SECA production cells when using the same set points for the particle temperature and velocity.

Tubes of the HPD10R1 and HPD9_G60 have also been sprayed into cells. However, the thinner wall in the HPD10R1 and the complex geometry of the HPD9_G60 requires lower temperature (T_p) set points in order to prevent severe thermal stresses. Of course, lower particle temperature will increase the cell leak rate but for cell testing purposes is not crucial. It is expected that as more spray trials are performed using such tubes, the cell leak rates will improve.

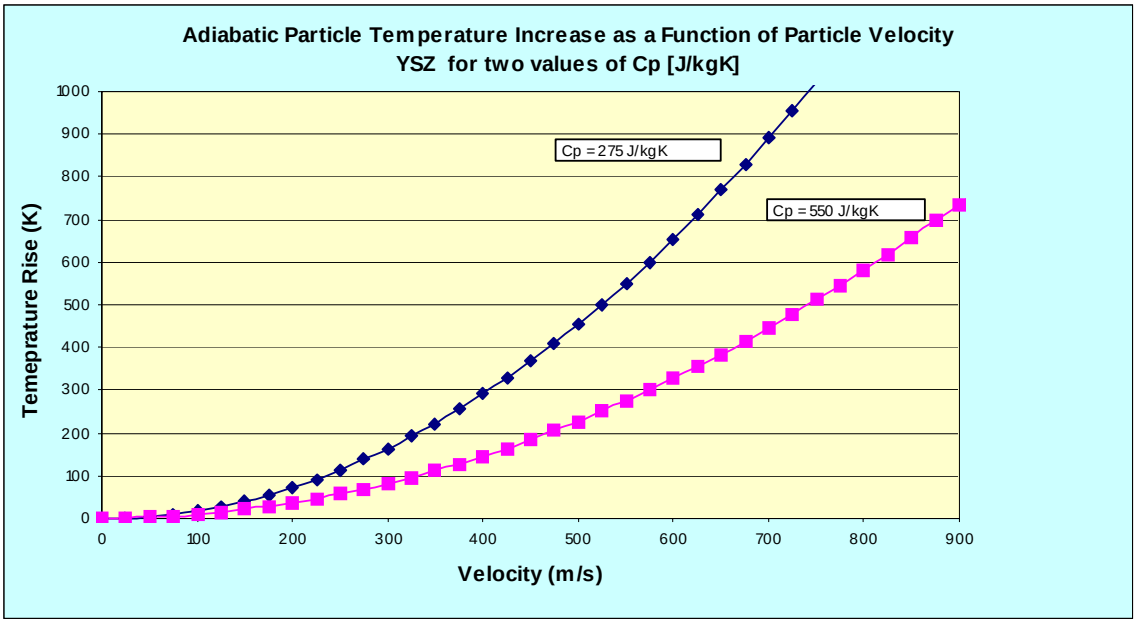

Figure 1-39. Adiabatic particle temperature rise as a function of V_P

1.3.1.3.2 PLATING NI BEFORE FE PLASMA SPRAYING

The Ni-plating is traditionally applied to IC surface after FE plasma spraying. The disadvantage of such a sequence is best reflected by the contamination from silicone adhesive of masking tape, which often causes poor plating. To solve this problem, Ni-plating is proposed to be applied to the surface of IC right after EL densification. The high-temperature process of EL densification would remove the majority of organic adhesive from masking tape used for plasma spraying EL, resulting in a clean surface for subsequent Ni-plating. As a result of this change, the quality of Ni-plating has been significantly improved and the total plating time has also been reduced from 20 minutes to 10 minutes.

The focus of this task during this reporting period was to explore a suitable spraying pattern that yields a uniform electrolyte coating on Delta cells. The work was conducted separately in two plasma spray booths, one of which is the old one with a limited gun and fixture motion and another of which is the newly built one that is able to manipulate motions with gun and sample fixture to accommodate the corrugated surfaces inherited from Delta cell design. In this section, we discuss experimental work done in these two booths. The work performed in the new booth is still ongoing.

1.3.1.3.3 OLD BOOTH

To support SECA/Coal Hybrid program, a total of twenty Delta 9 cells were manufactured in the old booth. The plasma spraying process was applied to make interconnection, electrolyte and anode. The major challenge was the electrolyte coating, which were reflected by a much higher plume temperature and two additional manipulations on gun angle. At the beginning, Delta 9 cells could not survive the impact of the hot plume that was used for regular HPD cells, due to the generally higher stress level inherited by Delta 9 cell and a limited cooling capacity by the in-house air. To circumvent this problem, the average plume temperature had to be reduced. As a result, the yield of electrolyte production was improved. However, the subsequent densification process had to be extended to achieve an acceptable leak rate requirement.

1.3.1.3.4 NEW BOOTH

To improve the coverage and uniformity of the coated electrolyte layer on Delta cells, a new plasma spraying booth was recently built. The new booth features flexibility of turning the cell at any desirable angle and increased cooling capacity. With these two major modifications, the uniformity and the coverage of the electrolyte across the Delta 9 cells are expected to be significantly improved while high plume characteristics can still be applied to the process due to an increase cooling capacity. Currently, a number of matrices have been designed to tune the plasma spraying parameters for achieving the optimal thickness and the density of the electrolyte. More results will be available for next reporting period.

1.3.1.4 *Conclusion*

In conclusion, the cell manufacturing for the SECA 5kW POC has been completed. The data accumulated has been analyzed in order to gain better insights of the APS process for HPD cells. All the lessons learned have been incorporated and are being used to fabricate other types of cells such as new cell geometries or for new cell materials.

Several cells were made using the ScSZ composition for the interlayer, electrolyte, and fuel electrode. Initial results indicate that minimal effort would be required to switch to the ScSZ material. A few tubes of the HPD10R1 design were also fabricated into cells. In addition, the newest tube design (HPD9_G60) has been sprayed to establish the preliminary requirements for achieving good leak rates. Given the complex geometry, the plasma spray gun must be angled in order to always spray perpendicular to the tube surface. The angle has been introduced manually, but a modification in the system software would facilitate the spraying of the new geometry.

1.4 CELL-TO-CELL CONNECTION

1.4.1 INTRODUCTION

1.4.2 EXPERIMENTAL

A five HPD5R1 cell bundle with the Ni foam cell-to-cell connector technology has been assembled and sintered. This bundle will be electrically tested to prove out the Ni foam technology as a replacement of the current Ni felt technology used in the POC. It is believed that the Ni foam is much cheaper that the counterpart Ni felt technology. Currently, the test article is being assembled. The results of the electrical test will be reported in the next reporting period.

Two additional cells have been fabricated which requires a different bundling design in the event bundles are assembled for some testing either electrical or mechanical. At this time the bundling design here presented are only concepts and may change with time. Figure 1-40 illustrates the current cell technology at Siemens Westinghouse. The standard cylindrical cell has a well established history. The HPD5R1 cell has exceeded 15,000 testing hours (cumulative) and will be tested on a 5kW environment. One of the HPD10R1 cell has been tested and has shown better performance that the HPD5R1 cell. The latest addition or the HPD9_G60 cell has been fabricated and will be tested shortly. This cell type has the interconnection on the flat portion of the tube while the fuel electrode is applied over the triangles region. The triangular shape allows for increased surface area and therefore higher power (Watts) per cell.

Cylindrical	HPD5R1	HPD10R1	HPD9_G60

Figure 1-40. The types of tubes and cells currently available at Siemens Westinghouse

In terms of bundling technology, the cylindrical cell bundle uses an established cell-to-cell connector (a combination of Ni screen and Ni foam). The HPD5R1 makes uses of a Ni felt cell-to-cell connector which has shown superb results in a multi-cell test and awaits data from the POC unit. A Ni foam cell-to-cell connector is being investigated as a potential replacement for Ni felts.

Figure 1-41 shows pictures of current bundles of the cylindrical and HPD5R1 type.

Figure 1-41. Different types and sizes of bundles currently fabricated at Siemens Westinghouse

The unit volume cross section of the three different HPD bundles is shown in Figure 1-42. The top drawing shows what is currently done with the HPD5R1 cell with either a Ni felt or Ni foam cell-to-cell connector. It envisioned that the HPD10R1 bundle (middle drawing) will require the same type of cell-to-cell connector made either with Ni felt or Ni foam. The only difference is that additional ridges would be required in order to maintain a uniform current density distribution and fuel channels. However, the HPD9_G60 bundle (bottom drawing) shows a significant advantage in bundling technology as a single thin pad of Ni foam would be required. Thin rolls of Ni foam of 1-3 mm are commercially available as they are used extensively in the battery industry and are therefore cost effective. A thin pad of Ni foam is sufficient because the fuel channels are already built in the cell, and the current distributes evenly along the sides of the triangles. Hence, a significant improvement in terms of power per volume can be expected with this type of cell. Figure 1-43 illustrates a five HPD5R1 cell from which height one may fit 7-8 HPD9_G60 cells. The HPD5R1 bundle in Figure 1-43 was used in Test 986 and was able to produce about 1 kW of power. Using a theoretical value for the HPD9_G60, one could expect to produce more than 3kW of power from the same volume.

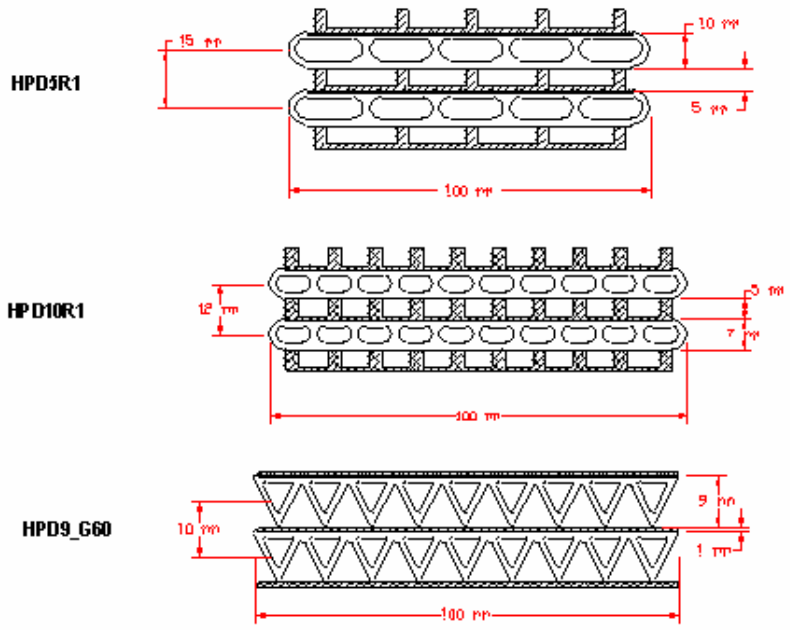

Figure 1-42. Current bundle technology for the HPD5R1 cell, and expected bundle technology for the HPD10R1 and HPD9_G60 cells

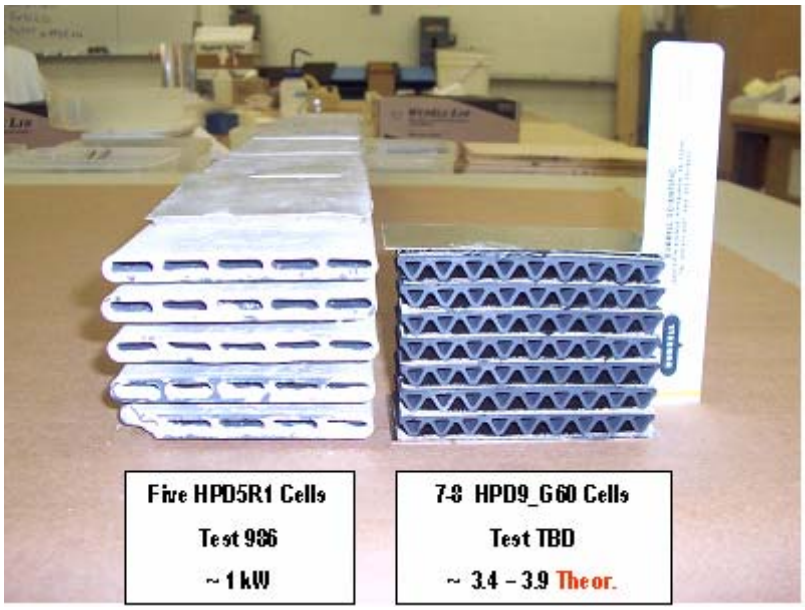

Figure 1-43. Comparison of number of cells that can be fitted in the same bundle height for the HPD5R1 and HPD9_G60 cell types

1.5 ON CELL REFORMATION

1.5.1 INTRODUCTION

On cell reformation program at the beginning focused on setting up testing protocol and testing single cells with reformation-retarding coatings.

1.5.2 EXPERIMENTAL

The first single cell test aiming to evaluate the effectiveness of reformation-retarding coatings was carried out. The cell used in this test has a ScSZ electrolyte and standard Ni/YSZ anode. The bottom half of the 50-cm cell was coated with alumina-magnesium oxide spinel (with excess MgO) in order to slow down methane reformation rate on anode. At the same time peripheral components in the cell assembly exposing fresh fuel at high temperatures, such as bus bars and fuel feed, etc., were also treated with the same coating solution. 1/8 inch I.D. Inconel sampling tube was used to collect gas samples from different elevations of the cell as shown in Figure 1-44. The cell sits in an alumina fuel feed chamber, and incoming fuel directly hits the closed end of the cell. Fuel feed tube was initially installed close to the edge of fuel feed chamber, and can be only pulled up to higher elevations due to the softness of the metal tube at high temperatures. An alumina tube was on order for future tests. Leak tests were performed before gas samples were collected in order to ensure a gas-tight system obtained.

1.5.3 RESULTS

Test using simulated reformate at 800^{o}C was carried out with current loading of 114mA/cm^{2} and 60% fuel utilization. Other key testing conditions were listed in Table 1-5. The sampling tube was pulled up to measure the progress of methane reformation along the cell. As shown in the table, original simulated reformate contains about 28% methane, and was quickly reformed along the cell. At only 2.5cm away from the closed end, nominally half of the methane was reformed; 13cm away saw little methane lect. Apparently methane was being reformed very fast at the closed end, and the applied coating needs to be further improved to slow down Ni/YSZ reformation kinetics. It is noted that CO_2 partial pressures decreased significantly along the cell indicating that CO_2 also involved in methane reformation. After the test at 800^{o}C, the reformation kinetics was measured at 700^{o}C under open circuit conditions. Similar results were obtained with little methane left at 13cm away from the closed end.

It seems that the reformation rate is still much faster than expected at the closed end region of the cell. Future work will mainly focus on modifying the coating compositions, changing anode materials and microstructures to slow down the reformation kinetics. In addition, cell testing assembly will be modified so that the deep fuel feed pocket where the cell sits in is eliminated and incoming fuel does not directly impact on the closed end forcing on cell reformation.

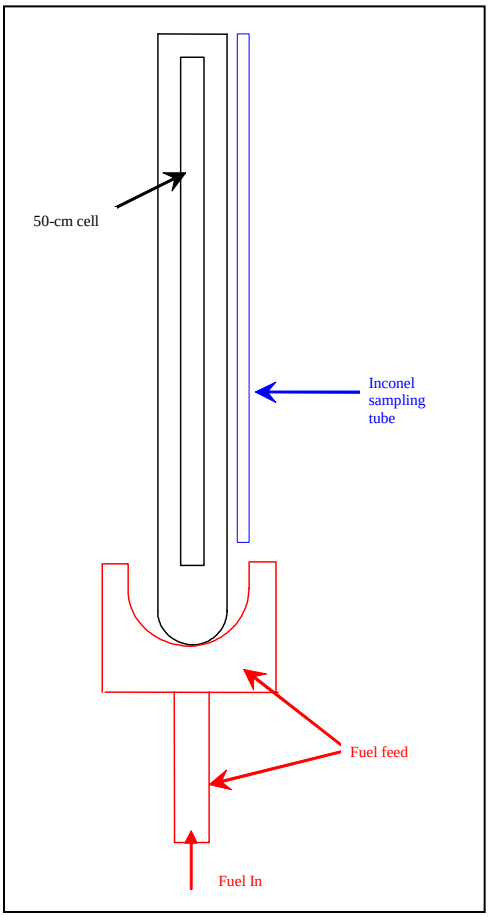

Figure 1-44. A schematic showing the cell, fuel feed, and Inconel sampling tube system

Table 1-5. Measurement of Methane Reformation Along the Length of the Cell

Testing conditions: 800^{O}C, $MgAl_2O_4$ spinel with MgO excess coating (one half of the cell from bottom coated), 22% humidity, 114mA/cm^2, Voltage 650-660mV, Sampling tube: Inconel, fuel Utilization: 60%, Air flow 8SLPM

	CH_4	H_2	CO	CO_2	H_2O
Simulated reformate composition	28.3	26.8	17.8	35.3	Not Analyzed
P-tip of the cell=2.5cm	13.5	42.6	18.7	25.2	Not Analyzed
P-tip of the cell=8cm	10.2	45.5	19.9	22.1	Not Analyzed
P-tip of the cell=13cm	2.8	49.2	26.3	16.3	Not Analyzed

1.6 LOW TEMPERATURE YSZ FUEL CELL DEVELOPMENT

1.6.1 ADVANCED CATHODE INTERLAYER

1.6.1.1 *Introduction*

Development of advanced cathode interlayer was carried out. The work includes studies on the effects of replacing electronic conducting phase WPC3 with LSF ($La_{0.80}Sr_{0.20}FeO_3$) and ionic conducting phase YSZ or ScSZ with GDC (20mol%Gd-CeO_2) on the cathode resistance index. In addition, an alternative technique of applying interlayer was also tried.

1.6.1.2 *Experimental*

The cathode interlayer coatings were prepared by roller-coating inks containing a mixture of either ScSZ and LSF or GDC and WPC3 on the surface of a bare cathode tube substrate.

To characterize the cathode resistance index, AC impedance analysis was conducted on a half-cell configuration. The measured resistance index includes the contributions from both cathode/electrolyte and Pt/electrolyte interfaces, where Pt is used as the counter electrode. A comparison to the baseline (ScSZ+WPC3) is necessary in order to evaluate the performance of new cathode interlayers.

Plasma spraying technique was also considered to be a method of applying interlayer coating. The advantages include one-step masking for both interlayer and electrolyte, elimination of calcination process and process continuity to plasma spraying electrolyte manufacturing. However, there are still some unknowns about this technique such as how plasma spray parameters affect the chemistry and porosity of the deposited interlayer. As a first trial, a mechanical mixture of YSZ, WPC3 and pore former was made and sprayed with moderate plasma spraying conditions. The compositions of starting materials are listed in Table 1-6.

Table 1-6. Compositions (wt%) of Starting Materials in Plasma Spray Grade Composite Interlayer Materials

	LSM	YSZ	Graphite
Mix-1	40	40	20
Mix-2	45	45	10

The chemistry and microstructures of the deposited interlayers under various plasma spraying conditions were characterized by ICP and optical microscopy, respectively.

1.6.1.3 *Results and Discussion*

1.6.1.3.1 NEW COMPOSITE LAYER

The cathode polarization resistance indices of two new interlayer cells measured by AC impedance analysis at 900^{o}C are summarized in Table 1-7 along with baseline cell S2C0048.

R_{ct}, R_{pore} and R_{pol} represent cathode-associated charge-transfer resistance index, pore diffusion resistance index and polarization resistance index (the sum of R_{ct} and R_{pore}), respectively. Comparing with the baseline data, it is evident that both LSF+ScSZ and GDC+WPC3 interlayer cells have a higher R_{ct} than baseline cell. However, GDC+WPC3 clearly shows the lowest R_{pore} whereas ScSZ+LSF shows the highest R_{pore}. As a result, GDC+WPC3 exhibits the lowest R_{pol} among the three interlayers. The microstructural observations as shown in Figure 1-45, also confirmed this finding by showing more porous microstructure in the GDC+WPC3 interlayer and a denser microstructure in the ScSZ+LSF interlayer. Considering that fact that all three interlayer cells were sintered at the same condition, it also suggests that GDC material be more refractory to WPC3 than ScSZ and LSF material be sinterable than WPC3.

Table 1-7. Comparison of Cathode Polarization Resistance Index of New Interlayer at 900°C

Cell ID	IL type	R_{ct}, Ωcm^2	R_{pore}, Ωcm^2	R_{pol}, Ωcm^2
S3A0008	LSF+ScSZ	0.597	0.523	1.120
S1C0252	GDC+WPC3	0.339	0.128	0.467
S2C0048	WPC3+ScSZ	0.289	0.430	0.719

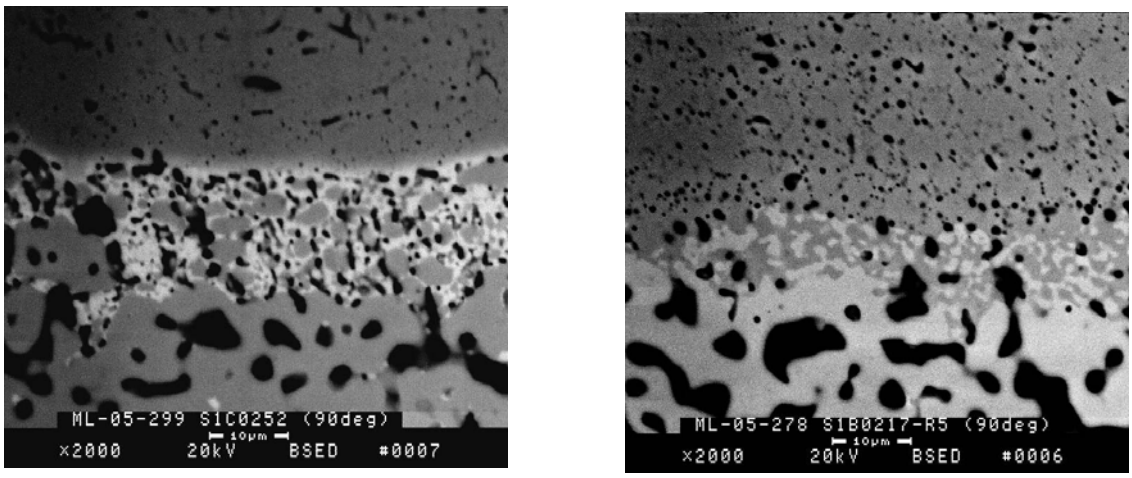

Figure 1-45. Back-scattered SEM microstructures of GDC+WPC3 and LSF+ScSZ interlayers

1.6.1.3.2 PLASMA SPRAYING COMPOSITE LAYER

The chemistry of deposited interlayer could well be altered due to the exposure to high temperature plume. In order to monitor the chemistry change after plasma spraying, the powders sprayed under different plasma spray conditions were collected and analyzed by ICP. The results are shown in Figure 1-46. For a given gun power and primary gas Ar usage the YSZ content increases with H_2 usage whereas LSM content decreases with H_2 usage. The increase of YSZ with H_2 usage is understood to be due to a hotter plume induced by the use of H_2, which in turn improves the deposition efficiency of high melting-point YSZ powder whereas

the decrease of LSM with H_2 usage is also due to a hotter plume that leads to more evaporation of Mn. This assertion is supported by the fact that the stoichiometry of Mn in LSM was found to decrease with increasing H_2 usage, *i. e.*, 0.91, 0.88 and 0.82 for H_2=0, 0.5 and 1.0 slpm, respectively. To achieve stoichiometric Mn in LSM, a certain Mn compensation in the starting materials is necessary. For YSZ:LSM ratio of 50:50 by weight, Figure 1-46 suggests the optimal H_2 usage to be around 0.8-0.9 slpm for gun power of 15 kWe and Ar 45 slpm.

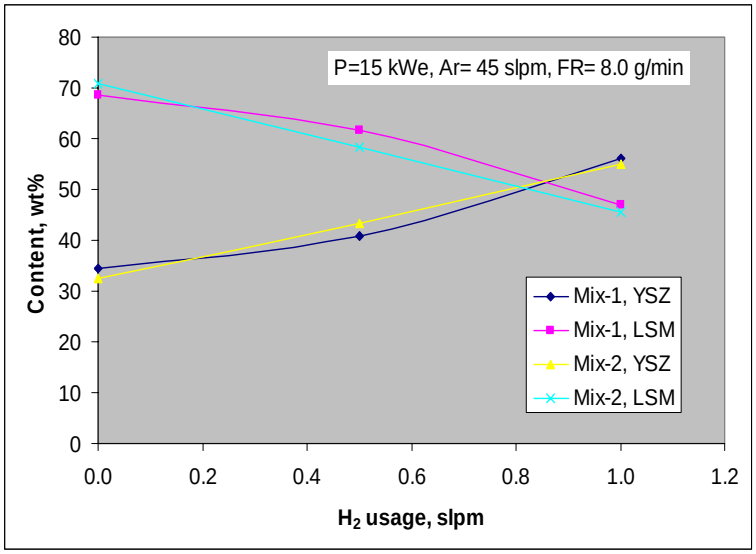

Figure 1-46. YSZ and LSM contents as a function of H_2 usage in plasma spraying

A typical microstructure of plasma sprayed interlayer is shown in Figure 1-47, where the thickness of the layer is estimated to be ~15 micron, but with apparently limited porosity and residual graphite. This observation suggests that the majority of graphite is consumed in the plume. To improve the deposition efficiency of graphite, the homogeneity of three phases is highly demanded. Spray drying the three phase mixture into agglomerates, by which plasma spray gun is fed, is a better way to achieve the homogeneity. More results will be reported in the next period.

Surface roughness, Ra, of plasma sprayed interlayer was also found to be high, in the range of 200-250 micron inches. High Ra could induce cracks in the electrolyte during densification process. The root cause of high Ra is believed to be the large particle size of starting materials used for plasma spraying. With agglomerating fine particles of starting powders, Ra is expected to be significantly reduced.

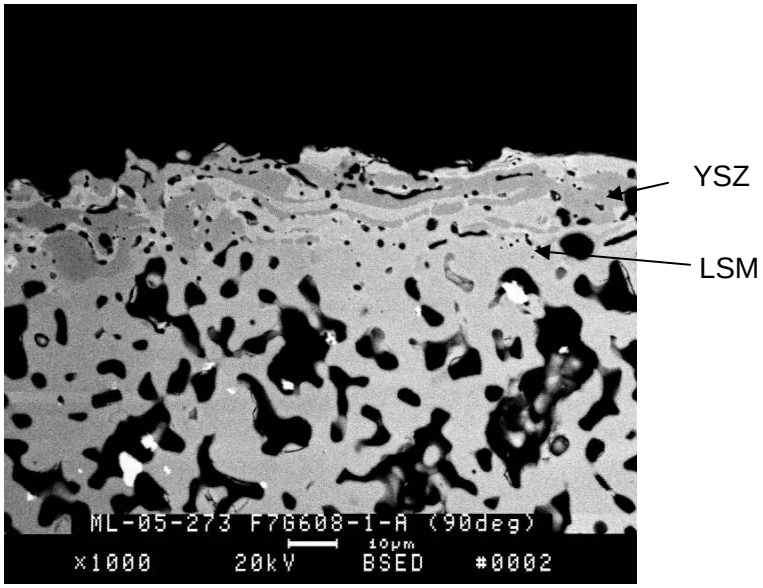

Figure 1-47. Back-scattered SEM microstructure of plasma sprayed interlayer. Gun power 15 kWe, Ar 45 slpm, H_2 0.5 slpm and powder feed rate 8.0 g/min. The interlayer/cathode couple was sintered at 1345^{o}C for 6 hours

1.6.1.4 *Summary*

The GDC+WPC3 interlayer has been identified by AC impedance analysis as a promising candidate for further improving power density of tubular SOFCs at lower temperatures. On the other hand, in an effort to simplifying manufacturing process plasma spraying composite interlayer was also practiced.

1.6.2 LOW TEMPERATURE CATHODE FOR YSZ BASE CELLS

1.6.2.1 *Introduction*

During this reporting period, ScSZ cell development was concentrated on testing effects of a variety of material combinations such as interconnection and anode interlayer on cell performance. This study was initiated based on the observations that the ohmic voltage drop across the interconnection and anode polarization become increasingly significant as the temperature decreases. With the cathode polarization being considerably reduced by implementing cathode interlayer, the contributions from interconnection and anode should also be mitigated, particularly at lower temperatures.

1.6.2.2 *Experimental*

The anode interlayer used in this study is a mixture of 20mol%Sm_2O_3-doped CeO_2 and Ni. It was deposited first on the surface of the electrolyte with a thickness of ~25 microns, followed by spraying a 75-micron regular ScSZ+Ni cermet.

High A/B interconnection materials were used in this study. Theoretically speaking, higher A/B ratio in a Perovskite material would reduce the resistivity of the interconnection. Chemical homogeneity of sprayed interconnection, on the other hand, also contributes the resistance index of the interconnection.

1.6.2.3 *Results and Discussion*

1.6.2.3.1 ScSZ-Based Cell Testing

Figure 1-48 shows a lifetime plot of cell testing 1068, which is made of ScSZ+WPC3 cathode interlayer, ScSZ electrolyte and SDC+NI anode interlayer/ScSZ+Ni anode. After the cell was conditioned and a number of electrochemical characterizations were completed, it is operated at 900°C with a current of 70 A and fuel utilization of 83%. The cell voltage stabilizes at 675 mV with no sign of degradation after a total of testing hour of ~950 hours. It is planned to run this cell at 900°C for at least 5000 hours to see the actual degradation rate.

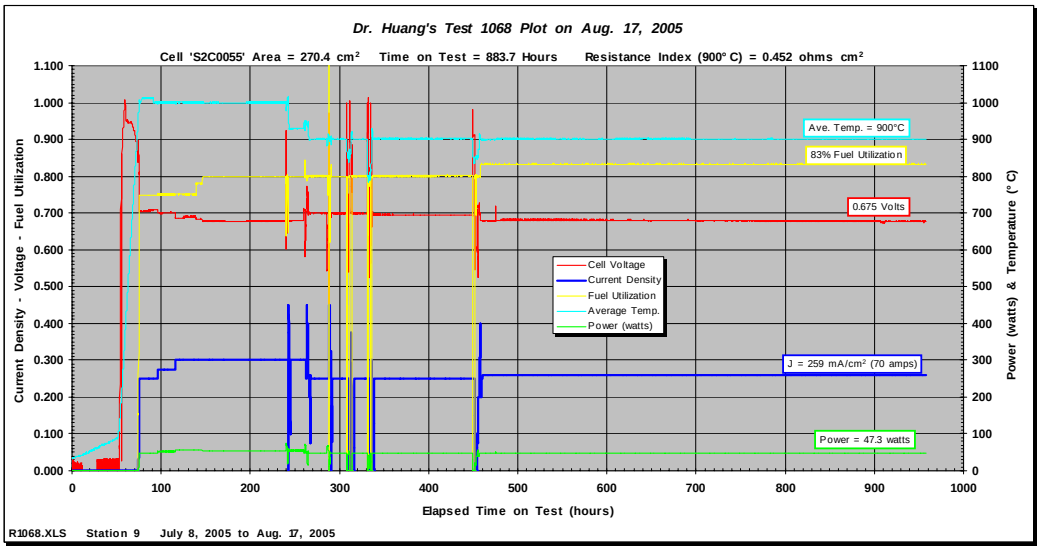

Figure 1-48. The lifetime plot of Test 1068

The electrochemical performance of Test 1068 is illustrated in Figure 1-49, where V-J characteristics are shown at different temperatures. The measured total ohmic resistance indices at 1000, 940 and 900°C are 0.345, 0.360 and 0.399 Ωcm^2, respectively, representing a considerable reduction in comparison to all YSZ cells tested in the past. Another obvious reduction is the pore diffusion polarization as indicated by a much smaller O_2-shift value of 52 mV at 1000°C, which suggests approximate 10 mV voltage loss at 300 mA/cm^2 by the pore diffusion polarization after Nernst potential is corrected. Another important finding from the plot is that there is almost no difference in performance from 900 to 1000°C, implying a potentially better performance in a practical generator where a substantial temperature gradient is present along the length of cells. According to Figure 1-49, the current density at cell voltage of 0.65 volt and 900°C is ~330 mA/cm^2, a 50% power enhancement over today's production cells.

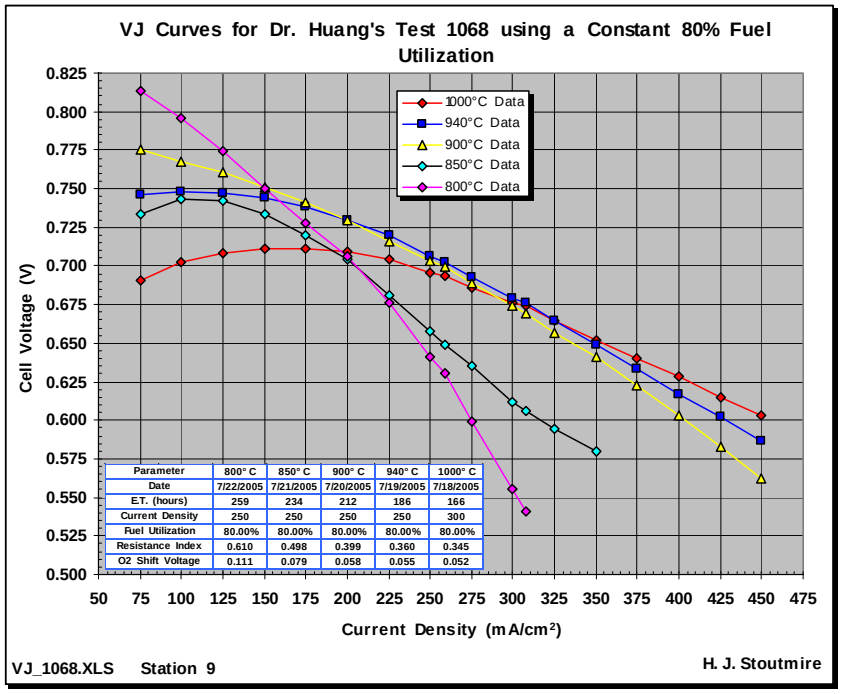

Figure 1-49. The V-J characteristics of Test 1068 at different temperatures

Another contributing factor for low ohmic resistance index is the low resistivity of interconnection used in T1068, which has been confirmed by an independent ring cell testing. The reason for this low resistance index is revealed by electron microscopic analysis. Figure 1-50 shows elemental mappings of Cr in the interconnection of T1068 and another "bad" lot interconnection measured by EDX. The Cr distribution is evidently much uniform in the cell of T1068 than in "bad" lot interconnection. Furthermore, the EBMA indicates a higher A/B ratio (~1.00) of this interconnection compared to the "bad" lot (~0.85).

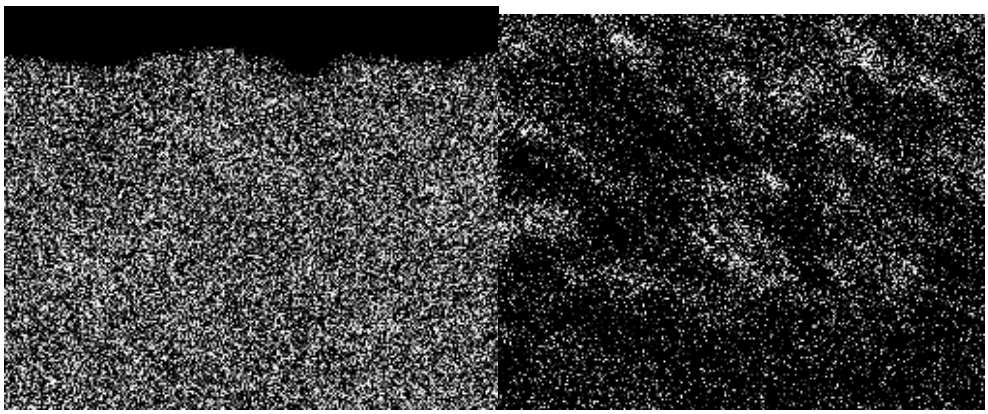

(a) **(b)**

Figure 1-50. Comparison of Cr-distribution of a "good" and "bad" interconnection lots (a) "good" IC lot (b) "bad" IC lot

1.6.2.4 *Summary*

The V-J characteristics of ScSZ-based cells revealed almost the same performance at 900 as at 1000°C, benefiting from using ScSZ+WPC3 cathode interlayer, ScSZ electrolyte and SDC+Ni anode interlayer. The performance at 900°C of ScSZ cell represents a 50% power enhancement over present production cells. It was also found that a higher A/B ratio and more homogenized compositions in interconnection result in low resistivity.

1.6.3 DEVELOPMENT OF ALTERNATIVE AIR ELECTRODE MATERIALS

1.6.3.1 *Introduction*

Efforts continued to develop alternative air electrode materials focusing on Y-series compositions. These materials, compared with traditional WPC3 composition, have higher calcium doping resulting in higher conductivity and lower costs. Y1 composition testing results showed that a reaction layer developed between air electrode and interconnector when the cell was under load. As a result, Y2 and Y4 compositions with lower calcium doping were prepared and tested.

1.6.3.2 *Experimental*

1.6.3.2.1 Y2 Air Electrode Development

1.6.3.2.1.1 Performance and Stability for the Y2 Tubes

In order to evaluate Y2 air electrode, a Y2 tubular cell (Y2D048) was made with the following key components: Y2 air electrode, CeO_2 interlayer, YSZ electrolyte, and Ni/YSZ fuel electrode. YSZ electrolyte was sintered at 1345°C for 17 hours. Figure 1-51 shows performance of the cell including a starting break-in period for the first 200 hours, stability test of measuring cell voltage at a constant current density, performance measurements at different current densities, and finally five thermal cycles between 200 and 1000°C. As shown, after the break-in period, cell voltage is stable at current density of 300mA/cm^2, which indicates that, unlike Y1 cell, the interface between IC and AE of the Y2 cell is stable. This is also confirmed by the microstructure analysis of the interface showing no reaction layer formed after testing. Besides, the cell shows no performance drop before and after the five heat cycles suggesting the Y2 AE composition is also stable with insignificant amount of CeO_2 phase separation, if any.

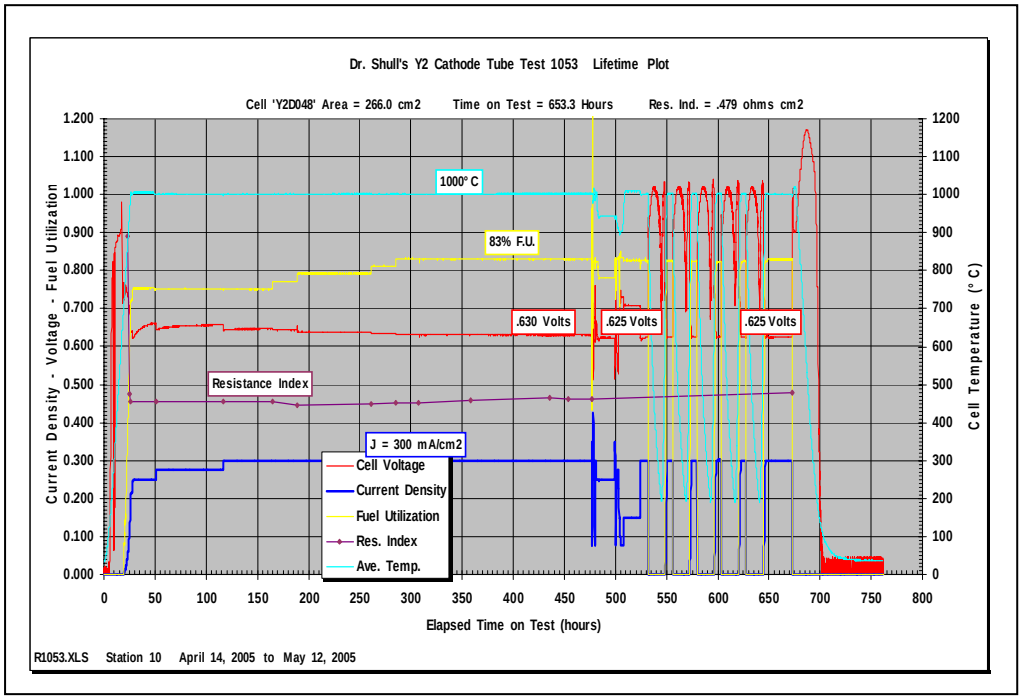

Figure 1-51. Electrochemical testing of the cell Y2D048 with Y2 air electrode

Performance measurement of the Y2 cell up to 400mA/cm^2 is plotted in Figure 1-52 comparing with that of a WPC3 cell. Y2 shows a slight lower performance than WPC3 in the entire current density range. It seems that the low-resistance Y2 AE does not translate to a better cell performance. The reason for the low performance is that the IC has high resistance, and it turned out later that the IC powder lot was not qualified for production, which results in high total cell resistance index of 0.479Ωcm^2 and low cell performance. Y2 cells with the right components will be made in the future. In the meantime, composite interlayers containing Y2 AE material and Sc doped zirconia are also being studied to enhance cell performance.

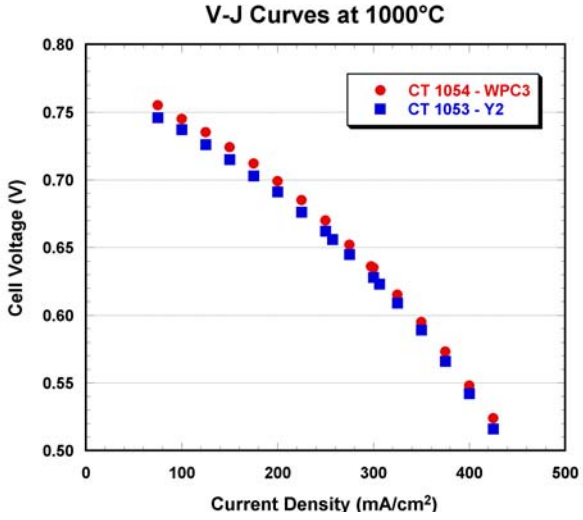

Figure 1-52. Comparison of V-J curves of WPC3 and Y2 cell with similar cell configurations

1.6.3.2.1.2 Stability of the Y4A

Again, past experience of testing Y1 cells showed that the interface between AE and IC degrades over time under current loading conditions while the interface is free of reactions even soaking at high temperatures for an extended period of time without currents. It seems that the undesired reactions are a process related to or driven by electrical fields. Therefore, the stability of Y4 AE with IC was investigated with a half cell under load of 300mA/cm^2 at 900^{o}C to simulate fuel cell operation. As shown in Figure 1-53, a half cell section of Y4 AE coated with IC and electrolyte was tested in a dual atmosphere with air as oxidant and 5%H_2 as fuel. A constant current density of 300mA/cm^2 flowed through the interface of AE and IC for 500hrs using potentiostat. As shown in Figure 1-54, the cell voltage is relatively stable during the 500 hour test suggesting that minimal undesired reactions occurred at the interface.

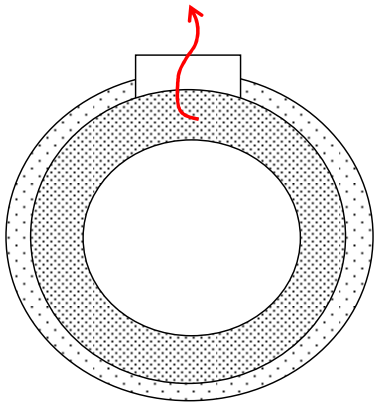

Figure 1-53. A Y4 half cell section of Y4 air electrode coated with IC and electrolyte. Current flows through AE and IC as the arrow indicates in a dual atmosphere to simulate fuel cell operation

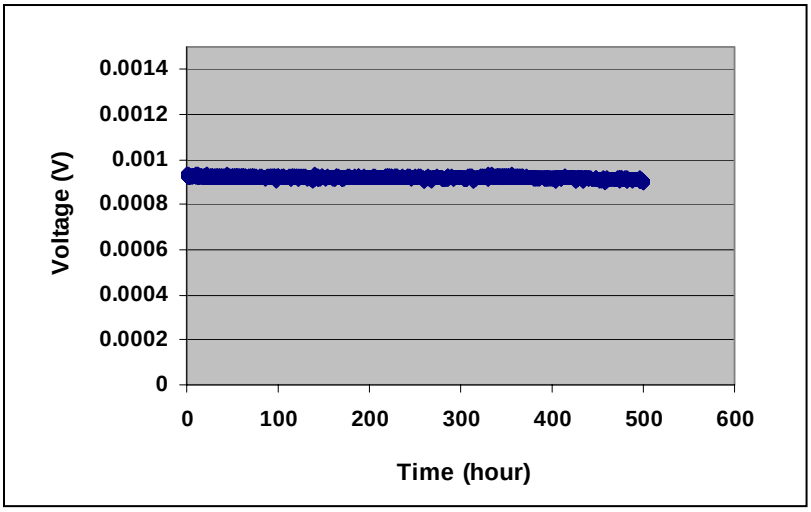

Figure 1-54. Stability test of the interface between IC and AE of a Y4 half cell section as shown in Figure 1-53.

No major problems were encountered in the fabrication of fuel cells from the "Y4" cathode tubes. For "Y4" cells made with composite interlayer it was possible to densify the electrolyte at 1300°C compared to 1345°C for WPC3 cells. Attempts to fabricate "Y4" cells using vacuum infiltrated ceria rather than composite interlayer were generally not successful. The resulting cells usually exhibited high ohmic resistance.

Electrical conductivity versus temperature is plotted for Y4 and the standard WPC3 cathode material in Figure 1-55. The Y4 composition exhibits a 33% higher conductivity than WPC3 at 1000°C, and the improvement is even greater at 800°C and 900°C. More importantly, though, is the stability of the conductivity over time at operating temperature. WPC3 is known to undergo increases in resistance due to phase equilibrium reactions at cell operating temperatures. At 1000°C this effect is of little consequence. However, it becomes more and more significant at lower temperatures. Conductivity versus time at 900°C is plotted for both Y4 and WPC3 in Figure 1-56. WPC3 eventually stabilizes at ~30 S/cm after a few thousand hours, but little or no degradation is observed for Y4, giving it roughly three times the conductivity for a mature cell at 900°C.

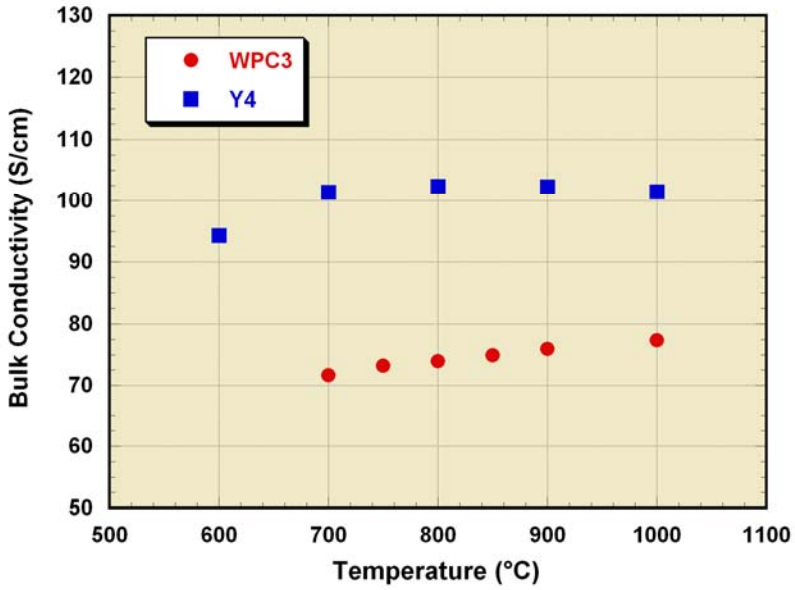

Figure 1-55. Bulk electrical conductivity versus temperature for WPC3 and Y4 cathode tubes

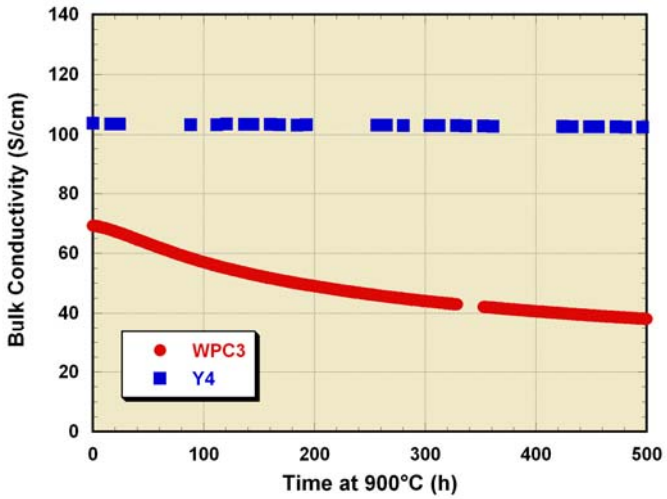

Figure 1-56. Bulk electrical conductivity versus time at 900°C for WPC3 and Y4 cathode tubes

1.6.3.2.1.3 Performance of Y4 Cell

A Y4 cell (Y4B012) with the following configuration Y4 AE, ScSZ EL, Ni/YSZ FE, and Y4/ScSZ IL was made with electrolyte sintered at 1345^{o}C for 6hrs. Figure 1-57 and Figure 1-58 showed the performance of Y4 under a standard test plan and V-J curves at different temperatures, respectively. The cell voltage is relatively stable indicating there is no degradation at the interface between IC and AE, as already confirmed in the previous stability test. However, the cell performance is still lower than that of WPC3 by about 10mV at 1000^{o}C, for example. Though the cell has a low ohmic resistance index - 0.345Ωcm^{2}, impedance of a similar Y4 cell (Y4B002) shows a high cathode polarization resistance (0.608Ωcm^{2}). Low ohmic and high polarization resistances indicate that the problem arises at the interface between AE and EL. As porosity of all Y4 AE tubes were confirmed to be above 30%, the high polarization may be due to the Y4/ScSZ interlayer. Microstructures of theY4/ScSZ, Y2/YSZ, and WPC2/YSZ interlayers with the same sintering schedule (1345^{o}C for 6hrs) are compared in Figure 1-58. These microstructures showed a clear trend of denser ILs from WPC3, to Y4 to Y2 as Ca doping in these AE materials increases. The dense ILs could be due to the enhanced mass diffusion of Ca which facilitates the sintering of ILs. Consequently the loss in porosity at the interlayer explains the high polarization impedance observed in Y4 cells. All these results suggest that development of alternate AE materials should, instead of changing AE compositions, focus on the optimization of IL compositions and processing conditions in order to lower the cathode polarization resistance. As a result, alternative IL compositions and sintering conditions are being studied to enhance the overall cell performance of alternative air electrodes in the near future.

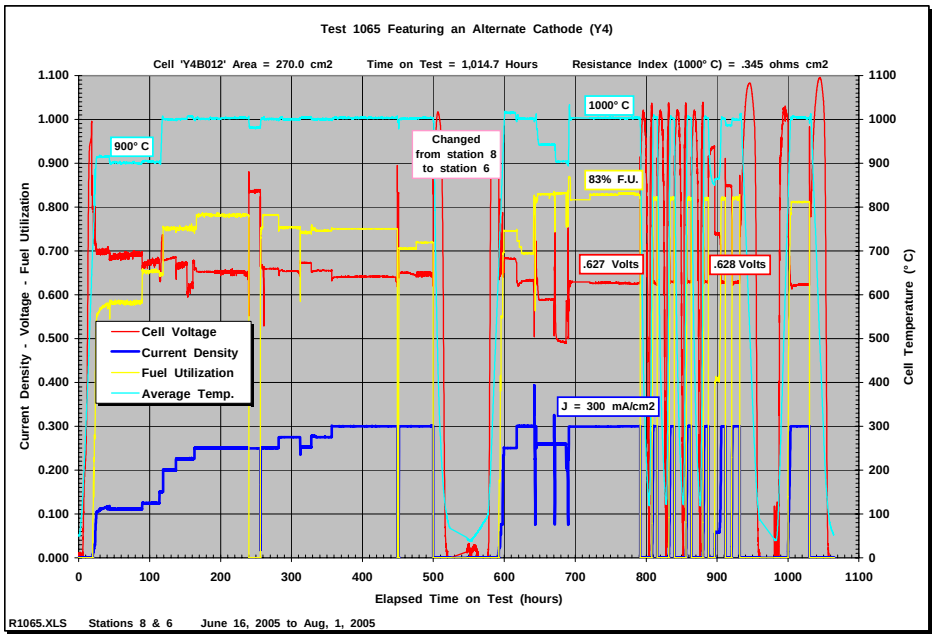

Figure 1-57. Electrochemical testing of the cell Y4B012 with Y4 air electrode

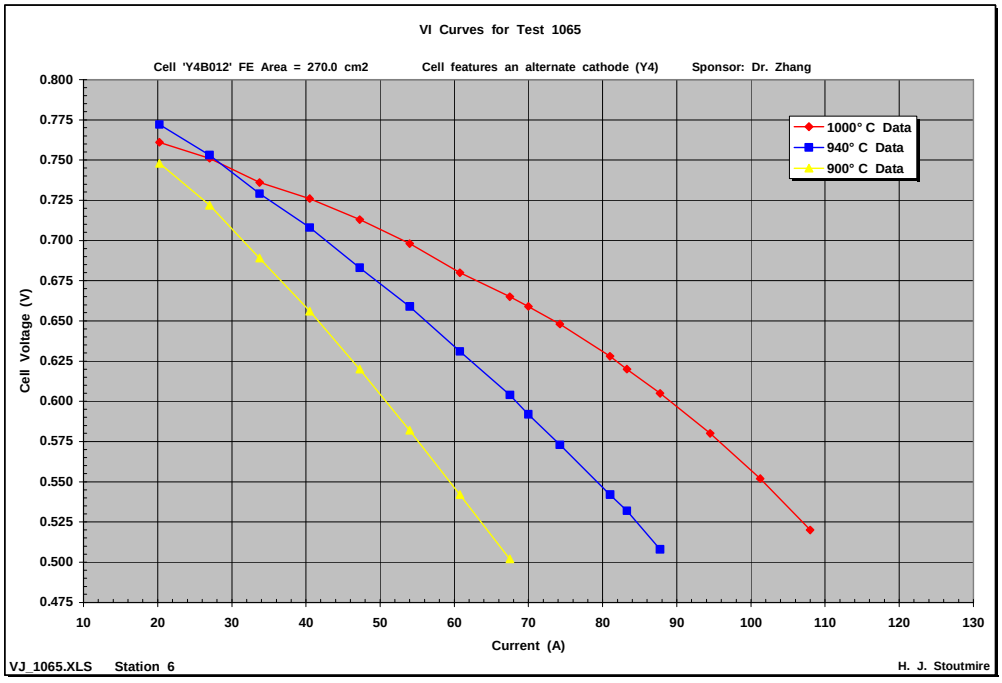

Figure 1-58. V-J curves of the cell Y4B012 at different temperatures

Cell testing results for the “Y4” cells so far have been very positive. Table 1-8 compares the performance of three cells at the standard 940°C operating point. Test 1111 is a standard production cell. Its performance is very close to the average for cells in the 125 kWe generator. Test 1101 has a “Y4” cathode, composite interlayer (C-IL), and a standard YSZ electrolyte.

Test 1110 is similar to 1101 but also has a ScSZ electrolyte. All of the cells have 50cm active length.

Table 1-8. Comparison of Standard Operating Point

Test Number	Cell Characteristics (Cathode, Interlayer, Electrolyte)	Voltage (V)	Current (A)	Fuel Utilization (%)	Resistance Index ($\Omega \cdot cm^2$)	Average Temperature (°C)
1111	WPC3, CeO_2, YSZ	0.639	70.0	82.8	0.447	941.4
1101	"Y4", C-IL, YSZ	0.674	70.1	82.7	0.405	940.8
1110	"Y4", C-IL, ScSZ	0.693	70.0	82.8	0.335	941.2

Cell performance at 900°C has also been very good. The stable electrical conductivity of this material is reflected in the lack of performance degradation seen in Figure 1-59. A typical WPC3 cell is shown in Figure 1-63 for comparison.

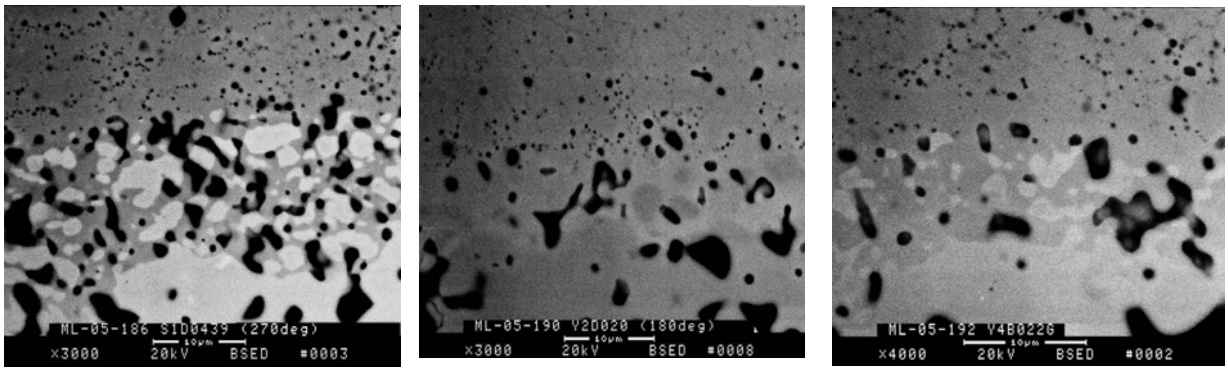

WPC3/ScSZ IL, 1345C/6hrs (ML-05-186)

Y2/YSZ IL, 1345C/6hrs (ML-05-192)

Y4/ScSZ IL, 1345C/6hrs (ML-05-192)

Figure 1-59. Comparison of the microstructures of interlayers made of different Y series AE and electrolyte materials sintered at 1345°C for six hours

In fact, all of the "Y4" cathode tube cells tested so far have shown improvement after being cooled from 1000°C to 900°C. Test 1087 improved from 645 mV to 654 mV (Figure 1-60), test 1101 improved from 648 mV to 662 mV (Figure 1-61), and test 1110 improved from 659 to 675 mV (Figure 1-62). This type of improvement is common for new cells at 1000°C and is referred to as the "break in" effect. "Break in" is believed to be related to the establishment of thermodynamic phase equilibrium at the cathode electrolyte interface. When a cell begins testing, the interface reflects the higher temperatures which it experienced during cell processing. As the cell is tested, the interface slowly changes to reflect the thermodynamic phase equilibrium of the operating temperature (usually 1000°C -- Current density may also influence equilibrium.). For the Siemens cell, the equilibrium at 1000°C is more favorable for cell operation than the equilibrium at cell processing temperatures, and consequently, cell performance improves as the cell "breaks in." The addition improvement seen at 900°C

suggests that the thermodynamic phase equilibrium at 900°C is even more favorable for cell operation than it is at 1000°C.

The additional "break in" at 900°C, however, has never previously been observed in cells made with WPC3 cathodes. Here it is apparently masked by the increase in resistance for WPC3 cathodes at this temperature (Figure 1-63).

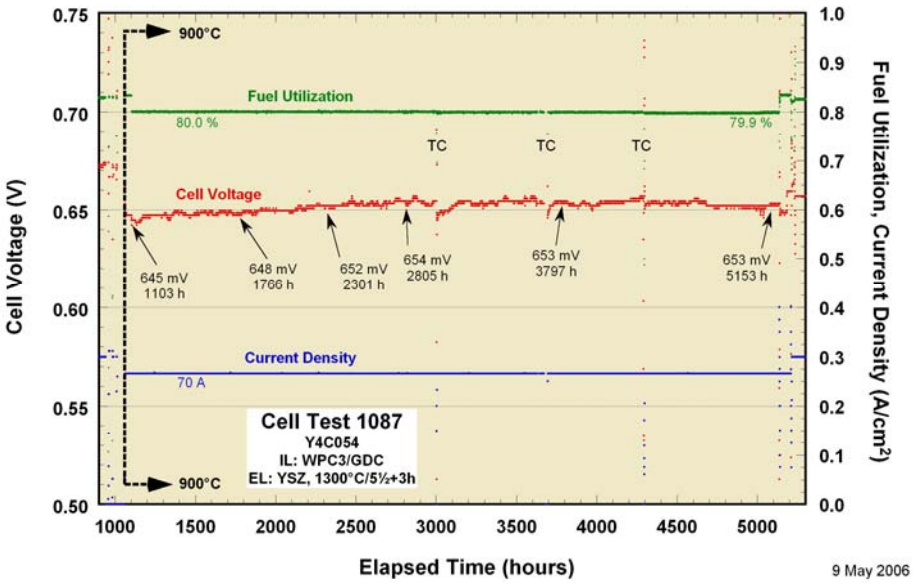

Figure 1-60. Voltage stability plot for test 1087 at 900°C

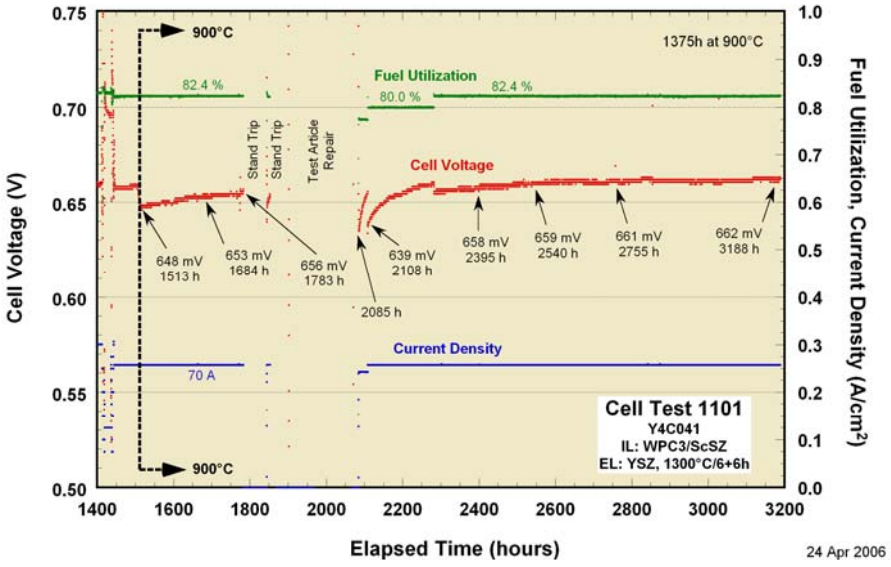

Figure 1-61. Voltage stability plot for test 1101 at 900°C

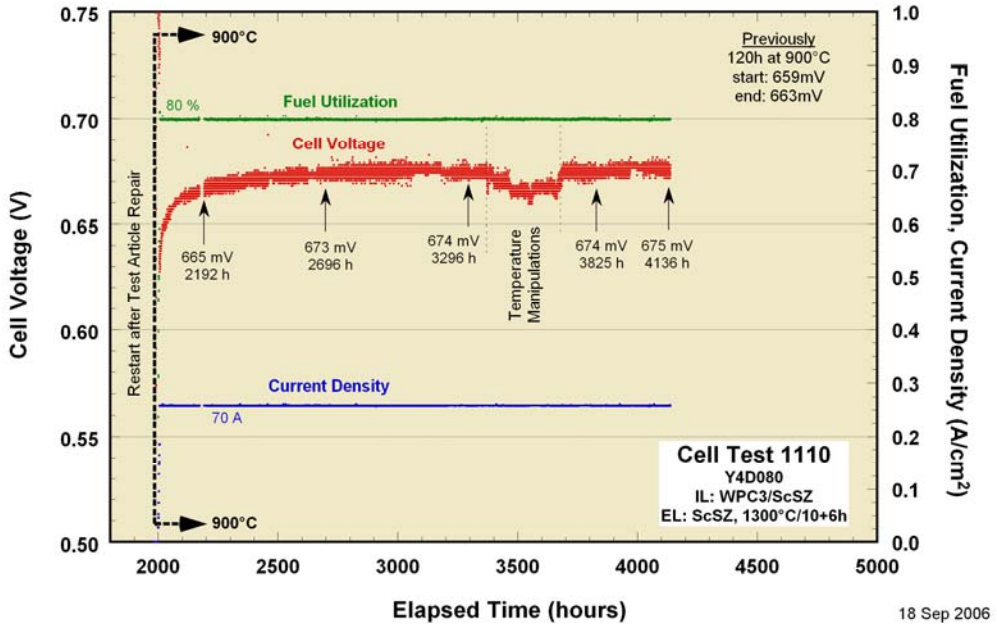

Figure 1-62. Voltage stability plot for test 1110 at 900°C

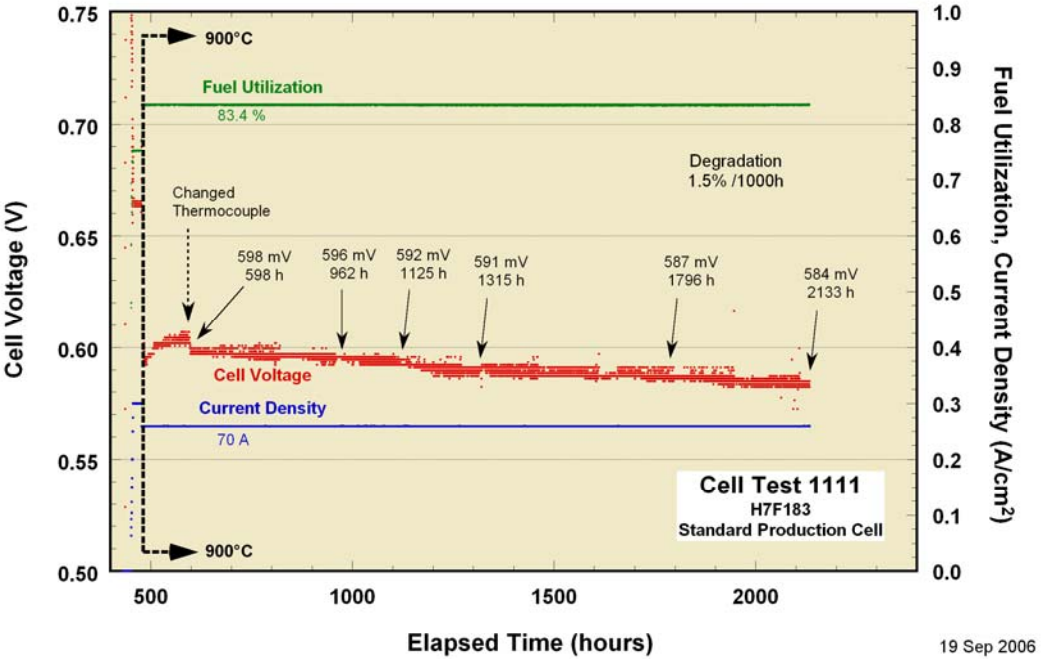

Figure 1-63. Voltage stability plot for test 1111 at 900°C

1.6.3.2.1.4 Test of Y4 AE with GDC Based Interlayer

Efforts continue to make Y4 cells with GDC based interlayers. One of the interlayers tailored for low temperature applications is GDC based composition which showed low interfacial resistance with ScSZ electrolyte in previous impedance tests. Since there are still some peeling issues when depositing ScSZ electrolyte on GDC based interlayer, a Y4 cell (Y4C054) with WPC3/GDC composition IL and YSZ EL was made and tested. Microstructure of the cell IL was examined in Figure 1-64. The back scattered image shows the interlayer of about 20μm thick with well defined, homogeneously distributed dark WPC3 phase, bright GDC phase, and pores. As shown in Figure 1-65 the electrochemical test (1087) was performed on the same cell. The cell achieved 0.682V at 300mA/cm^2 under 85% fuel utilization at 1000^{o}C and 0.610V at 900^{o}C, which is 40mV and 60 mV, respectively, higher than a standard WPC3 cell with CeO_2 IL and YSZ electrolyte.

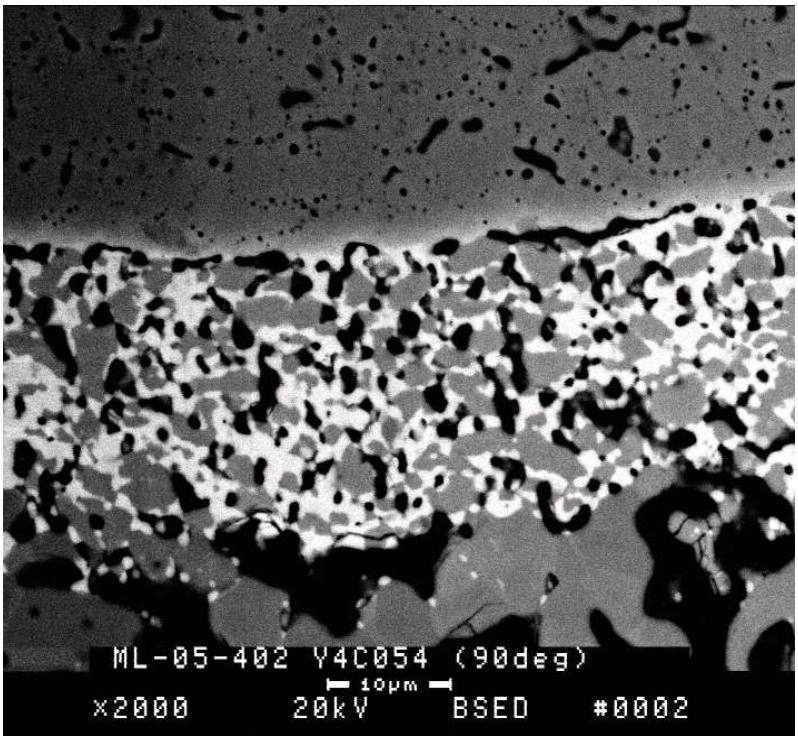

Figure 1-64. SEM picture showing the WPC3 and GDC interlayer microstructure (middle) of the cell Y4C054 (test 1087)

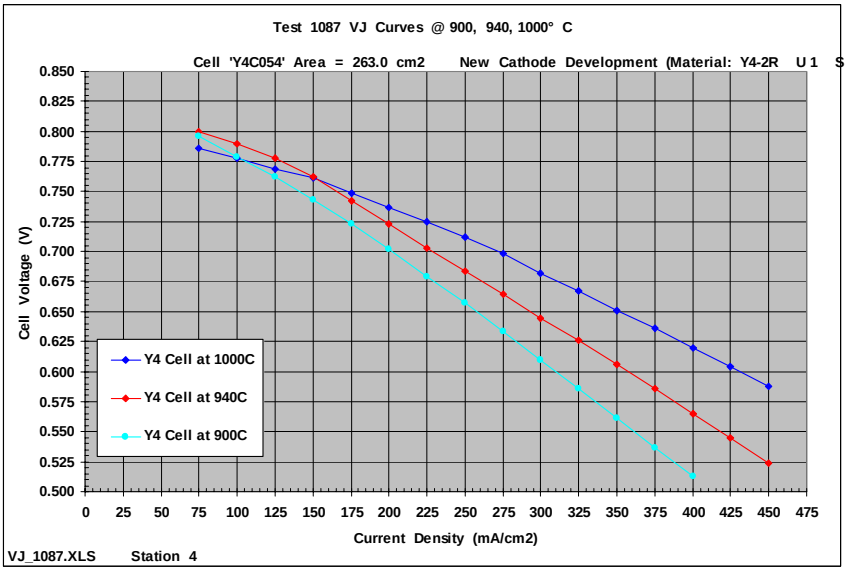

Figure 1-65. VJ curves of the cell Y4C054 at different temperatures

Long term test was also carried out with 70A loading and 80% fuel utilization at 900°C. Figure 1-66 shows that the stability test lasted for almost 4000 hours, and the cell performance improved 10mV from 0.643V and stabilized at 0.653V. This result indicates that both the Y4 air electrode and the new GDC based interlayer is very stable under the testing conditions.

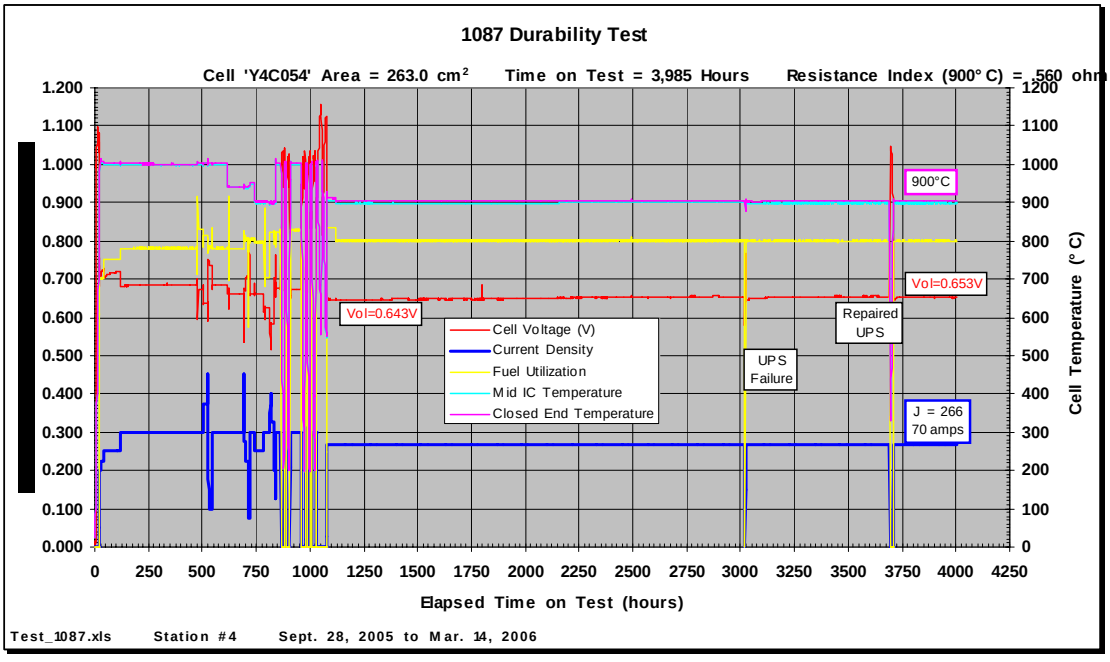

Figure 1-66. Long term stability test of cell Y4C054 at 900°C

1.6.3.2.1.5 Optimization of the Thickness of Interlayer

The main function of a cathode interlayer is to enhance interfacial kinetics of the oxygen reduction reactions without blocking its pore polarizations. This function is achieved by providing and extending the triple phase boundaries (TPBs) at the interface between the air electrode and electrolyte, which requires a thicker IL. In the meantime, to support electrochemical reactions ionic and electronic species should be effectively transported to or away from TPBs. In order to reduce the transport resistance, a thinner interlayer is preferred. As a result, an optimization of the IL thickness should be achieved through the tradeoff between these two factors.

In this study, effects of IL thickness on half cell impedance were carried out. IL thickness is directly determined by the number of coatings applied. To change the thickness, one cell (Y4B014-1-A) was coated with one layer while the other cell (Y4B014-2-A) coated with two layers. In Figure 1-67 both cells show similar microstructures but the thicknesses of two coatings almost doubled. Figure 1-68 showed the half cell impedance results. Both cells have similar ohmic resistances since they have the same AE and EL. However, profiles of pore polarization and charge transfer resistances behaved quite differently with IL thickness between these two cells. The cell with thin IL has significant higher charge transfer resistance as the total length of TPBs is limited. As the thickness of IL doubles, pore polarization increases as the pathway for transport of electrochemically active species, i.e. the oxygen ions and electrons, increase dramatically. Since charge transfer resistance and pore polarization change in opposite directions with IL thickness, the total cell impedance, which determines the overall cell performance, does not show significant difference. As a result, it seems that number of IL coatings and thus, the thickness of IL, can be reduced without significantly compromising the cell performance.

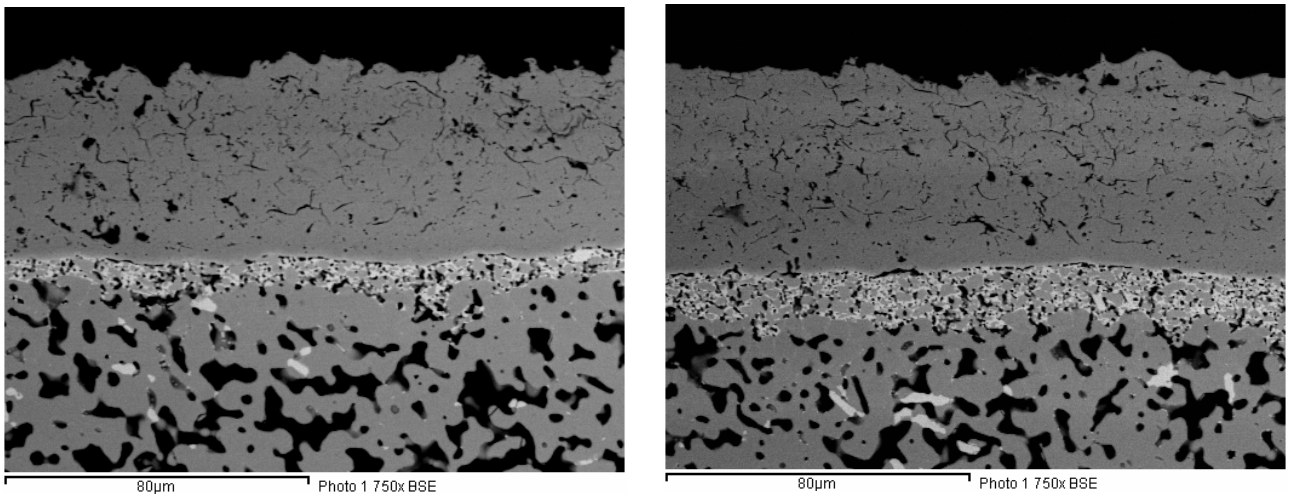

(a) *(b)*

Figure 1-67. Microstructures of WPC3/GDC interlayer of different thickness: a) One-layer coating and b) Two-layer coating

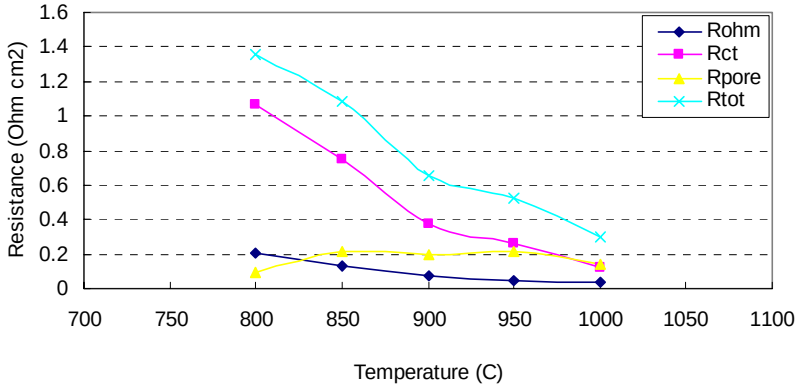

(a)

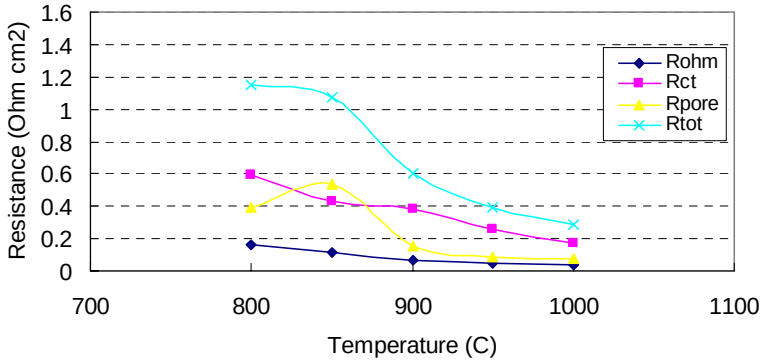

(b)

Figure 1-68. Impedance breakdown of (a) Y4B014-1-A with 1 coat-IL and (b) Y4B014-2-A with 2-coat IL

1.6.4 SEALS DEVELOPMENT

1.6.4.1 *Introduction*

In an effort to eliminate costly air feed tubes and lower air pressure drop, an once-through generator design was proposed, as shown in Figure 1-69 Air flows through inside fuel cell tubes while fuel flows on the outside. As a result, sealing materials separating air and fuel are needed between air electrode tubes and manifold, and a seals program was launched. The entire seals program consists of three phases of development. The first two phases, which are our current focus, include (1) finding good glass/ceramic sealing materials and (2) applying the sealing material on a HPD cell/bundle test. The third phase is to apply the technologies learned in the first two phases to a real once-through generator.

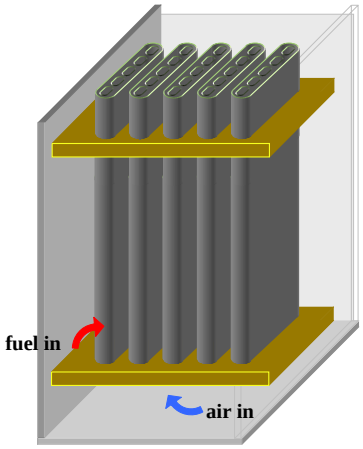

Figure 1-69. Initial concept of an once-through generator design

1.6.4.2 *Experimental*

Glass powders were processed in general according to the following procedures. Different metal oxides of desired formulation were well mixed and then heated up to 1400°C in a platinum crucible for two hours to melt the mixture. The melted glass was then cooled down, broken up, milled, and sifted through 400 mesh sieve. The as-made glass powder is ready for various materials compatibility tests, or made into bars for thermal expansion coefficient (TEC) measurements. For sealing tests, glass/ceramic powder is normally mixed with ethylene glycol or other organic agents to form a paste, which was used to seal air electrode tubes sections with ZrO_2 blocks or manifold coupons. The entire structure was then normally heated up to the glass/ceramic melting temperature for a certain period of time to achieve the final seals.

1.6.4.3 *Results & Discussion*

1.6.4.3.1 Performance and Properties of Seal Composition #57

Up to now, more than 60 glass/ceramic compositions have been extensively evaluated and a few of them showed promising results in the 800 to 900°C range. Among them, the #57 glass/ceramic was used to seal an AE tube section to a ZrO_2 block. The glass powder mixed with ethylene glycol was applied to the joint, heated up to 1050°C for half an hour, and then cooled down to room temperature. In order to test its reliability, the sealed structure was thermal cycled between 120 to 900°C for ten times. As seen in the Figure 1-70 he joint remained a hermetic seal and no cracks around the seal were observed.

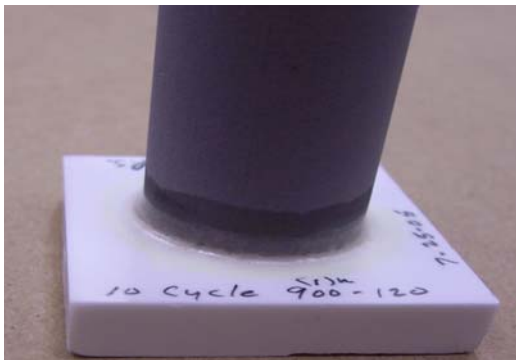

Figure 1-70. Picture of an AE tube section sealed to a ZrO2 block using #57 glass. The entire structure went through ten thermal cycles

Thermal expansion coefficient of the composition #57 was measured in air as shown in Figure 1-71. From room temperature to 650°C, the glass shows an almost linear thermal expansion behavior and the TEC is 10.49×10^{-6}/°C, which is very close to that of air electrode. Match in TEC between seals and air electrode minimizes stress generated on the seal during heat cycling as described in the previous section. Above 650°C, the glass/ceramic starts to soften, and higher mechanical compliance is expected in this temperature range, which is a preferred temperature range that the seal is operated in. Therefore, the composition #57 is designed ideally for 800 to 850°C.

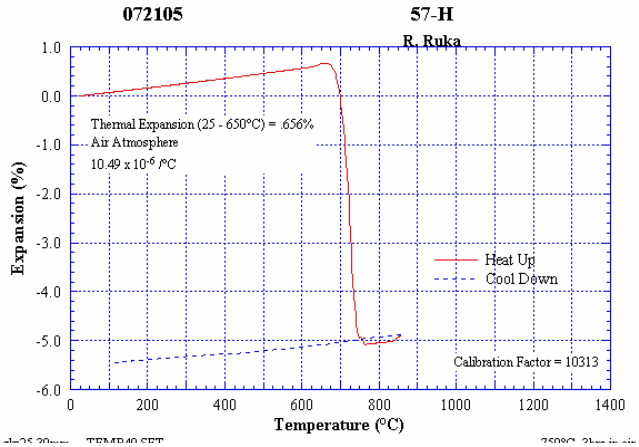

Figure 1-71. Thermal behavior of glass/ceramic seal composition #57

Composition #57 was also used to seal a HPD cell section to a sense ZrO_2 cap simulating the structure of HPD cells sealed to manifold. As seen in Figure 1-72, the glass also gives hermetic seal after being melted at 1050°C suggesting that sealing is independent on the shape of the cell.

Figure 1-72. Picture of an AE HPD section sealed to a sense ZrO_2 cap using #57 seal

1.6.4.3.2 Cell Protection from Chemical Attacks

Study of sealing cylindrical AE tubes with glass showed that the edge of bare AE tubes is sometimes vulnerable to chemical attacks by alkali metal ions in the glass. Because of the attack, tubes could break due to weakened bonding or stress generated at the bonding during heat cycling. To prevent or minimize the impact of glass, the cell edge needs to be coated for protection. Of the coating materials, doped ZrO_2 is a good choice since it has been used as the electrolyte material for the cell, and the technology for plasma spraying YSZ is well developed at Siemens. Therefore, the edge of the cell was plasma-sprayed using similar electrolyte spraying processes. As shown in Figure 1-73, for comparison the cell on the left is a bare HPD tube without any coatings on the end face while the edge of the cell on the right was plasma sprayed with YSZ. The coated cell can then be used for cell assembly. The coating is expected to protect the cell, and a cell with coated edge is being on test now.

Figure 1-73. Comparison of H PD once-through cells without (left) and with (right) plasma-sprayed YSZ coatings

1.6.4.3.3 Plasma Spray of Manifold Surface

Manifolds made of Spinel materials by using Blasch's injection molding process could be 20-30% porous which results in gas leakage between air and fuel. Different methods of coating surfaces of manifolds to prevent the leak were carried out. First, the surface of the manifold was sealed with various glasses. Our team in Erlangen has demonstrated this concept as shown in Figure 1-74 The surface of test article made of Spinel material is completely covered and sealed with glass after sintering giving the manifold a gas tight seal. Though applying glass is successful, concerns of exposing a large area of glass in reducing environment still remain. As a result, instead of using glass, surface of the manifold can be plasma sprayed with YSZ. As shown in Figure 1-75 the testing article made of spinel material were coated with YSZ using the same spraying parameters as Siemens standard electrolyte spraying conditions. After it was sprayed, the sample was sintered at 1345^{o}C for 6 hours and a dense layer on the surface was obtained. Four cylindrical cell sections were sealed to the coated board without any problems. Compared with glass and YSZ, YSZ is preferred for surface coating since the coating process can be achieved with minimal changes in production and area of glass exposed to reducing environment is limited.

Figure 1-74. Picture of surface of a manifold sealed with glass

Figure 1-75. Pictures of spinel manifold testing coupons with surface plasma-sprayed with dense YSZ layer. The picture on the left is a bare sample without coating. The one on the right side was coated with YSZ and sealed with four cylindrical tube sections

1.6.4.3.4 Apllication of Epoxy on Seal

Another practical issue was raised regarding sealing using glass paste. After glass paste is applied on the joint between the cell and manifold, the glass will be dried over time leaving almost no bonding strength between these two parts. In order to hold the glass in position during cell assembly process, fast-setting epoxy is applied after the glass is dried out. Figure 1-76 shows a picture of hardened epoxy on a cylindrical tube and ZrO_2 block assembly sealed with glass. The hardened epoxy provides sufficient bonding between the tube and block and keeps dried glass powder in place. The entire assembly was then heated to 1050^oC for half an hour in 5%H_2/N_2 balanced with 11% water. Epoxy started to be burned out at approximately 320^oC, and minimal carbon is left after the burning process. Bonding using Epoxy was used and a single cell has been successfully assembled.

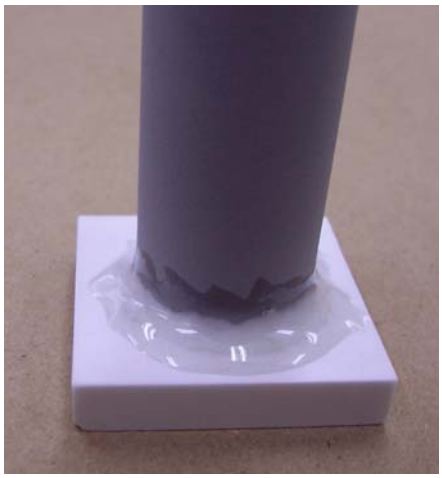

Figure 1-76. Epoxy was applied on the glass powder at the joint between a cylindrical cell section and ZrO2 block

1.6.4.4 *Summary*

In order to build an once-through generator, sealing materials are needed. In the seals program, over 60 glass/ceramic sealing compositions were evaluated. Among those promising candidates, #57 has a TEC ($10.49\times10^{-6}/^oC$) matching that of AE and has been successfully used to seal tubular and HPD cell sections with ten thermal cycles. In order to protect the cell from chemical attacks from glass, the edge of a HPD cell has been plasma-sprayed with YSZ. Blasch porous manifolds can be sealed on surface by using glass; however, the preferred way to do is to plasma spray YSZ on the surface in order to cut down the areas of glass exposed to reducing atmosphere. Both approaches have been demonstrated. Lastly, epoxy was applied on top of sealing materials at the joint so that the sealed structure can maintain mechanical integrity during cell assembly.

1.7 HPD CELL TESTING

1.7.1 SINGLE CELL TESTING

1.7.1.1 *Introduction*

1.7.1.2 *Experimental*

Test 1000, a HPD5R1 qualification cell, was terminated after reaching about 4000 hours. The newly designed and fabricated Delta9 cell was electrically testing (Test 1050) passing 3000 hours of operation and greatly improved the wattage on a cell basis. A ScSZ HPD5R1 cell (Test 1083) was tested as a qualification cell for the POC2. Test 1086, the first HPD5R1 once thru cell was tested using a homemade seal and a dense zirconia cap.

1.7.1.3 *Results and Discussion*

Figure 1-77 illustrates the lifetime plot for Test 1000. This HPD5R1 cell ran for about 4000 hours, of which 2200 hours operating at 400mA/cm^2. The standard operating current density of cylindrical cells in cell testing is 300mA/cm^2. This test shows that operation at higher current density is possible with HPD cells with negligible voltage degradation.

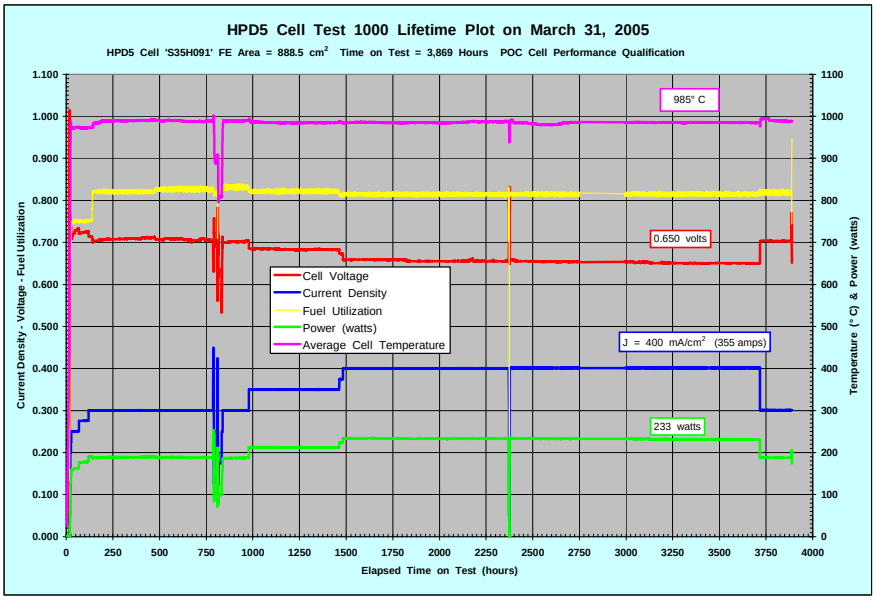

Figure 1-77. Lifetime plot for Test 1000, showing good voltage stability for about 4000 hours

Figure 1-78 shows the lifetime plot for Test 1050 or the new Delta9 cell. This cell was operated for 3000 hours, of which 1800 hours operating at 500mA/cm^2. This test pushed the current density envelope even higher than Test 1000. This is a remarkable achievement as it shows good performance at very high power densities. The cell experienced no voltage degradation throughout the duration of the test. The test terminated in order to run other tests.

In Figure 1-79, the area specific electrical performance of our current cells is updated reflecting the new Delat9 cell test. The voltage and power density of the four geometries is plotted as a function of current density. The advantage of the HPD geometry can be readily seen. For instance a typical cylindrical cell operates at a cell voltage of 0.65 Volts and 300mA/cm^2 while a HPD5 can operate at a cell voltage of 0.65 Volts and 400mA/cm^2. This translates to a 33% improvement in power density. The first HPD10 cell test shows improvement over the HPD5 cell and confirms the benefit of increasing the number of conductive paths or ribs. The result is encouraging as the HPD10 can operate at a cell voltage of 0.65 Volts and 475mA/cm^2. This translates to a 58% improvement in power density over cylindrical cells. It is worth noting is that this is the first HPD10 cell test and further improvement is to be expected as the manufacturing process matures. The Delta9 cell shows the same characteristics of the HPD10 however the real benefit of this cell will be shown later. As for the HPD10, this is a first cell test and by no means optimized. In other words, the cell performance is likely to increase further.

In Figure 1-80 the cell voltage and cell power is plotted against the cell current. The benefit is more evident when one compares the cell power for the different geometries. A typical full length cylindrical cell can produce about 190 Watts at maximum power. At the same conditions an HPD5 cell can produce about 270 Watts and a HPD10 reaches about 300 Watts. The benefit of the Delta9 is now evident as a maximum power of 416 Watts is reached, a worldwide record for a single cell test. It worth noting that these improvements have been achieved with cells having half the active length of standard cylindrical cell.

In Figure 1-81 the lifetime of Test 1083 is shown. This cell is qualification cell test for HPD generator POC2. This HPD5R1 is a full ScSZ cell. The cell voltage is stable over its lifetime and matches a prior cell test with ScSZ. After 375 hours the top furnace heating element failed, and the article was cooled down in order to repair the furnace.

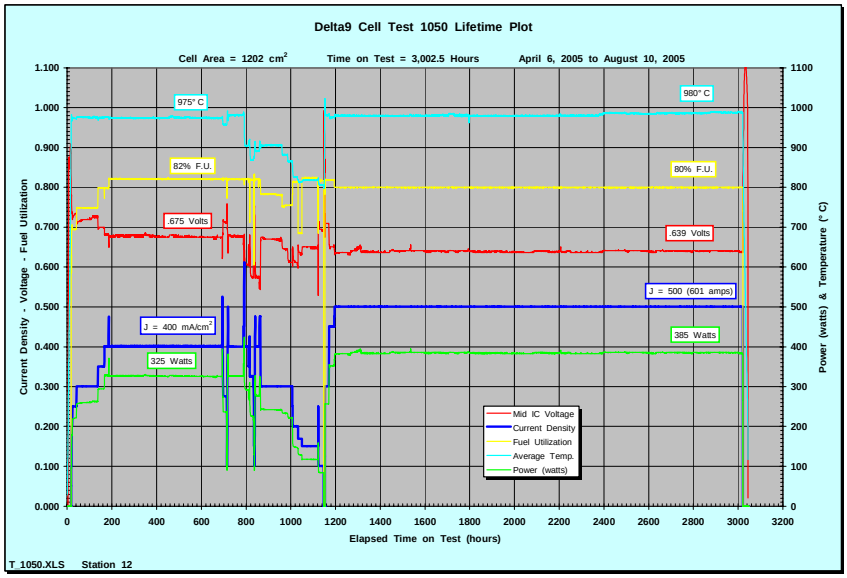

Figure 1-78. Lifetime plot for Test 1050, this Delta9 cell run at very high current density for about 1800 hours without any voltage degradation

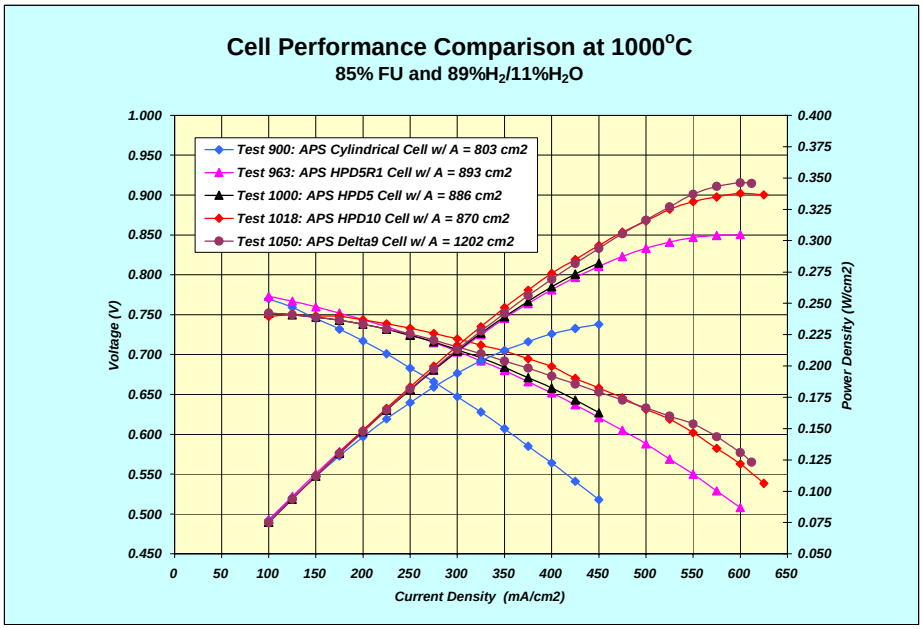

Figure 1-79. Area specific electrical performance for cylindrical, HPD5R1, HPD10R1, and Delta9 cells at 1000°C

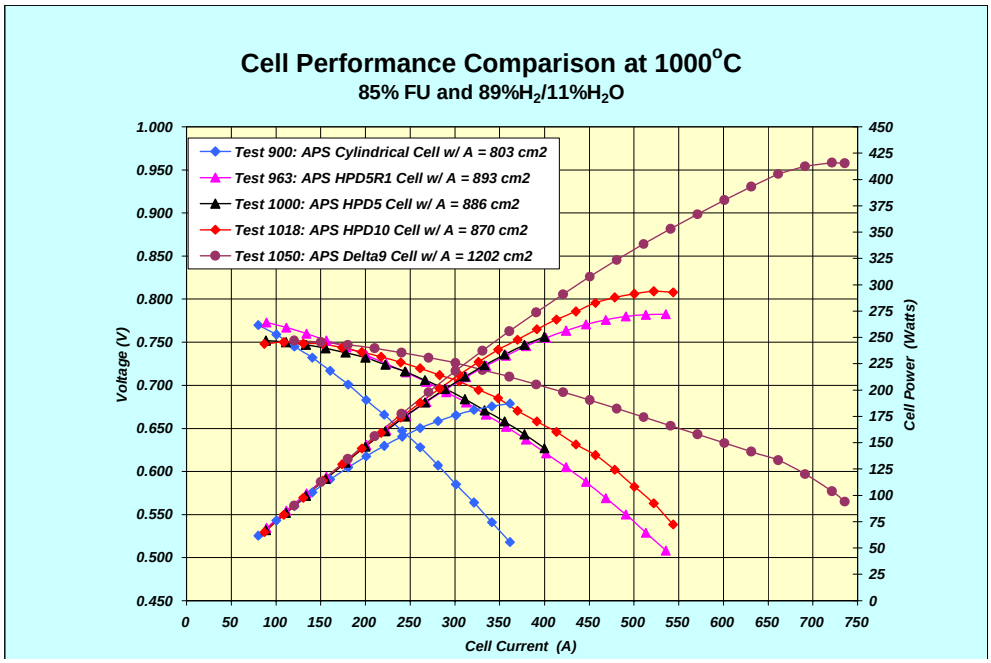

Figure 1-80. Electrical performance on a cell basis for cylindrical, HPD5R1, HPD10R1, and Delta9 cells at 1000°C

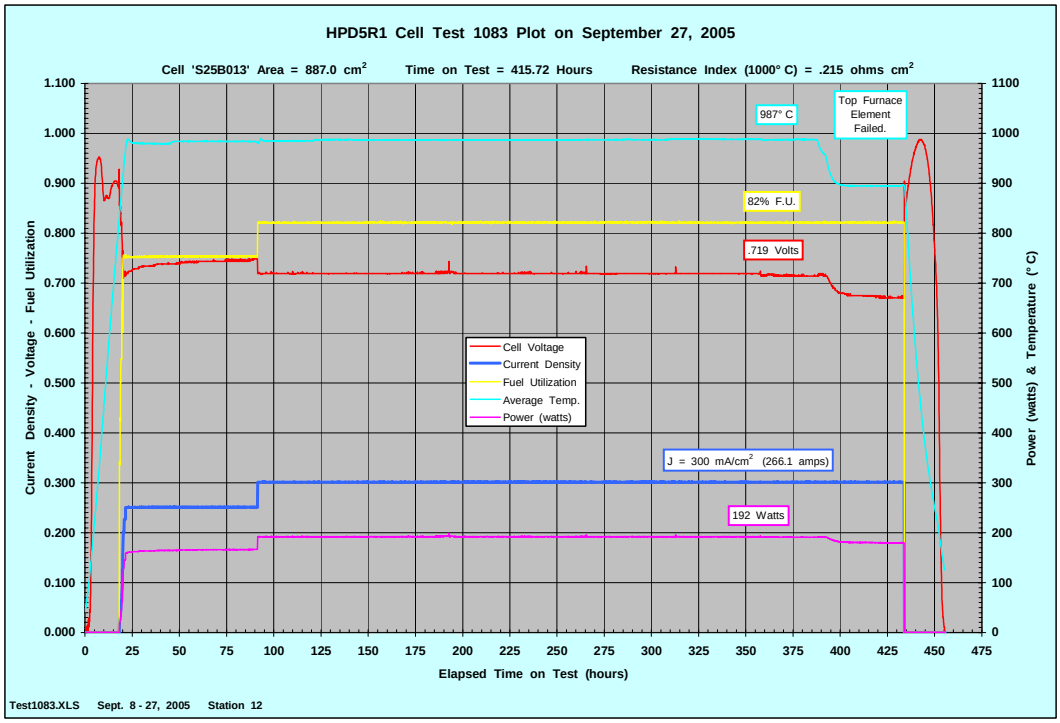

Figure 1-81. Lifetime plot for test 1083, HPD5R1 cell with ScSZ electrolyte, a qualification cell for the POC2

In Figure 1-82 the lifetime of the first seal test is shown (Test 1086). The seal region is kept at 800°C in order to avoid large volatization of the components. This results in a lower average cell temperature. However, future seal development will focus on a seal with a wider operating temperature. The fuel utilization is kept low in order to avoid low combustion temperatures, and therefore it helps to keep the cell open temperature higher by preheating the incoming air. The cell voltage is still improving as the cell conditions, and the seal is stable for the duration of the test (210 hours). The test will continue in order to determine the stability of the seal material.

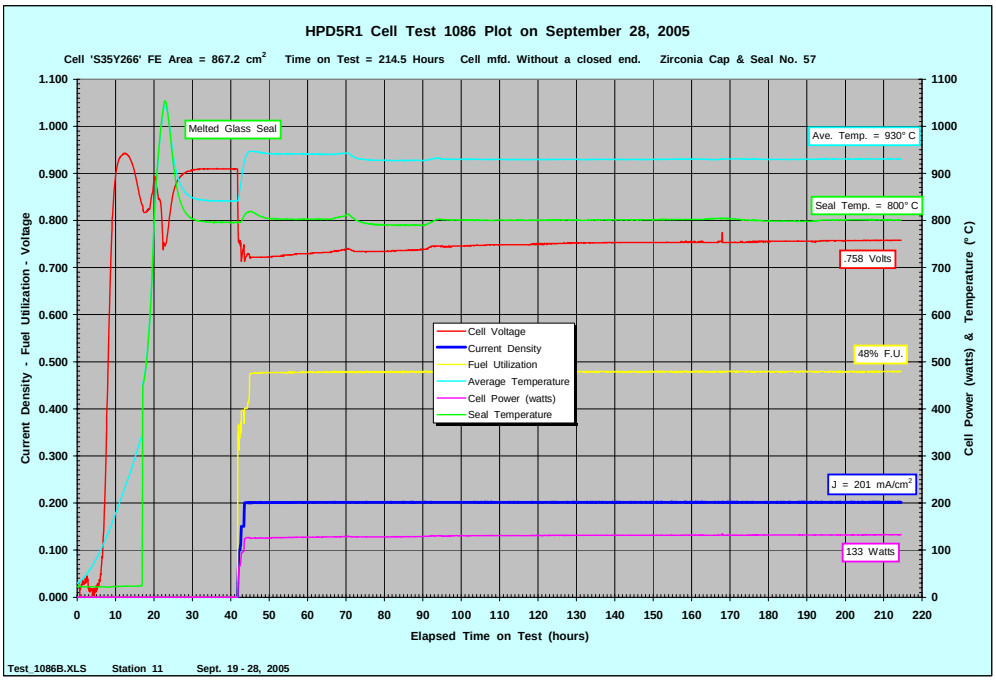

Figure 1-82. Lifetime plot for test 1086, a HPD5R1 cell with a Zirconia cap and seal

The purpose of test 1109 is to study the combined effect of new low temperature electrolyte Sc-doped ZrO_2 and geometry on cell performance. The ScSZ material was used for electrolyte, cathode interlayer and anode. The standard manufacturing process was used to make various layers.

Figure 1-83 shows the V-J characteristics measured with fuel utilization 80% of inlet fuel of 89% H_2/11% H_2O and 6 air stoich at different temperatures. The overall performance represents the best among the cells ever fabricated in Siemens, indicating the combined benefits from material and geometry. A representative performance at 1000°C is illustrated by V_{cell}=0.695 volt at J=600 mA/cm^2. The resistance index for ScSZ HPD10 cell ranges from 0.127 at 1000°C to 0.375 Ωcm^2 at 800°C; the latter is typical for cylindrical cell at 1000°C, implying the operating temperature of ScSZ HPD10 cell can be reduced to 800°C but still maintaining the performance of cylindrical cells at 1000°C.

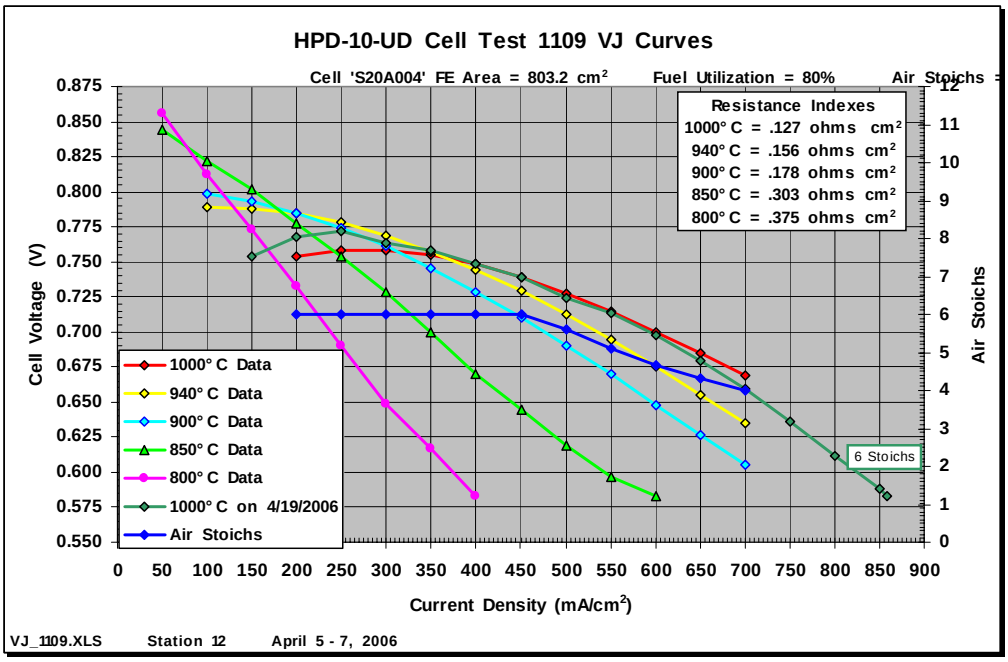

Figure 1-83. V-J characteristics of ScSZ-based HPD10 cell

The long-term stability is shown in Figure 1-84, where the cell voltage is plotted against time. A number of spikes on the chart represent various transients associated with characterizations. After 500 hours, the cell operates under stable condition without interruption, showing a stable cell voltage. Currently, the cell is under stability test at 900°C.

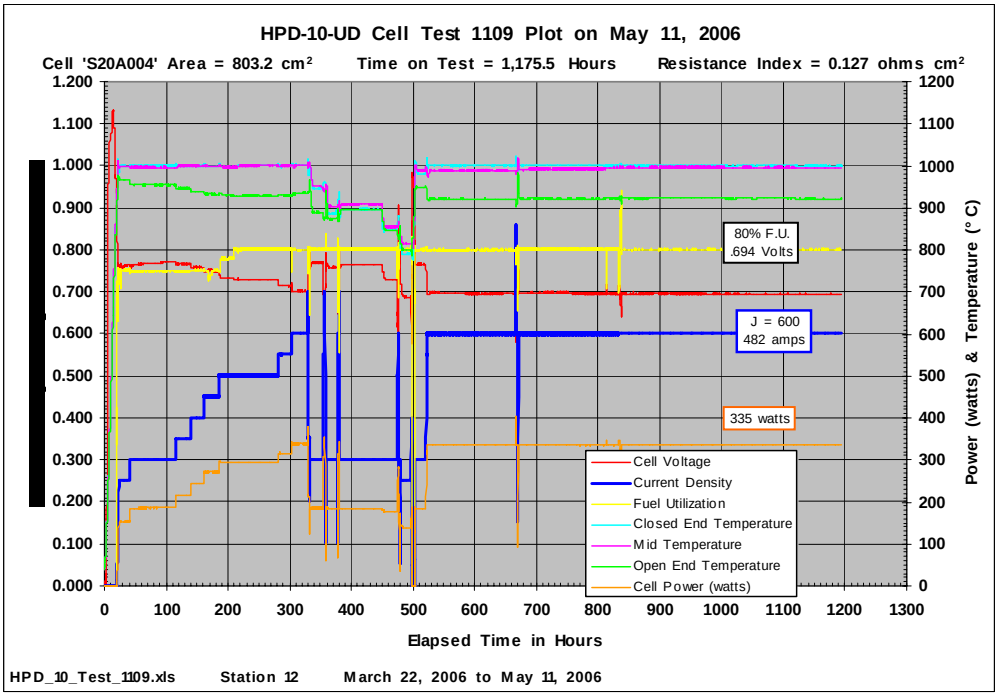

Figure 1-84. Lifetime plot of ScSZ-based HPD10 cell

A one meter length Delta-9 cell is exercised in test 1122. The typical length of IC for HPD/Delta cells is 75 cm. To show the feasibility of increasing cell power by scaling-up cell area, a Delta 9 cell with 100 cm long IC was fabricated and tested. Figure 1-85 shows the V-I and P-I curves measured at 1000°C. Note that the active cell area is 1382 cm^2 as opposed to 1200 cm^2 for 75-cm long Delta 9 cell. The resistance index is very low, <0.1 Ωcm^2, well expected from the benefits from ScSZ material and geometry. At the nominal operating voltage of 0.70 volt, the cell power is approximately 330 W as opposed to 285 W for 75-cm long Delta 9 cell. The peak power is extrapolated to be roughly 550 W at cell voltage of 0.50 volt. The performance shown in Figure 1-85 confirmed that the scale-up cell area could increase the cell power proportionally.

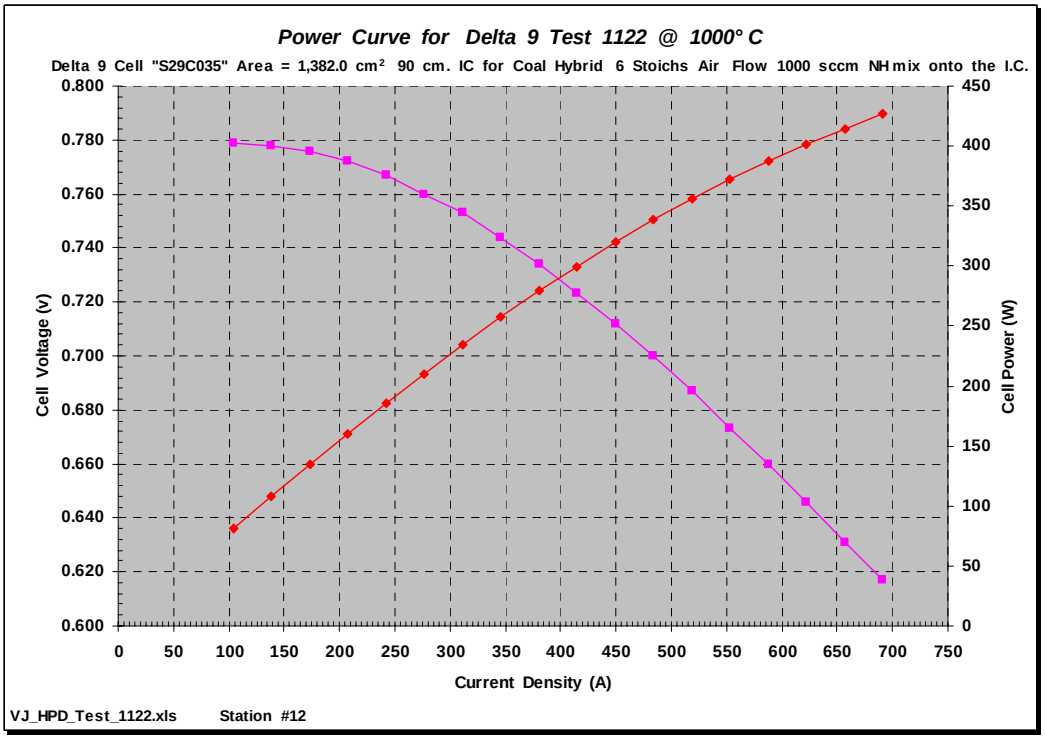

Figure 1-85. V-I and P-I curves of 1-m long Delta 9 cell at 1000°C

The lifetime plot of the cell is shown in Figure 1-86. Over roughly 1000-hour testing, the cell voltage shows a slight degradation over time. Examination of cell resistance index indicates no change over time, implying increasing polarization may be the cause. Another speculation is that there are two internal fuel heaters, with which gaskets are used. Due to the exposure to high temperature, these two gaskets may lose their elasticity, therefore the seal between anode and IC chambers may deteriorate. As a consequence, the fuel could severely bypass, leading to decline in cell voltage.

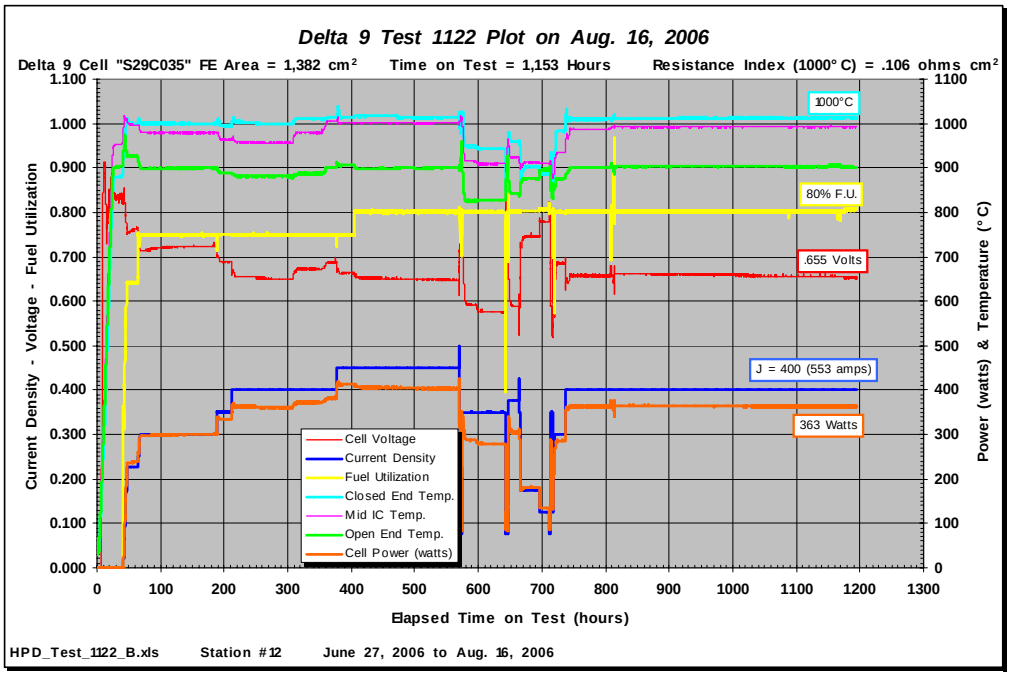

Figure 1-86. Lifetime plot of 1-m long Delta 9 cell at 1000°C

1.7.1.4 *Conclusion*

The power density of the tubular type SOFC has been improved by modifying the geometry from cylindrical to flattened tubes of different types. The geometry has reduced the cell resistance and in turn lowered the ohmic losses. The increase anode surface area has increased performance so that more watts can be produced per cell. Worth noting is that the power enhancement at a 1000°C is due to geometry alone and does not include the benefit if more advanced materials were to be used. Further improvement in performance can be obtained by using more advanced material such as Scandia Stabilized Zirconia especially at lower temperatures. It is expected that a combination of advanced materials and the new geometries will bring Siemens Power Corporation SOFCs performance to even higher levels of performance.

1.7.2 MULTICELL TESTING

1.7.2.1 *Introduction*

1.7.2.2 *Experimental*

The bundle assembled with Ni-foam cell-to-cell connectors was tested. During the loading process one of the cells failed at the closed end cap. The failure mechanism seems to be related to the current density concentrating to the closed end region.

1.7.2.3 *Results and Discussion*

The lifetime plot of the bundle Test 943 is shown in Figure 1-87. The test article was brought to temperature and the open circuit voltage indicated the all cell were healthy. Upon the initial loading, about 100 Amps, the voltage started to decline very quickly while the closed temperatures increased. This has been always an indication of failure near the closed end of the cell. The test was cooled down and upon disassembly a broken cell was found. It is believed that the current density, concentrated at the closed end, may have played the major role during the cell failure. At this time, it is expected that this test will be repeated in order to prove out the Ni foam bundling technology once more cells are available and priorities allows.

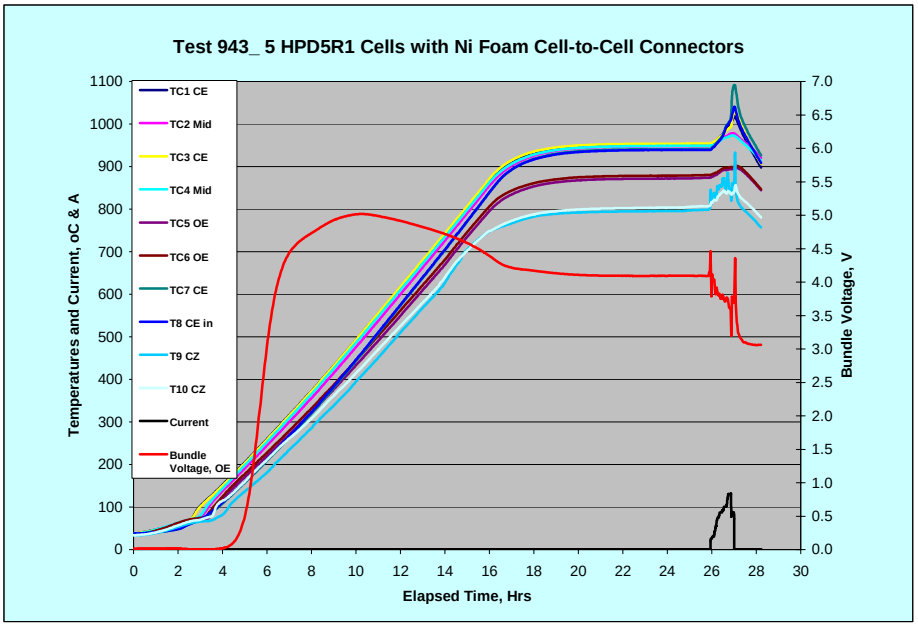

Figure 1-87. The lifetime plot for the bundle test

1.7.2.4 *Conclusion*

The bundle test intended to prove out the new Ni foam technology was tested. During the initial loading, one of the cell cracked which terminated the test. It is expected that this test will be repeated.

2. SOFC GENERATOR DESIGN AND DEVELOPMENT

2.1. DEVELOPMENT OF OPTIMIZED DESIGN FOR THE SEAL-LESS PLANAR AIR ELECTRODE (CATHODE) SUPPORT TUBES

2.1.1. RESIDENTIAL DETAILED DESIGN FOR POC

The SECA Proof of Concept (POC) unit is a fully integrated natural gas fueled power system of nominally 5 kWe capacity utilizing Siemens high power density [HPD5R1] solid oxide fuel cells. A primary objective for Phase 1 of the SECA program is the successful demonstration of the POC unit. The minimum requirements for success have been defined by DOE to include: dc peak power between 3 and 10 kWe; net dc efficiency of at least 35% [net dc/LHV]; 1500 hours of operation; steady state degradation rate less than 2% per 500 hours of operation; 80% availability; nine power cycles; one thermal cycle.

The design of the POC borrows heavily from Alpha unit of Fuel Cell Technologies [FCT], a collaborator with Siemens Stationary Fuel Cells in the development of residential class SOFC power systems and a sub-contractor to Siemens in the SECA program.

The POC generator employs thirty six HPD5R1 cells with scandia doped zirconia electrolyte. Six cells are bundled in electrical series comprising a short stack. Six bundles are then arrayed into two rows of three bundles each with the flat side of the cells parallel to the face of the cell row. Cell bundles are interconnected in electrical series. The two cell rows flank the internal reformer that separates the rows. Figure 2-1 shows a bundle of HPD5R1 cells.

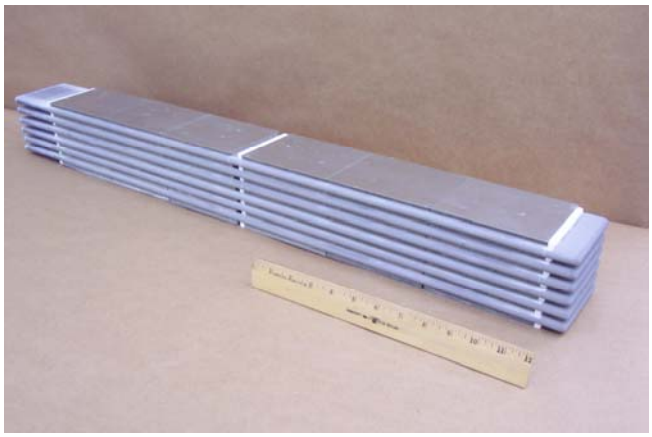

Figure 2-1. Bundle of six HPD5R1 solid oxide fuel cells

Process air feed tubes passing through insulation boards located above the cell open ends comprise the counter-flow internal recuperator. A natural gas driven ejector located above the reformer recirculates a portion of the anode exit gas, mixes it with fresh fuel and drives the mixture through the reformer. From the reformer exit, at the lower end of the generator

assembly, the reformed fuel is distributed to the closed end of the cells at the bottom of the generator assembly. The flow path for air, fuel, and exhaust can be seen in the flow schematic of Figure 2-2 . The generator module in turn is integrated with a balance of plant or BOP to form the power system. The generator module and BOP are housed in an enclosure.

The FCT Alpha generator module, which used tubular cells, utilized flat plate-style guard heaters located around the stack periphery on the exterior of the inner canister to heat the SOFC stack. This style of heating was judged to yield excessive temperature gradients within the HPD cell stack. To obtain more uniform stack heating, an electric heater was designed to heat the combustion zone. A blower (separate from the process air blower) is used to supply air to the startup heaters. The hot air exiting the startup heaters will mix with the stack exhaust gas and heat the incoming process air via the internal recuperator.

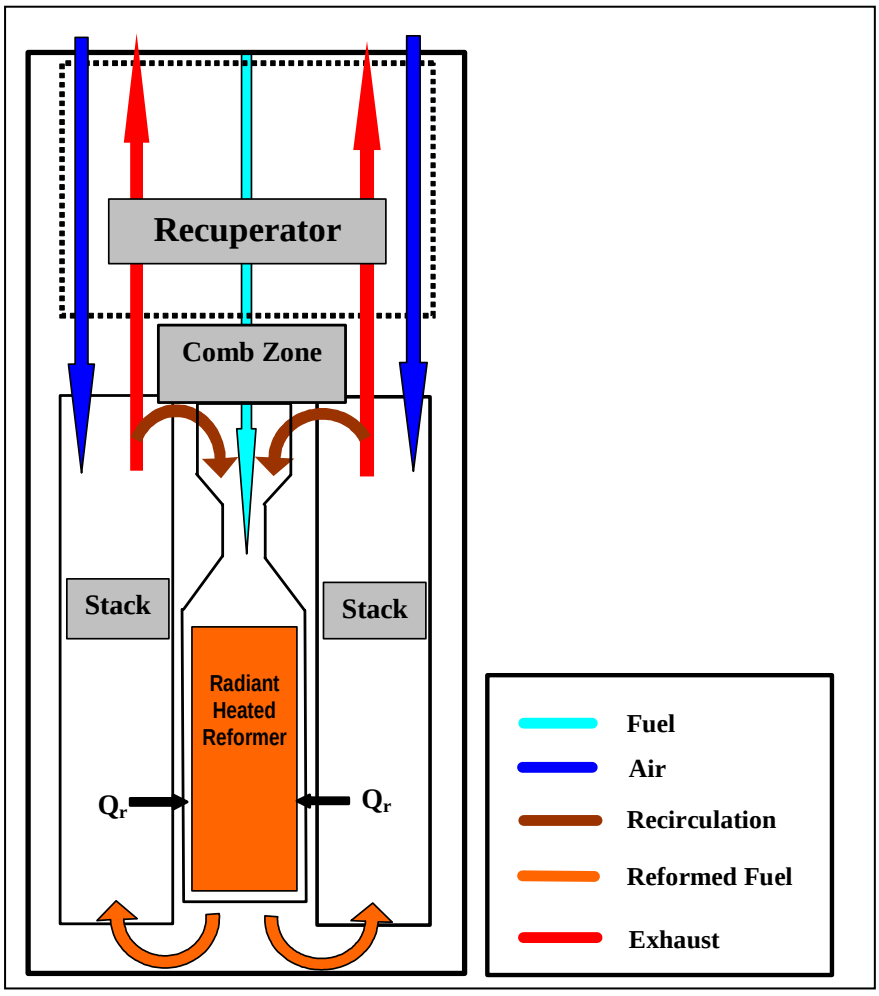

Figure 2-2. Flow schematic of POC generator module

2.1.2. POC SYSTEM & PERFORMANCE

A photograph of the POC system under test is shown in Figure 2-3. Operational data for the POC unit is presented in Figure 2-4. A comparison of observed performance against the requirements for the POC can be found in Table 2-1. In can be concluded that the POC has exceeded performance requirements.

Figure 2-3. POC system

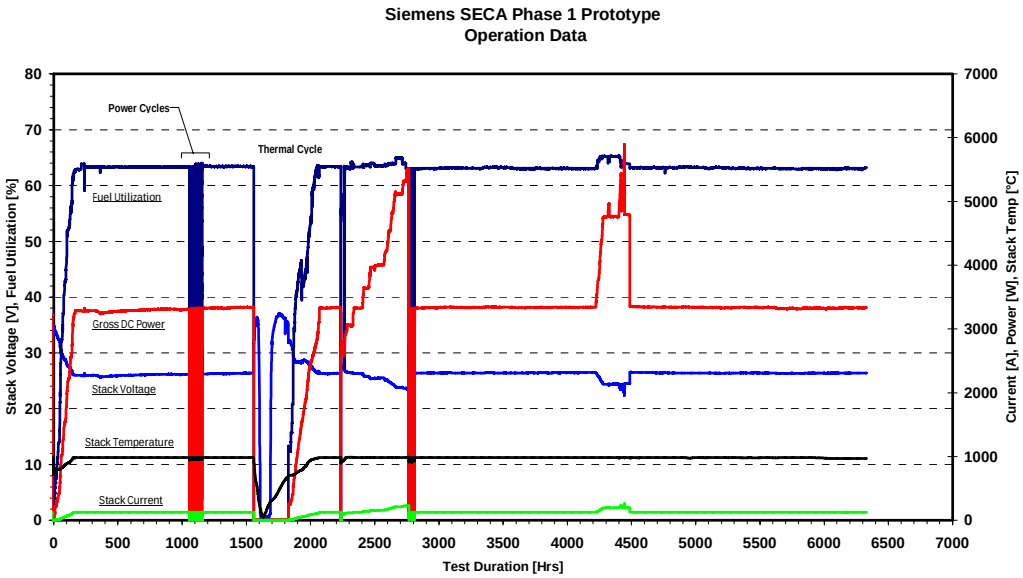

Figure 2-4. Operational data for SECA POC

Table 2-1. SECA POC – Summary of System Performance

Performance Parameter	Requirements	Results
Net DC efficiency	35%	38%
DC Peak Power (kW)	3-10	5.5
Steady State Degradation	< 2% per 500 hrs	0 (2% Power Enhancement)
Thermal cycle	1	1
Power cycle	9	9
Availability	80%	100%
Test Duration (hours)	1500	~3800 (Test continues)

2.2. COMPONENT DEVELOPMENT

2.2.1. LOW GAS PERMEABLE CERAMIC MATERIAL

2.2.1.1. External Surface Treatment Technologies (Blasch Prevision Ceramics)

Investigations by Blasch to develop external coating and treating technologies that could effectively close off ceramic porosity were terminated because success was not deemed possible within the limits of project schedule and resources.

2.2.1.2. Chemical Stability Testing of Silica in High Temperature Reducing Atmosphere

Currently, the temperature and pressures at reducing SOFC atmospheres whereby the silica in different ceramic materials becomes a contaminant are unknown. In the design stage for a ceramic housing liner for the beta residential SOFC, it is important to understand at what temperature and pressure the silica becomes a contaminant to the SOFC reducing atmosphere. With this information, it will be possible to determine by heat flow calculation the exact point in the thermal gradient of the lining where free silica-containing ceramic may be used. For example, if free silica were determined to no longer be a contaminant in SOFC atmosphere/ operating pressure at 500°C, and the thermal gradient of the ceramic lining goes from 900°C hot face to 100°C shell temperature, then silica contamination would be permissible from the center point of the lining thickness to the shell. This could be important with regards to deciding how thick the internal ceramic housing liner must be, and at what point in the overall SOFC lining thickness can lower cost ceramic insulating materials (which contain free silica) be used. Test Results have been inconclusive.

2.2.2. CERAMIC HOUSING COMPONENTS

2.2.2.1. Development of High Thermal Expansion Ceramic Material Compatible with SOFC Sealant

Blasch Precision Ceramics, in partnership with Siemens, has identified a high magnesia ceramic material, characterized by a reverse spinel stoichiometry, thermally compatible with the sealant being used in SOFC manufacturing. Also, Blasch developed a non-aqueous magnesia slurry and binder system capable of forming complex three-dimensional shapes that would not distort significantly upon subsequent debinding and firing processes. As a brief summary, this work included:

- Investigation of several binder systems, allowing for easy formability and adequate green strength of reverse spinel ceramics
- Investigation of several mold materials, allowing for easy release of the green ceramic parts from the molds
- Tailoring of the composition to match the thermal expansion coefficient of the SOFC sealant (CTE = 10.5 x 10^{-6}/°C)
- Successful forming of reverse spinel shapes, ranging from simple bars and discs to more complex nozzles and cups
- Successful forming of a simplified prototype SOFC plate, as supplied by Siemens
- Initial optimization of the debinding and firing cycles in an attempt to reduce or eliminate defects observed in the final shapes

Development of mold-making and shape-making technology for reverse spinel ceramics saw the successful casting of a relatively simple plate design and a few truly three-dimensional shapes. As opposed to the simplified plates, these final shapes possessed more complex geometry on the face of the parts as well as an increased overall thickness (max. ¾" thick). Such features lead to further challenges in mold fabrication, part forming, and subsequent debinding and firing processes.

Critical to the ability to mold and subsequently form complex reverse spinel shapes is a dimensionally accurate rapid prototype model. Any deficiencies present in these models are thereby transferred directly to the resulting ceramic shapes

Several different methods of mold fabrication were investigated. In partnership with a vendor, one mold has been made without porosity. In addition to the elimination of porosity, the material used in this method of mold fabrication is translucent, giving the added benefit of being able to observe injection of the ceramic material during the shape-forming process.

In addition to making the individual shapes, these parts must be cemented together into a final assembly. The cement must possess a thermal expansion coefficient similar to that of the ceramic parts, contain little to no contamination, and adequately bond the shapes to one another. It has been previously determined by Siemens that Zircar's zirconia cement is not well

suited to this application. Other cements tested by Siemens have shown initial success, but further work is needed. Blasch has used a modified version of the raw wet reverse spinel mix to join the parts prior to debinding and firing. The resulting assemblies possess a distinguishable cemented region and some minor cracking, both of which are believed to be due to employing an excessive amount of cement.

Investigation of debinding and firing cycles was carried out in an effort to reduce distortion, bloating, and cracking observed during thermal processing of the reverse spinel ceramic shapes.

The current reverse spinel composition (BPC-RSB-W) utilizes different organic binders than past compositions (BPC-RSA-G) as well as raw materials containing a larger proportion of magnesia to alumina. Modulus of rupture, apparent porosity, fired density, and gas permeability have been measured and are presented in Table 2-2. With the exception of gas permeability, all reported values are averages of the values determined from 10 test bars. The value reported for gas permeability is an average of the values determined from 3 disk specimens.

Table 2-2. Basic Property Values for Reverse Spinel Ceramic Material BPC-RSB-W

Property	Value
Modulus of Rupture (T = 25°C)	3436 psi = 23.69 MPa
Apparent Porosity	30.8%
Fired Density	2.46 g/cm^3
Gas Permeability	30.3 centidarcies

2.2.2.2. Ceramic Housing Design

Due to excessive permeability the ceramic stack housing is deemed impractical at this time. Activity continues with regard to advanced module manifolds.

2.2.3 RECIRCULATOR

Every SOFC generator that has been produced by Siemens to date has employed an ejector pump, or a parallel-connected array of such units, for purposes of recirculating partially utilized fuel, combustion products and freshly reformed fuel gas within the generator. Incoming fuel is the motive gas. A compressor is required to elevate the fuel pressure to the required level at entry to the ejector nozzle. An ejector pump is essentially a fixed operation point device.

Advantages of an alternative recirculation technology that employs a centrifugal blower are as follows:

- Generator performance is improved through more uniform fuel distribution. A centrifugal blower can be designed to give a much higher head rise than can an ejector pump.

- Turndown capability is acquired. Unlike an ejector pump, a centrifugal blower can produce a wide range of volumetric flow rate through speed reduction.

- Gas side startup heating is possible. A high volumetric flow rate of the start-up gas facilities the transfer of heat from a heating means to the generator.

- Alternative fuels might be used. Variation of recirculation ratio connotes variation of O to C ratio, and thus facilitates the use of alternative fuels.

Several manufacturers of high temperature blowers were invited to submit proposals for a design, prototype manufacture and testing program, on the basis of our specifications. All parties were given access to our benchmark design but were strongly encouraged to develop their own concepts. Initially two manufacturers showed a keen interest but ultimately only one of these produced a design concept and expressed a desire to go forward. This company is CAP (Creative Applications) of Yokohama, Japan. CAP has produced high temperature blowers in a variety of sizes, and have supplied units to Fuel Cell Technologies of Kingston Ontario for use in their 5 kW Beta units.

To date, the Capco recirculator continues to accumulate hours of operation in several of the FCT Beta units. Several modifications were required to the Capco unit to control bearing temperatures, which have shown to be successful. The high temperatures can be attributed mainly to the location and orientation of the recirculator. The recirculator for the BETA unit is placed at the inlet of the reformer, which has a significantly higher temperature than the reformer outlet, causing a higher transfer of heat to the bearings. Also, the shaft orientation is horizontal which imposes an increased load, due to gravity, on the bearings. Another issue is the simple straight blade design of the Capco impellor. In order to obtain the necessary head rise, the rotational speed is relatively high which will increase the bearing temperature.

Based on the information gained from Beta testing, the recirculator would need to be placed at the reformer outlet for the SECA Alpha unit. An additional design improvement would be to orient the shaft vertically. Lastly, it is desired to redesign the impellor to increase the head rise while decreasing the rotational speed.

Since the primary objective of the POC is to evaluate the HPD cell stack in a timely manner, it was decided not to incorporate a recirculator into the POC unit.

2.2.4 AIR MANIFOLD

Due to the layout of the generator it was believed that the cells adjacent to the reformer will provide more heat for reformation than the cells further away. Thus the air manifold for the POC was designed to provide control of individual rows of cells from the inner to outer. However, during the first test it was discovered that the heat was not radiating to the reformer as expected. A large temperature gradient was not measured between the inner and outer cells, most likely due to the several layers of radiation barriers of the strap assemblies.

Airflow control for POC test 3 has been designed to control a half bundle (3 cells), thus allowing control of the air from the front to the back and a less precise control from inner to outer. The following drawing in Figure 2-5 shows the flow control scheme:

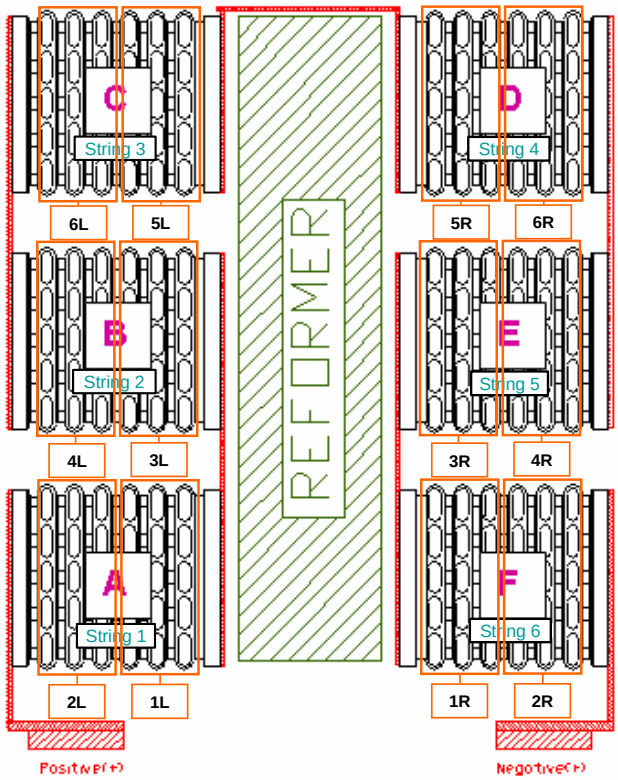

Figure 2-5. Air manifold configuration – revised control

This airflow configuration appears to have worked as temperature gradients within the stack were held at a minimum allowing for an increase in power.

2.2.5 PURGE GAS SYSTEM

The purge gas system consists of a pump that supplies a water/methanol solution to the fuel side of the cell stack during system start-up and shut-down. This new method of supplying a reducing atmosphere to the anode side of the cell stack replaces the expensive and impractical use of NH Mix gas cylinders. Tests have been carried out on several Beta cell stacks using the steam/methanol purge system. These tests used the steam purge system during both system start-up and shut-down, with no effect on the cell stack. Voltages well above the Nickel oxidation potential were maintained during all phases of the start-up and shut-down.

2.2.6 GAS-FIRED INTERNAL STARTUP COMBUSTOR

The gas fired burner currently in use in the BETA unit has shown to be more than adequate for its intended purpose and has performed well. As mentioned above, the flat plate startup heaters were eliminated for the POC unit and a method was needed to heat the exhaust gas prior to entering the recuperator. Due to these significant changes from the FCT Alpha unit, it was decided to minimize any further complexities and utilize an electric heater for this purpose.

If this methodology proves to be effective, it is anticipated that a gas-fired startup combustor similar to that used in the BETA unit could be adapted with minimal changes.

2.2.7 INTERNAL RECUPERATOR (RECUPERATIVE AIR PREHEATER)

Preheating of the process air for the POC is accomplished using the air feed tubes with internal enhancers which are contained within alumina boards. This counterflow arrangement has proven to be very successful in all of the FCT Alpha units and also in the SECA POC. No further design improvements are planned in this area.

2.2.8 COMBUSTION BOARD DESIGN

The function of the combustion board is to seal around the HPD cells that will provide a sufficient barrier to separate the combustion chamber from the recirculation gases. The standard method used for the cylindrical cells is to utilize a fibrous alumina board that has been accurately machined to fit the exact pitch of the cell bundles. Since each cell pitch and size varies between bundles, a precise mapping is required to ensure a satisfactory fit.

To accomplish this seal around the HPD cells for the POC, a flexible alumina paper was used which was to conform to the cell irregularity and unequal pitch. The design utilizes 6mm thick alumina paper that is cut to length and inserted between and around the cells. This configuration is demonstrated in Figure 2-6.

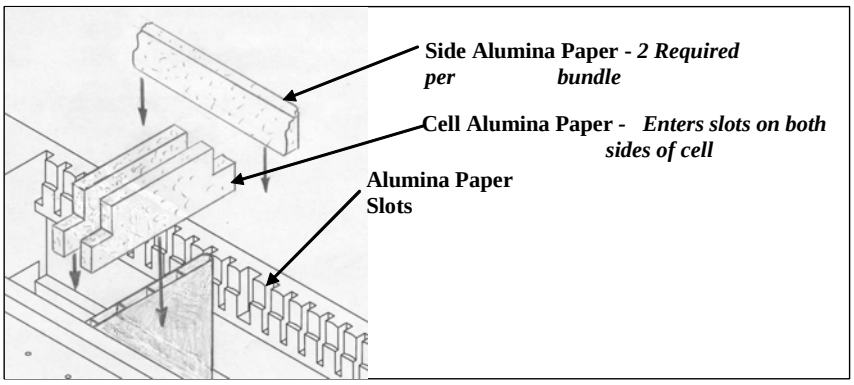

Figure 2-6. Combustion board design

After operating the first POC test it was evident that the there was insufficient sealing around the cells. A change was made for the second test which showed much improvement and was again used for the third test.

2.2.9 POWER LEAD

The power lead assembly utilizes a flat bar/strap design which has been proven to effectively direct the current from the cell stack to the terminal without disrupting the natural current density profile of the cell. The strap design uncouples the relative displacement of the cell bus to that of the cell stack, allowing minimal stresses on the cell.

2.2.10 REFORMER

The reformer used in the POC is based on the FCT Alpha unit. It utilizes an ejector to accomplish spent fuel recirculation and a catalyst bed of Haldor Topsoe wagon wheels for reforming. Details of the design and issues encountered during the test for the POC were discussed previously in section 2.1. 1.

2.3. SEAL DEVELOPMENT

2.3.1. INTRODUCTION

Glass compositions working at 800^{o}C have been reported previously. Herein efforts are directed toward developing compositions sutible for 900^{o}C applications. Despite temperature differences, the basic seals requirements remain the same, including thermal expansion match, low leak rate, good mechanical compliance at operating temperatures, etc. Using the same set of criteria to screen candidate materials, glass composition #82 for 900C applications was identified, and its thermal and sealing behaviors are evaluated under simulated fuel cell enironment.

2.3.2. EXPERIMENTAL

2.3.2.1. Thermal Mechanical Properties Of Sealing Material #82H

2.3.2.1.1. Composition and Thermal Expansion

Glass #82 is mainly composed of La_2O_3, B_2O_3, Al_2O_3, SiO_2, SrO, YSZ, and MgO. No alkaline metal oxides were added in this composition as many of them are known for fast diffusion and evaporation in reducing atmosphere at high temperatures. Metal oxides such as silicon and boron oxides serve as network-forming agents and others are added to adjust thermal-mechanical behaviors. Thermal expansion of the sealant from room temperature to 900^{o}C was measured as shown in Figure 2-73. #82 starts to expand almost linearly from room temperature to about 850^{o}C, and a small step was observed around 600C probably due to phase transformation though exact reason is not clear. After 850C the glass starts to soften where the thermal expansion curve drops sharply, which makes this glass suitable for operation as a compliant seal at 900^{o}C. Also seen in Figure 2-7, the sealant has a thermal expansion coefficient (TEC) of 10.95×10^{-6} up to 650^{o}C, which is very close to that of WPC3 air electrode and YSZ electrolyte. Matching TEC with other fuel cell components is critical for glass development since it can minimize stress generation during thermal cycling.

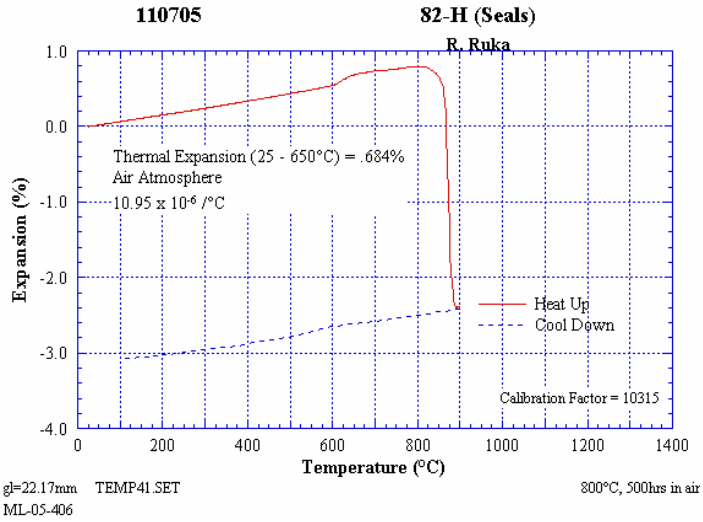

Figure 2-7. Thermal behavior of #82H glass/ceramic sealant

2.3.2.1.2. Stability

It is well known that glass, by definition, is not in a thermodynamically stable state, and it will crystallize over time at high temperatures. The crystallization process could alter its thermal behaviors including thermal expansion coefficient and softening point over time, which directly influences the functionality of the glass as high temperature seal. To evaluate the stability of glass #82, thermal expansion curves of a bar sample were measured before and after 500 hr thermal treatment at 800°C. As shown in Table 2-3, the TECs vary between 9.09 to 12.22 $\times 10^{-6}$ while most values are around 10.5×10^{-6}. At the same time the softening point increased to about 950°C after 500 hours of heat treatment, which indicates the crystallization process continued as expected.

Table 2-3. Thermal Expansion Coefficient of #82 Glass Sealant

	Beginning of Life	1st after 500-hr hold	2nd	3rd	4th	5th	6th	7th
TEC ($\times 10^{-6}$)	10.95	9.09	12.22	11.02	10.35	10.52	10.84	10.08
Softening point (C)	850	>850	940	950	970	950	950	960

2.3.2.2. HPD Cell TEST USING #82H SEALANT

2.3.2.2.1. Test Article Preparation

In order to further evaluate #82 in a real fuel cell operating condition, a "once-through" HPD cell was sealed to a dense ZrO_2 end cap using the same glass. For detailed sealing procedures, refer to the internal memo IN-05-041. A picture of the sealed structure was taken in Figure 2-8 showing part of the cell, dense ZrO_2 cap, and #82 glass powder encapsulated by hardened epoxy. To monitor temperature change for potential gas leakage from the seal region during testing, three thermal couples, T1 (OE), T2 (CE) and T3 (CE) were placed on the cell with T2 and T3 close to the seal. In addition three voltage tabs were attached to the cell at different elevations of the cell with U1 at open end, U2 at middle section, and U3 at closed end. A reference electrode probe was also used to monitor the change of gas compositions in exhaust fuel.

Figure 2-8. A "once-through" HPD cell sealed with a dense ZrO_2 cap using #82 glass seal

2.3.2.3. *CELL TEST AND ANALYSIS*

The testing plan for this seal test is to first start up the cell, hold it at open circuit for 500 hours, and finally run 5 thermal cycles.

2.3.2.3.1. CURING THE GLASS

The glass curing procedure includes heating the seals region to 1050^{o}C for half an hour or so to cure the glass and then cooling it down to 900^{o}C. Figure 2-9 shows the curing process for the HPD cell with cover gas containing 20% water vapor as fuel. The relationship between temperature and voltage during the first 40 hour period shows almost the same curing pattern as a previous test on #57 glass (IN-05-041). Cell temperature started to rise slowly to about 250^{o}C, during which the hardened epoxy provided sufficient sealing as indicated by the rise in OCV. As the epoxy was burned off above 250^{o}C the OCV decreased. At 600C the glass powder started to sinter and air leakage decreased. As a result, cell voltage rose again to 950mV at 800^{o}C. As temperature continued to rise, it seems that high temperature leak dominated and cell voltage dropped to 660mV. At 1050^{o}C, the sealant #82 was cured and a complete seal was achieved. The seal was then cooled along with the cell kept at 900^{o}C, and cell voltage was stabilized at around 770mV.

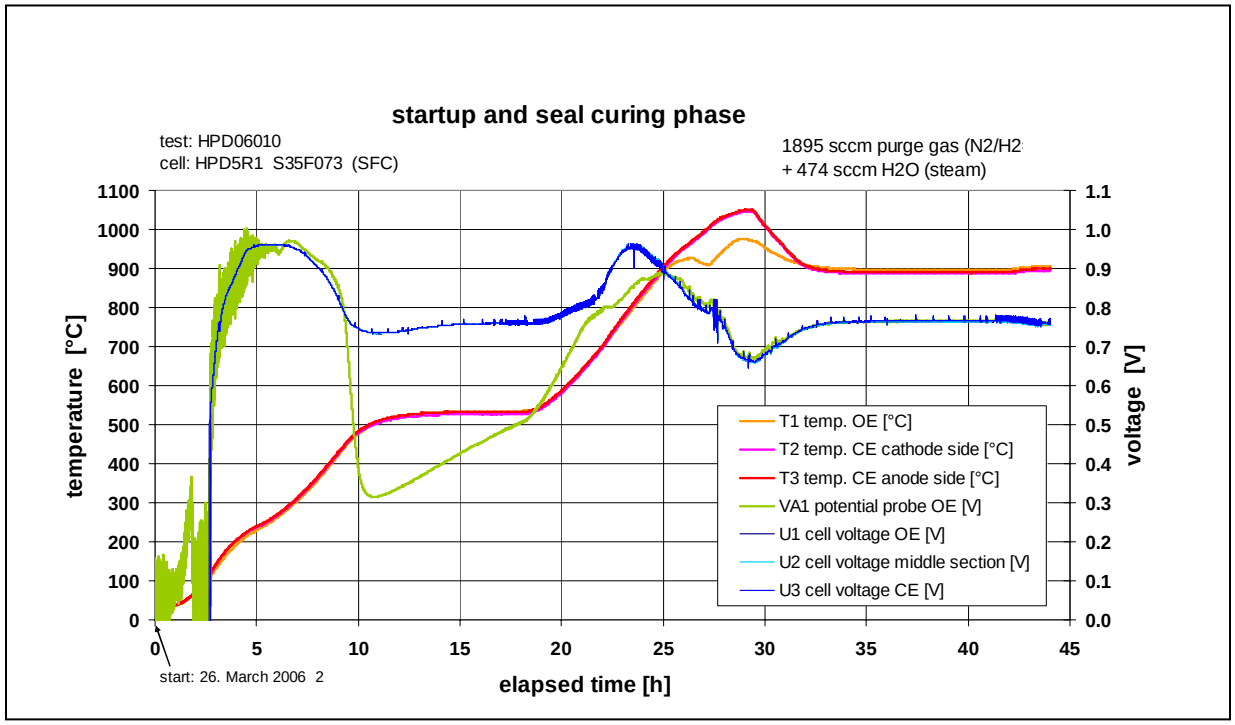

Figure 2-9. Seals temperature, voltage, and current density profiles during the glass curing process

2.3.2.3.2. CONSTANT HOLD FOR 500 HOURS

As shown in Figure 2-10, #82 provided a good seal at 900°C with no performance degradation until the first 185th hour when a power supply interruption occurred. The incident did not cause temperature change but did trigger the test stand to enter the protection mode of flowing purge gas. After the 5% H_2 was reintroduced the cell voltage lost 30-40mV and then gradually increased over time. However, the cell did not fully recover the total voltage loss caused by the incident. Information obtained so far cannot explain why voltage dropped due to the gas change. After the power interruption incident cell voltage was relatively stable until thermal cycles, which indicates that the glass still provided sufficient seal.

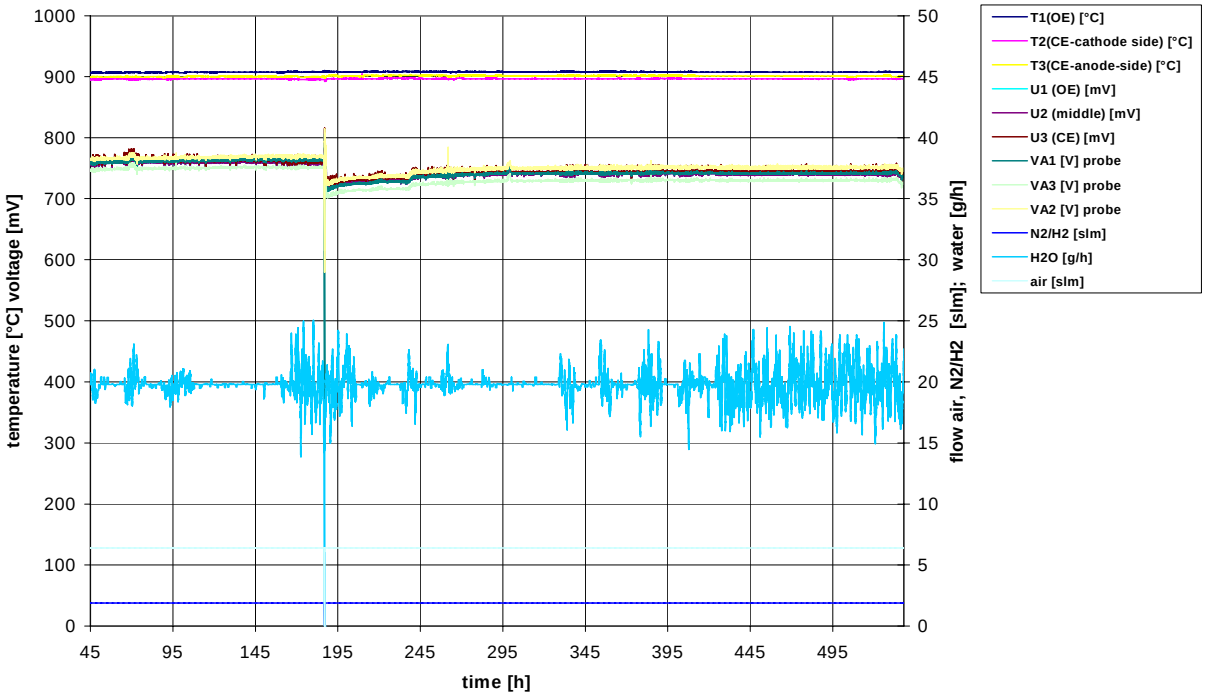

Figure 2-10. Constant hold at 900C for 500 hours

2.3.2.3.3. THERMAL CYCLES

At the end of the 500-hour test, the cell was thermally cycled between 900°C and 100°C approximately every two days, as shown in Figure 2-11. Under 5%H_2 the cell was cooled down for 25 hours to 100°C and slowly heated back up to 900°C for 20 hours and held there for about 10 hours. During the entire thermal cycling, cell voltage was relatively stable and actually the peak voltage at 700°C increased gradually over each cycle, indicating that the sealant was in a stable condition. During the same period of time the cell survived three incidents including a water interruption at 578th hour, a power supply interruption 625th hour, and a maintenance at the last thermal cycle, and none of these incidents caused any noticeable permanent change in OCV.

After five thermal cycles, the seal went through additional 350 hours of holding at 900°C as shown in Figure 2-12. At the 1180th hour the seal again went through an air supply breakdown incident, however, no damage in terms of cell voltage was observed. The cell voltage was stabilized at 750-760mV.

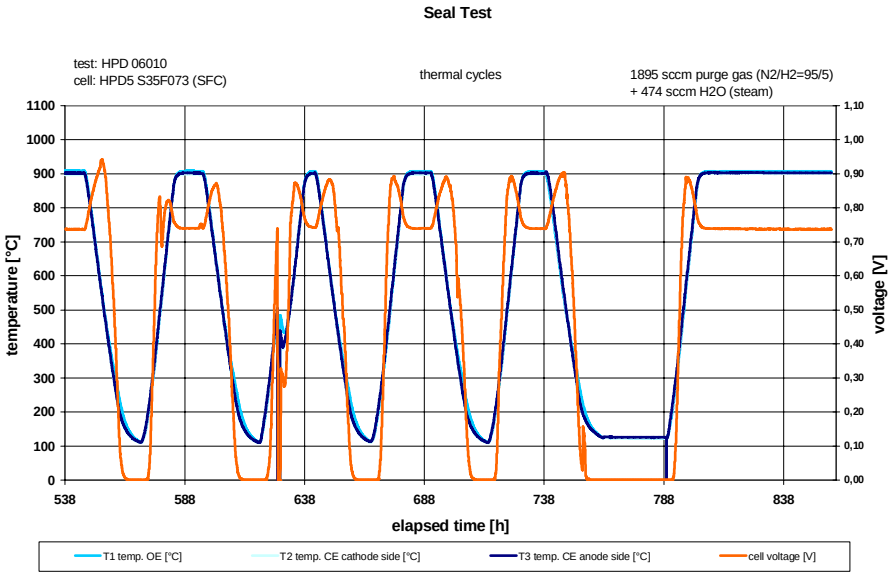

Figure 2-11. Seal temperature and voltage profiles during thermal cycles

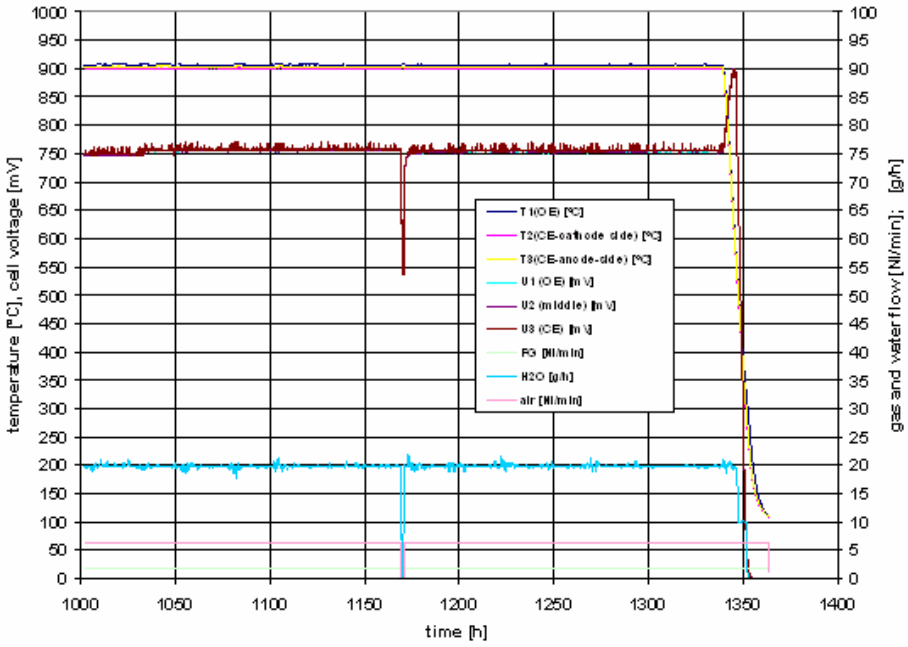

Figure 2-12. Seal temperature and voltage profiles after five thermal cycles.

2.3.2.4. *POST ANALYSIS*

The cell was dissembled after the test. Shown in Figure 2-13 (a) and (b), unexpectedly multiple cracks were observed on both IC and FE sides of the cell. It seems that these cracks originated from seals region and propagated upward into active areas of the cell. Little Ni oxidation was observed along with these cracks though some minor burning marks were visible. These observations were consistent with constant cell temperatures measured in seal region, indicating there is no gross leak through these cracks. Also shown in Figure 2-13(c), glass sealant materials went through significant changes in morphology. Bubbles were observed in seal regions, and some sealant materials appeared missing during the test, which suggests that either some oxides were evaporated or unexpected reactions occurred with fuel stream or both. Since there were almost no cell voltage data to suggest cell failure like this, it is hard to obtain a definite answer of how and when the cell failed. Cross sectional microstructures in Figure 2-14 show that the AE is well protected from the plasma-sprayed ZrO_2 electrolyte as no reactions were observed between glass and air electrode. Composition analysis of the seal region in Figure 2-14(e) showed that Si content is disproportionably lower than the original composition confirming the speculation that Si evaporated in the reducing atmosphere. In addition, some of the oxides such as LaO_x and BaO could absorb or react with water at high temperatures as a large amount of bubbles were observed. Excessive bubbles would form a continuous path for gas leakage.

2.3.3. SUMMARY

Efforts on glass sealants development have shifted to 900^{o}C applications. In this report, thermal behaviors and a HPD cell test of #82 glass sealant material, developed in Pittsburgh, were reported. Results show that #82 on average matches thermal expansion of other major cell components after 500-hour heat treatment. A real cell test was also carried out by sealing a HPD5 cell to a dense ZrO_2 cap using #82 glass seal tested at 900^{o}C. Long-term stability test was held at 90^{o}0C for 500 hours followed by five thermal cycles. OCV and temperature measurements indicated that the seal was in a stable condition with no indication of failures during the entire test. However, post analysis after the cell was disassembled showed surprisingly different results. Multiple cracks propagated from the seal region and air bubbles developed in seals. The cell failure suggests that #82 sealant material needs to be further improved especially in terms of thermal-mechanical and chemical stability at high temperatures, reducing atmospheres, and high humidity.

		
(a)	(b)	(c)

Figure 2-13. Post analysis showing cell (a) cracks on FE side (b) cracks on IC sides, and (c) bubbles in seals

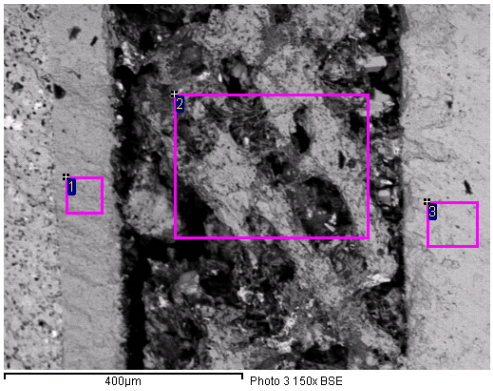

(a)

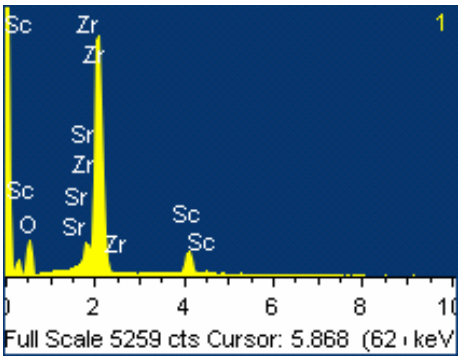

(b)

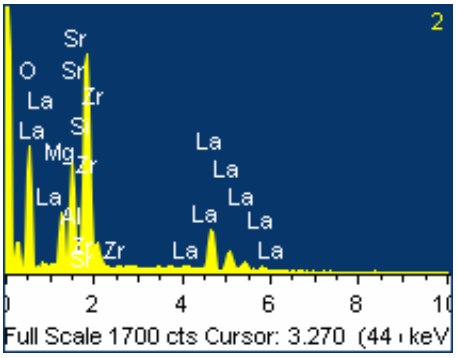

(c)

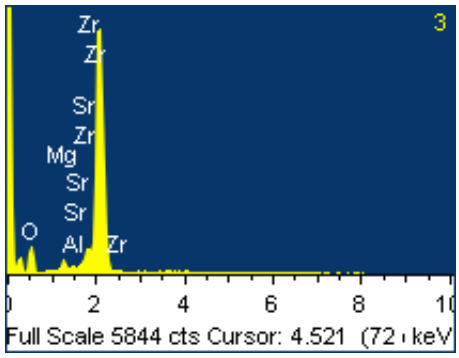

(d)

Processing option : All elements analyzed (Normalized) All results in atomic%

Spectrum	In stats.	O	Mg	Al	Si	Sc	Sr	Zr	La
1	Yes	70.04				4.41	1.22	24.33	
2	Yes	69.04	5.41	8.13	1.37		10.98	1.54	3.53
3	Yes	65.36	2.06	0.36			1.00	31.22	

Figure 2-14. Cross sectional element mapping of the seals region (post analysis). (a) a picture of the seals region including section 1 being the plasma-sprayed ZrO2 coating, section 2 the glass seal, and section 3 dense ZrO2 cap; (b)-(d) EDX spectra of the ZrO2 coating, seal, and ZrO2 cap, respectively; and (e) a table showing the seal composition

3 BOP DEVELOPMENT

3.1 CONTROL SIMPLIFICATION

Significant effort has been put forward in the area of data management and reporting as well as secure access to this data over the Internet. A Modbus/TCP driver has been developed under QNX 4 and was ported to QNX Neutrino.

The Athena CPU platform has been configured to run the Neutrino operating system.

The Athena CPU platform will provide a significant opportunity for cost reduction as an interim step towards further hardware simplification. Hardware multiplexing on the next revision of Signal Conditioning Board will also provide cost savings even after the cost for software development has been accounted for.

The new Beta signal conditioning boards have been proven to be very reliable, with no significant design changes required.

The Gamma boards will hold the first custom-built microcontroller board that resides on the PC/104 bus. This allows either the custom board or an off-the-shelf PC/104 CPU card to be used. The analog circuits will not contain any analog isolation which is expensive to implement. Analog isolation was used initially in order to avoid any problems with the string voltages in the stack. Further testing will indicate if 'ground loops' are a potential problem.

It is expected that the Gamma boards will implement a simpler component list for the SOFC. Fewer transducers and sensors are expected to be used by this point which will allow the board to become smaller and the component count to go down.

The final Production-Ready SCB will contain the entire required control and data acquisition engine including the microcontroller. This will allow for an optimized board in terms of physical size and component count. It will also minimize the required connectors which will help with the reliability and Mean Time Between Failures (MTBF). Economies of scale will be used so that the labor cost of these boards is minimal. It is expected that a completely automated test bench, which has been started with the Beta Boards, will continue to this phase of the project. The test bench allows an entire board to be tested for functionality and spec in a period of minutes instead of hours.

3.2 BOP DESIGN SIMPLIFICATION

The following sections outline present and future work required to simplify the design of individual subsystems, in order to reduce the number and complexity of components required.

3.2.1 ELECTRICAL SYSTEM

Where possible, suppliers have been encouraged to tailor their designs to allow devices to be powered directly off the battery voltage, in order to reduce the size and number of DC/DC converters required, and to improve reliability. Efforts have been made to source pressure transducers and other devices that are PCB board mountable. This will reduce the amount of field wiring required, and reduce system cost. Other work required to reduce the cost of the electrical system is outlined in section 3.8.1 above.

3.2.2 FUEL SUPPLY SYSTEM

Alternate suppliers of the fuel mass flow controllers have been found, and FCT will prepare a specification for the fuel mass flow controllers specific to the SOFC requirements. It may also be possible to integrate the fuel shut-off valves with the mass flow controllers to reduce component costs. Alternate piping arrangements and materials are been investigated, including an improved desulfurizer vessel design.

3.2.3 AIR SUPPLY SYSTEM

Alternate piping materials and mechanical arrangements were pursed in order to reduce the parts count and facilitate faster production times. Plastics manufacturers will be contacted to obtain design expertise, with the option of having all of the piping assembled by a third party supplier.

Alternate suppliers of all air supply system components will be found, and less expensive components will be substituted where possible. For example, the venturi flow elements are cast brass, and would be much cheaper if they were produced from molded plastic or similar materials.

3.2.4 WASTE HEAT EXTRACTION

The waste heat exchanger is manufactured by a heat exchanger company specifically tailored to the fuel cell industry. Alternate suppliers for this part will be found, and it may be possible to switch to less expensive materials given the lower exhaust temperatures that resulted from the improved recuperator heat exchanger performance. The thermocouples, thermistors and water flow transducer will be removed from future units, as these are included in the BOP at this point to provide engineering information only.

3.3 BOP COMPONENT DEVELOPMENT

The cost of the DC power module (used to supply the various bus voltages required by the BOP) can be reduced by eliminating as many power rails as possible, and by eliminating many of the current transducers used to gather engineering information. DC

to DC converter manufacturers will be contacted with the goal of obtaining an off-the–shelf module capable of providing all of the various voltage rails.

3.3.1 INVERTERS

1ST GENERATION INVERTERS

The first generation inverters, partially developed on the SECA program have been received and testing was carried out on various features, including the following:

- anti-islanding,
- seamless transfer from grid-tie to stand-alone and return,
- overall efficiency (DC to AC),
- total harmonic distortion.

To date all features are working well with the exception of overall efficiency, which is less than the 85% target. It must be noted that the 10 volt input is very low and will incur significant additional losses relative to a higher input voltage available from the HPD cells.

2ND GENERATION INVERTERS

Investigations have been carried out over a large range of inverter manufacturers and university development programs. Some novel approaches to inverter design, particularly low loss DC to DC stages have been identified. Efficiencies of 90% are possible even with a 10 volt input. A down-selection process will be carried out in the next period and a vendor selected for development of a second generation unit.

3.3.2 DESULFURIZER

FCT has tested a reagent provided by ECN in the Netherlands. In the previous report, this reagent was not identified due to the confidentiality agreements signed between FCT and ECN. Since that time, ECN has started a new subsidiary named SulphCatch B.V. which will commercially sell the reagent now identified as NGDM-1. NGDM-1 is a non-nickel based, ambient temperature operating reagent that was specifically developed to adsorb Tetrahydrothiophene (THT) compounds from natural gases. FCT tests with NGDM-1 and THT have been very encouraging. NGDM-1 has more than 4 times the sulfur capacitance of the next best THT desulfurization reagent tested by FCT. NGDM-1 was also tested with Tertiary Butyl Mercaptan (TBM), Ethyl Mercaptan (EM) and Carbonyl Sulfide (COS). The results indicated that NGDM-1 is a poor reagent for adsorbing TBM and COS odorants, however it has some capacitance for adsorbing EM at ambient temperature.

Süd Chemie's C8 activated carbon was tested with THT, TBM and COS. The capacitance of C8 for TBM was the highest of all the reagents tested to date. For THT, it only has about 60% of the capacitance of SulphCatch NGDM-1. For COS, C8 has similar adsorption performance to other reagents.

Tokyo Gas's TOSPIX94 was tested with COS and TBM. The results of the TBM test indicated that TOSPIX 94 capacitance was somewhat reduced when city natural gas was used rather than when pure methane was used. This indicated that TOSPIX 94 might have the ability to adsorb odorants other than TBM and Dimethyl Sulfide (DMS) for which it was developed. A follow-on test was conducted using COS as the odorant. The TOSPIX94 was observed to adsorb the COS. Final results indicated that it had somewhat better COS capacitance than all the other reagents tested to date.

COS remains a difficult sulfur compound for adsorption. In general, the reagent capacitances are low. Four other reagents were tested besides the ones described in the previous paragraphs. C28 and RVS-1 from Süd Chemie and a combination bed of CNG1 and CNG2 manufactured by Engelhard. Engelhard suggested the use of their CNG1 and CNG2 adsorption reagents before testing their Selectra SULF-X system. At ambient temperatures, the Süd Chemie C28 and Engelhard CNG1/CNG2 reagents have essentially the same capacitances for COS. The RVS-1 material was tested at 300 ºC with COS. This particular reagent/odorant combination resulted in very poor performance.

EM is commonly used to odorize propane. Besides the SulphCatch NGDM-1 reagent, testing was also conducted with Süd Chemie C28 reagent at elevated temperature. At 200 ºC, C28 adsorbed EM to almost 1/3 of its initial mass. This is encouraging as a heated desulfurizer scheme may be an ultimate means to remove the high concentrations of odorants found in propane.

The reagent evaluation work performed in the last few months has highlighted some effective, non-nickel reagents that can be used in lieu of the C28 material for various odorants. FCT continues to test new reagents that are still being developed by various reagent suppliers. New non-nickel based reagents formulations by BASF and Süd Chemie are scheduled to be tested in the next few months.

3.3.3 MULTI FUEL DEVELOPMENT

Work has been carried out on propane as described in the previous section, as well as optimization of the fuel system for multi-fuel capacity: Adopting the system for methanol fuel has been initiated., directed towards modifying and optimizing the fuel supply system for accommodating liquid methanol fuel. Compared with other liquid fuel, reforming of methanol is very easy and can be done in a unit designed for natural gas use. Methanol is also nearly completely free from sulphur. However, the use of methanol requires modification to the fuel delivery system, and will also affect the overall energy balance of the system.

The major issues related to methanol feed are:

- Liquid nature of the fuel, and the necessity to evaporate it before supplying to the reformer/stack system
- Large amount of heat required for evaporation of methanol, particularly if it is used in diluted form.
- A strong tendency of methanol for cracking with the formation of carbon. Based on the literature data, cracking of pure methanol may happen already at temperatures in order of 300ºC or less, and may be strongly catalyzed by some of the standard engineering materials. Methanol cracking can be prevented by the presence of water (steam), the molar ratio H2O/CH3OH of 1 or above are required according to thermodynamics.

The following tasks have been carried out directed towards methanol feed modification:

- Analysis of options and initial system modeling have been performed, including the following options:
  - Liquid methanol feed through an injector. This method would require a considerable effort to develop of fuel injector that could work at the particular conditions (injection at a wide range of flow rates into the very hot anode recycled gas).
  - Use of 63% methanol solution as the fuel (molar ratio H2O/CH3OH = 1), fed to the stack in gaseous form. Because of the presence of water, no strict control on evaporation conditions is necessary, however evaporation of water would result in lowering of the overall thermal efficiently of the system.
  - Use of pure (100%) methanol, evaporated at conditions where carbon formation does not occur, and fed it to the stack in gaseous form. This option also requires that the methanol vapors are introduced to the stack and mixed with the anode gas without the formation of carbon.

The third (last) option was rated to be the most attractive and was selected for further development.

- Conditions for evaporating pure methanol have been tested experimentally, and the potential construction materials for the evaporator and the acceptable temperature range identified,
- Mixing of methanol vapors with stack gas has been tested experimentally using simulated stack gas. A design of the mixing port has been developed which allows safe introduction of (pure) methanol vapors into the stack gas. The design required only a small modification to the fuel injection port of a typical natural gas fed system. The mixing system was tested to operate without carbon formation in the flow range required for feeding a 5 kW unit (down to 2 mL/min).

- Work continues on modeling the effect of this particular method of methanol feed on the performance and operation of the SOFC unit.

.

4 LIST OF ACRONYMS

AE	Air Electrode
APS	Atmospheric Plasma Spray
BOP	Balance of Plant
CE	Closed End
EL	Electrolyte
FCT	Fuel Cell Technologies, Ltd.
FE	Fuel Electrode
GDC	Gallium Doped Ceria
HPD	High Power Density
IC	Interconnection
PNG	Pipeline Natural Gas
POC	Proof-of-Concept
ScSZ	Scandia Doped Zirconia
SECA	Solid State Energy Conversion Alliance
SOFC	Solid Oxide Fuel Cell
SFC	Stationary Fuel Cells
V-J	Voltage-Current Density
WPC3	Westinghouse Proprietary Composition 3
YSZ	Yttria Stabilized Zirconia